Microstructure of nuclear structural materials, Zr and V-5Cr-5Ti, determined by X-ray line profile analysis

Zhijian Fan

Physics Doctorate School

School Leader: Prof. Jenő Gubicza

Material Science and Solid State Physics Program

Program Leader: Prof. István Groma

Eötvös Loránd University

Institute of Physics

Department of Materials Physics

Advisers:

Prof. Tamás Ungár, DSc

Dr. Gábor Ribárik

Ph.D. Thesis

2019.

Contents

Chapter 1

Introduction

Since nuclear fission of uranium was discovered in 1938 (Hahn & Strassmann, 1939; Meitner & Frisch, 1939), people have developed different kinds of reactors for harnessing nuclear energy. Currently fossil-fuel power is still one of the dominant sources of energy in the world. However, in contrast to fossil fuel, fission power hardly produces greenhouse gases. The emission intensity per unit generated energy of fission electricity in total life-cycle is about 12 g CO_2 eq/kWh, which is far below than the values of 820 and 490 g CO_2 eq/kWh for coal and fossil gas, respectively. This emission intensity is even lower than that of renewable energy when the latter is considered as a whole (Warner & Heath, 2012). In order to satisfy the limitations of greenhouse gas emission, nuclear energy has been getting increased attention and regarded as a complementary alternative to fossil-fuel power. According to the power reactor information system of International Atomic Energy Agency (IAEA), as of 2018 around the world 454 civil fission reactors are in operation for generating electricity, 54 new nuclear power reactors are under construction. Nuclear power stations contributed a net electric capacity of ~400 GW. Nowadays fission electricity becomes the second largest source of low-carbon electricity, somewhat less than hydroelectricity. In addition, fission power is a stable and sustainable energy source, while hydroelectricity and other renewable energy are usually intermittent and seasonal.

Besides nuclear fission reaction, fusion of light nuclei can prospectively be used to produce a huge amount of energy (Shultis & Faw, 2002). As a potential candidate of energy source, fusion power plant has several advantages in concept over any of current

widely applied fission stations. The fuels of nuclear fusion are hydrogen isotopes such as deuterium and tritium (Kikuchi et al., 2012). The reserve of deuterium in sea water is abundant, ~30 g/m^3, whereas tritium is minor in nature. But tritium can be obtained via the reaction of neutron and ^{6}Li, where lithium in the Earth's crust, ~30 ppm, can be at least available for several hundred years. The radioactive waste created in operation of fusion reactor would generally be far less than fission reactor. And the half-life period of fusion waste is very short so that the radioactivity decays more rapidly. That is very helpful to storage waste safely. Began in the 1950s the development of fusion reactors for civil purposes was initiated on both aspects of theory and experiment. In the early time, fusion electricity was expected to be realized readily as the rapid process of fission power. But until now any existing design can't produce a positive energy balance, i.e. the input energy is always higher than the released fusion energy. It is extremely difficult in engineering for the confinement of plasma at high temperature and keeping continuous fusion reaction. Currently, one of the largest fusion projects is International Thermonuclear Experimental Reactor (ITER), which is started in 2007 and located in France. The project is collaborated between seven-member entities: the European Union, India, Japan, China, Russia, South Korea, and the United States.

The research and development of advanced nuclear fission and fusion power will attract persistent efforts of people. A critical issue is how to keep safe and reliable running of nuclear reactor. The in-service conditions of nuclear reactor are far more complex than those of fossil-fuel power plant. Especially, huge amounts of neutrons and heat accumulate in the reactor during the operation. Some common specifications are requested as follows for nuclear materials (Hoffelner, 2013; Whittle, 2016). (i) Nuclear materials should have few of swelling, phase transformation, and segregation or precipitation under long-term irradiation. (ii) Nuclear materials should have excellent resistances of corrosion and high-temperature oxidation. (iii) Nuclear materials should have comprehensive performance of strength, plasticity and fracture toughness for maintaining stability and completeness of component parts. (iv) Structural materials in reactor should have low absorption and activation cross-sections of neutron, and short half-life period. In practice, the selection of nuclear materials would be a tradeoff based on performance and cost of material. In the present dissertation we focused on two typical nuclear structural materials, Zr and V-5Cr-5Ti. Zr-based alloys are extensively employed as fuel cladding materials in fission reactor, due to their excellent

combination of properties of low absorption of thermal neutrons, corrosion resistance, thermal conductivity and mechanical behavior under complex service circumstances (Lemaignan & Motta, 1994; Onimus & Béchade, 2012). While vanadium alloys are prospective blanket structural materials in fusion reactor, considerable efforts have been made to improve high temperature strength, ductility at low temperatures, thermal or irradiation induced creep resistance and degradation under irradiation environment (Muroga, 2012; Muroga et al., 2014).

Polycrystalline Zr is composed of single crystal grains with a hexagonal-close-packed (*hcp*) structure at room temperature, each grain exhibiting anisotropic thermal, elastic and plastic properties. In manufacturing processes, the preferred crystallographic orientation of individual grains is developed, and various types of texture are formed depending on the fabrication conditions (Tenckhoff, 1988). The macro-mechanical response of the polycrystalline aggregates of Zr and its alloys is influenced significantly by texture, with manifesting strong elastoplastic anisotropy when different loading directions are applied on a sample (Beyerlein & Tome, 2008; Xu et al., 2008; Long et al., 2016). With regard to the glide plane in *hcp* crystals there are three major slip-system types: basal, prismatic and pyramidal. In terms of the glide directions and the dislocation character there are eleven sub-slip-systems (Dragomir & Ungár, 2002). In addition, {10.2} and {11.1} type tensile twinning and {11.2} and {10.1} type compressive twinning are also important deformation modes (Beyerlein & Tomé, 2008; Xu et al., 2008; Abdolvand et al., 2015; Li et al., 2016). In order to understand the deformation behavior in textured Zr and its alloys, it is necessary to investigate the contributions of different deformation modes during mechanical loading. Earlier studies of experimental characterization have shown that {10.0}<11.0> type prismatic <*a*> slip is the primary slip-system (Tenckhoff, 1988; McCabe et al., 2006; Balogh et al., 2012). Since, however, there are only two independent slip-systems for the prismatic <*a*> slip, other slip-systems, like {00.2}<11.0> type basal slip, {10.1}<11.0> type pyramidal <*a*> slip, {10.1}<11.3> pyramidal <*c*+*a*> slip and a few others may also be activated in order to fulfill the von Mises compatibility criterion. There have been a number of attempts recently to determine average dislocation densities and slip activities in pure Zr and its alloys affected either by irradiation or by plastic deformation, using the method of X-ray or neutron diffraction line profile analysis (Ungár et al., 2007, 2015; Balogh et al., 2012; Long et al., 2016; Seymour et al., 2017). It is, however, still

a challenge to identify the secondary slip-systems accurately in textured Zr and its alloys.

As for vanadium alloys, in order to improve mechanical properties of strength and ductility, various processing techniques such as cold rolling combined with aging (Fu et al., 2013), multi-directional forging (MDF) (Tyumentsev et al., 2011), mechanical alloying (MA) (Zheng et al., 2014b), equal channel angular pressing (ECAP) (Chun et al., 2009), and high-pressure torsion (HPT) (Ditenberg & Tyumentsev, 2018) have been developed in recent years. As one of severe plastic deformation techniques, high-pressure torsion has received much attention to enhance mechanical capabilities of materials (Zhilyaev & Langdon, 2008; Pippan, 2009). During the HPT procedure samples are imposed to a large torsional strain under high hydrostatic pressure in order to produce bulk nanostructured materials with exceptionally high strength. For the materials with fine grain size large numbers of grain boundaries could naturally act as sinks for point defects. Therefore, nanostructured materials were found to be of better resistance of the ductility reduction due to irradiation damages (Wurster & Pippan, 2009). Some reports (Zhilyaev et al., 2001, 2003; Zhilyaev & Langdon, 2008) have shown that the applied pressure is an important external factor for the formation of homogeneous microstructure in the entire specimen. With increasing the pressure, the microhardness value in the center of the specimen will be more close to that in the edge of the specimen after larger numbers of revolutions. In Reference (Jóni et al., 2013) two kinds of *bcc* metals, tantalum and niobium, were processed by HPT under different pressures and the microstructure was investigated by X-ray line profile analysis. It was shown that in the specimens deformed with higher pressure the dislocation density was smaller. This peculiar behavior was attributed to the larger vacancy concentration produced and retained in the specimen deformed under higher pressure. At the event of unloading a larger number of dislocations were annihilated because of the enhanced diffusion due to the larger instantaneous vacancy concentration. Many observations on the microstructure in vanadium alloys have been carried out using electron microscopy (Tyumentsev et al., 2011; Zheng et al., 2014b; Ditenberg & Tyumentsev, 2018). However, because of limited observation area it is not suitable for electron microscopy to obtain quantitatively microstructural information with high statistical accuracy. In contrast to electron beam, X-ray can penetrate deeply into the specimen. X-ray line profile analysis is a powerful and complementary method to characterize dislocation

densities, grain (or subgrain) size and planar defects in nanostructured crystalline materials.

In this research, in order to understand the correlation between the microstructure and strength of textured Zr and fine-grained V alloys, two kinds of experiments were designed and performed, respectively. As regards Zr, the cold-rolled specimens were tensile-deformed along the rolling (RD) and transverse (TD) directions, mechanical responses along these two directions were compared. For the accommodation of strain incompatibility between different texture components, the dislocation densities and the prevalent slip-system types in each texture component of material could be different during the deformation. On the other hand, the V-5Cr-5Ti specimens were processed by HPT at 4 and 8 GPa pressures, microhardness and thermal stability of the specimens were investigated. The shear deformation of the specimen changes proportional to the radial distance and the number of rotations, which results in microstructure evolving with position and rotation number of the sample. For the purpose of obtaining the microstructure in the different texture components or the positions of the samples, high-resolution micro-beam X-ray diffraction was applied and a systematic procedure for identifying the diffraction peaks corresponding to the different texture components was proposed. The microstructure of the specimens was determined by the extended convolutional multiple whole profile (CMWP) procedure (Ungár et al., 2001; Ribárik et al., 2004; Balogh et al., 2006, 2009). Finally, the microstructural information was correlated with the mechanical properties of the deformed specimens.

The sketch of the dissertation is arranged as follows. Chapter 2 provides a brief overview of theory and method of X-ray line profile analysis. Chapter 3 introduces the nuclear materials used for fission and fusion reactors, and reviews recent experimental works on zirconium and vanadium alloys. Chapter 4 and 5 present the research topics for tensile-deformed Zr and HPT processed V-5Cr-5Ti, respectively. In the end, the summary and conclusions of the work is given in Chapter 6. Appendix shows an attempt to measure neutron irradiated Zr-4 alloy by laboratory X-ray diffractometer. And all the microstructural results of HPT processed V-5Cr-5Ti are tabulated in the appendix.

Chapter 2

X-ray line profile analysis

In the early twenties of the last century, X-ray diffraction peak broadening was found to be closely connected with imperfections of crystalline materials (Scherrer, 1918; Becker, 1927). On the base of quantitative evaluation of diffraction peak broadening, microstructures in the samples can be deduced. Such a procedure is usually named as X-ray line profile analysis (XLPA).

In view of kinematical theory of diffraction, crystallite (or coherent domain) size and lattice distortions are two prominent factors influencing diffraction line profiles (Bertaut, 1949; Warren, 1959, 1969). Complex strain fields in materials can be produced due to lattice defects of different dimensions, such as point, linear and planar defects (Krivoglaz, 1996). For the purpose of obtaining microstructural information accurately, it is an essential prerequisite to describe and distinguish the effects of various types of microstructures on diffraction peaks.

During the past years, the fundamental theories for modelling crystallite size and strain related diffraction patterns have been well established (Guinier, 1963; Wilkens, 1970a; Langford & Wilson, 1978; Groma et al., 1988; Groma, 1998). Meanwhile, with the development of X-ray diffraction instrumentation and computer technology, nowadays the whole diffraction pattern can be evaluated directly using ab initio size and strain functions (Langford et al., 2000; Ungár et al., 2001; Scardi & Leoni, 2002; Ribárik et al., 2001, 2004). One of the widely used programs for diffraction data analysis is CMWP, which was developed in 2000s (Ribárik et al., 2001, 2004; Balogh et al., 2006,

2009). The program can provide microstructure parameters, including crystallite size and distribution, dislocation density and character, the arrangement parameter of dislocations, and the probability of stacking faults and twins. These parameters are vitally important for understanding the properties of materials.

As we know, transmission electron microscopy (TEM) can also be applied to investigate microstructures of materials. It is more favorable to obtain local microstructural images because of the inherent properties of TEM. In contrast, the morphology of microstructures can't be observed by X-ray diffraction. However, the procedure of XLPA is able to provide statistical information of microstructure in bulk materials conveniently. Both TEM and XLPA are complementary for the complete understanding of the details of microstructure.

In this chapter, the kinematical diffraction theory of imperfect crystalline materials, the models of crystallite size and dislocations on peak broadening, and the usage of CMWP are briefly summarized.

2.1 Kinematical diffraction theory

Crystalline material can be regarded as a periodic arrangement of a lot of unit cells, although the atoms oscillate around average positions at any time. Assuming a beam of X-ray with a wavelength of λ falls on the surface of crystalline material, the scattering amplitude of each unit cell is usually called the structure factor (Warren, 1969),

$$F = \sum_r f_r \exp(2\pi i \mathbf{h} \cdot \mathbf{u}_r) \ , \tag{2.1}$$

where f_r and $\mathbf{u}_r$ are the atomic scattering factor and the position of the *r*th atom in the unit cell, $\mathbf{h} = (\mathbf{s}_1 - \mathbf{s}_0)/\lambda$ is the scattering vector, $\mathbf{s}_0$ and $\mathbf{s}_1$ are the incident and reflected directions, and the summation involves all different atoms in the *n*th unit cell.

For X-ray diffraction experiments, instead of scattering amplitude the measurable quantity is diffraction intensity. It is the square of the modulus of scattering amplitude. The diffraction intensity of crystalline material can be expressed as a function of scattering vector,

$$I(\mathbf{h}) = \sum_{n,n'} |F|^2 \exp[2\pi i \mathbf{h} \cdot (\mathbf{u}_n - \mathbf{u}_{n'})] \ , \tag{2.2}$$

where $\mathbf{u}_n$ and $\mathbf{u}_{n'}$ are the positions of unit cells, the summation involves all the unit cells in the crystalline material. If $\mathbf{u}_n - \mathbf{u}_{n'}$ and $n - n'$ are replaced by $\mathbf{x}_m$ and m, respectively, equation (2.2) can be written as

$$I(\mathbf{h}) = \sum_{n,m} |F|^2 \exp(2\pi i \mathbf{h} \cdot \mathbf{x}_m) \ . \tag{2.3}$$

In the imperfect crystal, $\mathbf{x}_m$ is decomposed into two displacement vectors, $\mathbf{R}_m$ and $\boldsymbol{\delta}_m$. $\mathbf{R}_m$ is the displacement of nth and n'th unit cells in the undistorted crystal, while $\boldsymbol{\delta}_m$ is an additional deviation due to the microstrains in the real crystal. With this the diffraction intensity becomes

$$I(\mathbf{h}) = \sum_{n,m} |F|^2 \exp(2\pi i \mathbf{h} \cdot \boldsymbol{\delta}_m) \exp(2\pi i \mathbf{h} \cdot \mathbf{R}_m) \ . \tag{2.4}$$

If the illuminated volume V is moved by $\mathbf{R}_m$, the common region of the volumes at the previous and new positions is $V \cdot V(\mathbf{R}_m)$, the double summation in equation (2.4) can be replaced by a single sum over m (Guinier, 1963; Warren, 1969):

$$I(\mathbf{h}) = \frac{V}{v_1} \sum_m V(\mathbf{R}_m) \, |F|^2 \langle \exp(2\pi i \mathbf{h} \cdot \boldsymbol{\delta}_m) \rangle \exp(2\pi i \mathbf{h} \cdot \mathbf{R}_m) \ , \tag{2.5}$$

where v_1 is the unit-cell volume.

Transform the summation into an integration, and ignore the factors before the integral sign for brevity,

$$I(\mathrm{s}) = \int V(t) y(t) \exp(2\pi i s t) \mathrm{d}t \ , \tag{2.6}$$

where $\mathrm{s} = 2(\sin\theta - \sin\theta_B)/\lambda$, θ is the diffraction angle corresponding to the scattering vector $\mathbf{h}$, θ_B is the exact Bragg angle corresponding to the diffraction vector $\mathbf{g}$, t is the projection of $\mathbf{R}_m$ along $\mathbf{h}$, and

$$V(t) = \int_0^\infty \left\{1 - \frac{|t|}{\mu}\right\} \mathrm{g}(\mu) \mathrm{d}\mu \ , \tag{2.7}$$

$$y(t) = |F|^2 \langle \exp(2\pi i g \mathrm{L}_t) \rangle \ , \tag{2.8}$$

where μ is the crystallite size, $\mathrm{g}(\mu)$ is the volume distribution function, L_t is the projection of $\boldsymbol{\delta}_m$ along $\mathbf{g}$.

Equations (2.6)-(2.8) show the diffraction intensity $I(\mathrm{s})$ is the Fourier transform (FT) of the product of $V(t)$ and $y(t)$. $V(t)$ and $y(t)$ are the coefficients related to the crystallite size and the distortions, respectively. For small values of g and L_t, equation (2.8) can be expanded by Taylor series and it will be

$$y(t) = |F|^2 (1 + 2\pi i g \langle \mathrm{L}_t \rangle - 2\pi^2 g^2 \langle \mathrm{L}_t^2 \rangle + \cdots) \ . \tag{2.9}$$

Here, the series expansion is taken up to second-order term, and the value of $\langle \mathrm{L}_t \rangle$ is zero. Define the microstrain $\varepsilon = \mathrm{L}_t / t$, equation (2.9) becomes

$$y(t) = |F|^2 (1 - 2(\pi g t)^2 \langle \varepsilon_t^2 \rangle) \ . \tag{2.10}$$

Since the size coefficient $V(t)$ is order independent, while distortion coefficient $y(t)$ is order dependent, two different effects of size and distortion can be separated. This procedure is usually called Warren-Averbach method (Warren, 1959, 1969).

On the other hand, according to equation (2.6) the diffraction intensity $I(\mathrm{s})$ can also be written as the convolution of $\mathrm{FT}\big(V(t)\big)$ and $\mathrm{FT}\big(y(t)\big)$:

$$I(\mathrm{s}) = \mathrm{FT}\big(V(t)\big) * \mathrm{FT}\big(y(t)\big) \ . \tag{2.11}$$

That means the whole diffraction profile can be modelled by the convolution of the size and distortion profiles. It's the fundament of the method of CMWP. The prior challenge in the CMWP procedure is establishing microstructure based theoretical models, which can accurately describe the effects of different microstructures on diffraction peaks.

With regard to crystallite size, average size, size distribution and crystallite shape should be considered. Especially, non-spherical crystallite shape will also influence the *hkl* dependence on diffraction peak broadening. In the Warren-Averbach method the

distortions in crystal are just evaluated phenomenologically. Actually, they are created by particular lattice defects. The characters of peak profile, including peak width, asymmetry and *hkl* dependence, are influenced by the linear and planar defects. Here, the linear and planar defects are specifically assigned as dislocations and stacking faults/twins, respectively. Both kinds of the defects are adopted in traditional LPA. On the contrary, the point defects produce diffuse scattering underneath diffraction peaks, which can be referred to the literature (Egami & Billinge, 2004). According to the correlation between diffraction peak shape and lattice defects, microstructural information can be obtained inversely from diffraction data.

2.2 Crystallite size

As shown in equation (2.7), the diffraction intensity profile is related to the crystallite size μ and the volume distribution $\mathrm{g}(\mu)$. All the crystallites in the material could be regarded as the compositions of the columns parallel to the diffraction vector **g**. The volume fraction of the columns with the length between μ and $\mu + \mathrm{d}\mu$ is $\mathrm{g}(\mu)\mathrm{d}\mu$. The calculation of $\mathrm{g}(\mu)\mathrm{d}\mu$ is dependent on the crystallite shape and the size distribution of the crystallites.

In order to describe properly the size distribution of the crystallites, several different a priori distribution functions, including the lognormal distribution, the Gamma distribution, and the York distribution, have been proposed, c.f. Ph.D. thesis of Ribárik (2008) and the literatures cited therein. The most widely used distribution function is the lognormal size distribution. It has been successfully applied to powder or polycrystalline materials (Hinds, 1982; Krill & Birringer, 1998; Langford et al., 2000; Ungár et al., 2001). The lognormal size distribution can be written as

$$f(x) = \frac{1}{\sqrt{2\pi}\sigma x}\exp\left\{-\frac{[\log(x/m)]^2}{2\sigma^2}\right\}, \qquad (2.12)$$

where m and σ are the median and the variance of the distribution. Additionally, a realistic crystallite shape should be known for determining the quantity of $\mathrm{g}(\mu)\mathrm{d}\mu$. If the crystallite shape is spherical, the size related peak broadening is independent on the *hkl* indices. If the crystallite shape is non-spherical, such as being ellipsoidal or polyhedral, the *hkl*-dependent peak broadening will be present. It is usually called

anisotropic size broadening.

In the following, the crystallite shape is assumed to be spherical and the lognormal size distribution is selected. The size coefficient $V(t)$ can be obtained as

$$V(t) = \int_{|t|}^{\infty} \left(1 - \frac{|t|}{\mu}\right) \mu^2 \left[\int_{\mu}^{\infty} f(x)\mathrm{d}x\right] \mathrm{d}\mu \ , \tag{2.13}$$

where x is the diameter of the crystallite, $f(x)\mathrm{d}x$ represents the number of the crystallites with the diameter between x and $x + \mathrm{d}x$. Since only the crystallites with the diameter not less than μ contribute to the volume distribution $\mathrm{g}(\mu)$, the lower limit of the integral of $f(x)\mathrm{d}x$ starts from μ. Inserting equation (2.12) into equation (2.13), $V(t)$ can be expressed as (Ribárik et al., 2001)

$$V(t) = \int_{|t|}^{\infty} (1 - |t|\mu) \mathrm{erfc}\left[\frac{\log(\mu/m)}{\sqrt{2}\sigma}\right] \mathrm{d}\mu \ , \tag{2.14}$$

where erfc is the complementary error function with the form of

$$\mathrm{erfc}(x) = \frac{2}{\sqrt{\pi}} \int_{x}^{\infty} \exp(-t^2)\mathrm{d}t \ . \tag{2.15}$$

The final integral in equation (2.14) can be calculated using substitutions and partial integration. The size coefficient $V(t)$ can be further written as (Ribárik et al., 2001)

$$V(t) = \frac{m^3 \exp\left[(9/4)\left(\sqrt{2}\sigma\right)^2\right]}{3} \mathrm{erfc}\left[\frac{\log(|t|/m)}{\sqrt{2}\sigma} - \frac{3}{2}\sqrt{2}\sigma\right]$$

$$- \frac{m^2 \exp\left(\sqrt{2}\sigma\right)^2}{2} |t| \mathrm{erfc}\left[\frac{\log(|t|/m)}{\sqrt{2}\sigma} - \sqrt{2}\sigma\right] + \frac{|t|^3}{6} \mathrm{erfc}\left[\frac{\log(|t|/m)}{\sqrt{2}\sigma}\right] \ . \tag{2.16}$$

Considering only the size effect of crystallite, the diffraction intensity profile is the inverse Fourier transform of equation (2.16). It can be determined as follows (Ribárik, et al., 2001):

$$I(s) = \int_{0}^{\infty} \mu \frac{\sin^2(\mu\pi s)}{(\pi s)^2} \mathrm{erfc}\left[\frac{\log(\mu/m)}{\sqrt{2}\sigma}\right] \mathrm{d}\mu \ . \tag{2.17}$$

The maximal values of the size coefficient $V(t)$ and the size intensity profile $I(s)$ are, respectively,

$$V(0) = \frac{2m^3 \exp\left[(9/4)\left(\sqrt{2}\sigma\right)^2\right]}{3} \quad , \tag{2.18}$$

and

$$I(0) = \int_0^\infty \mu^3 \mathrm{erfc}\left[\frac{\log(\mu/m)}{\sqrt{2}\sigma}\right] \mathrm{d}\mu \quad . \tag{2.19}$$

Two size parameters L_0 and d are obtained by the derivation of $V(t)$ and the integral of the size intensity profile $I(s)$, respectively.

$$L_0 = -\frac{V(0)}{[\mathrm{d}V(t)/\mathrm{d}t]_{t=0}} = \frac{2}{3} m \exp\left[(5/4)\left(\sqrt{2}\sigma\right)^2\right] \quad , \tag{2.20}$$

$$d = \frac{1}{\beta} = \frac{I(0)}{\int I(s)ds} = \frac{I(0)}{V(0)} = \frac{3}{4} m \exp\left[(7/4)\left(\sqrt{2}\sigma\right)^2\right] \quad . \tag{2.21}$$

In the case of spherical crystallites, the proportional relations are hold between the area and volume weighted average crystallite sizes and the size parameters d and L_0, respectively (Hinds, 1982).

$$\langle x \rangle_{area} = \frac{\sum_i A_i d_i}{\sum_i A_i} = \frac{3}{2} L_0 = m \exp\left[(5/4)\left(\sqrt{2}\sigma\right)^2\right] \quad , \tag{2.22}$$

$$\langle x \rangle_{vol} = \frac{\sum_i V_i d_i}{\sum_i V_i} = \frac{4}{3} d = m \exp\left[(7/4)\left(\sqrt{2}\sigma\right)^2\right] \quad . \tag{2.23}$$

2.3 Dislocations

In the distorted crystalline materials, the displacements of the atoms from their ideal positions are assumed to be random by Warren and Averbach (1950). The analysis shows that diffraction peak broadening is proportion to the mean square strain $\langle \varepsilon^2 \rangle$.

Further, Krivoglaz and Ryaboshapka (1963) considered the case that lattice strains are created by randomly distributed dislocations. For the crystal with a size *D*, they derived an approximate expression of $\langle \varepsilon_t^2 \rangle$ at small values of Fourier variable t,

$$\langle \varepsilon_t^2 \rangle = \left(\frac{b}{2\pi}\right)^2 \pi\rho C \ln(D/t) \ , \tag{2.24}$$

where ρ, b, and C are the average density, the Burgers vector and the contrast factor of the dislocations, respectively. It can be found the logarithmic term in equation (2.24) is diverged with increasing the crystal size.

Wilkens realized firstly the problem is similar to the logarithmic singularity in the elastic stored energy of dislocations (Wilkens, 1969). Due to the correlation between the dislocations, the dislocation distribution is "restrictedly random". Wilkens introduced a parameter, the effective outer cut-off radius of dislocations, R_e, to replace the crystal size D. The dislocations are assumed to be randomly distributed in the separate regions with the radius R_e. Outside of the regions the interactions between the dislocations are screened off. In use of the scheme, Wilkens (1970a) obtained successfully the analytical expression of the mean square strain in the entire range of Fourier variable t. The expression can be given as

$$\langle \varepsilon_t^2 \rangle = (b/2\pi)^2 \pi\rho C f(t/R_e^*) \ , \tag{2.25}$$

where $R_e^* = \exp(-2)R_e$, $f(t/R_e^*)$ is the Wilkens function. The complete form of the Wilkens function is as follows:

If $\eta \leq 1$,

$$f^*(\eta) = -\log\eta + \left(\frac{7}{4} - \log 2\right) + \frac{512}{90\pi}\frac{1}{\eta} + \frac{2}{\pi}\left(1 - \frac{1}{4\eta^2}\right)\int_0^\eta \frac{\arcsin V}{V}\mathrm{d}V$$

$$-\frac{1}{\pi}\left(\frac{769}{180}\frac{1}{\eta} + \frac{41}{90}\eta + \frac{2}{90}\eta^3\right)(1-\eta^2)^{1/2} - \frac{1}{\pi}\left(\frac{11}{12}\frac{1}{\eta^2} + \frac{7}{2} + \frac{1}{3}\eta^2\right)\arcsin\eta + \frac{1}{6}\eta^2 \ ; \tag{2.26}$$

If $\eta \geq 1$,

$$f^*(\eta) = \frac{512}{90\pi}\frac{1}{\eta} - \left(\frac{11}{24} + \frac{1}{4}\log 2\eta\right)\frac{1}{\eta^2} \ ,$$

where $\eta = (1/2)\exp(-\frac{1}{4})(t/R_e^*)$.

The Wilkens function in the entire η range is shown in Fig. 2.1. At small values of η, the Wilkens function is asymptotically logarithmic; with increasing the values of η, it's much closer to a hyperbola. For comparison, the logarithmic and the hyperbolic parts of the Wilkens function are also shown in Fig. 2.1.

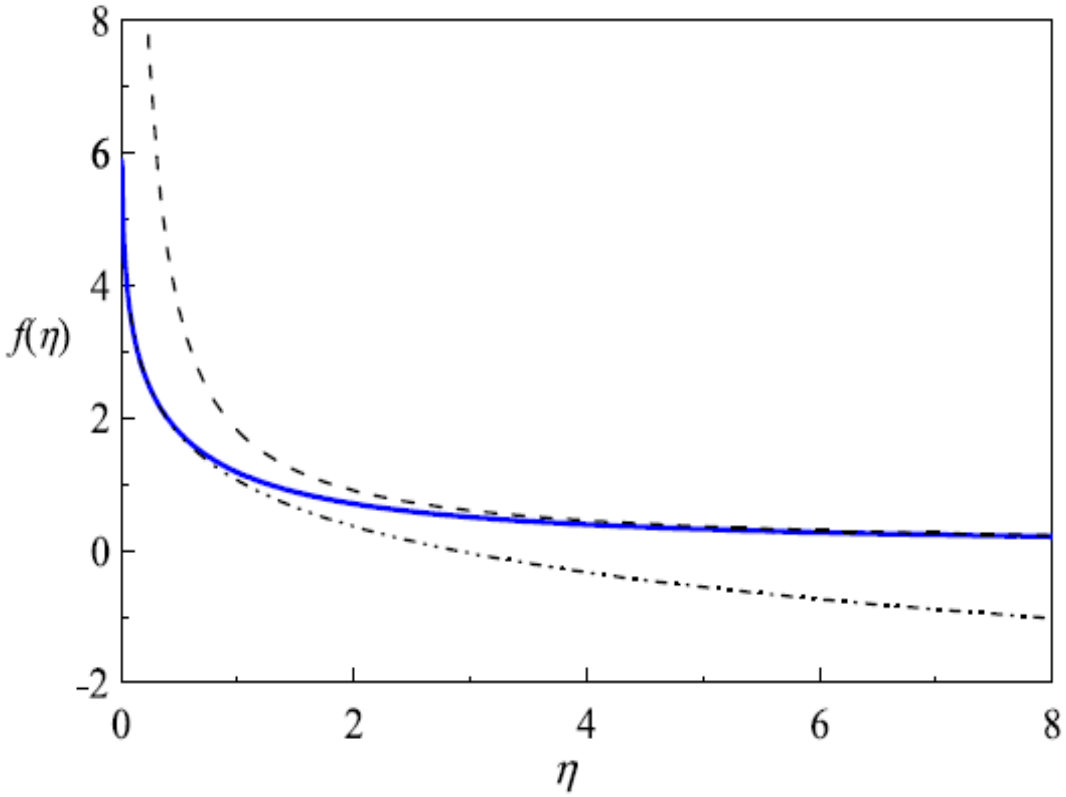

Fig. 2.1: The Wilkens function in the entire η range, the dash-double-dot line describes a logarithmic function and the dashed line is for a hyperbolic function. Reproduced from Fig. 2(a) in Ref. (Bobéry & Ungár, 2012).

Inserting equation (2.26) into (2.8), the strain Fourier coefficient can be written as

$$y(t) = |F|^2 \exp[-(\pi b^2/2)(g^2 C)\rho L^2 f(t/R_e^*)] \ . \qquad (2.27)$$

The Fourier transform of equation (2.27) is the strain intensity profile. Its shape is correlated directly with the dislocation arrangement. For characterizing the distribution of dislocations, Wilkens (1970b) proposed a dimensionless parameter: $M = R_e\sqrt{\rho}$. In the case of large values of M, the dislocations populate more randomly, and the dipole character is weak; in the case of small values of M, the dislocations correlate more

closely, and the dipole character is strong. The strength of the dipole character is related to the screening of the strain field of dislocations. Fig. 2.2 shows if the M parameter is smaller or larger than the unity, the diffraction peak shape will be closer to Lorentzian or Gaussian type function, respectively.

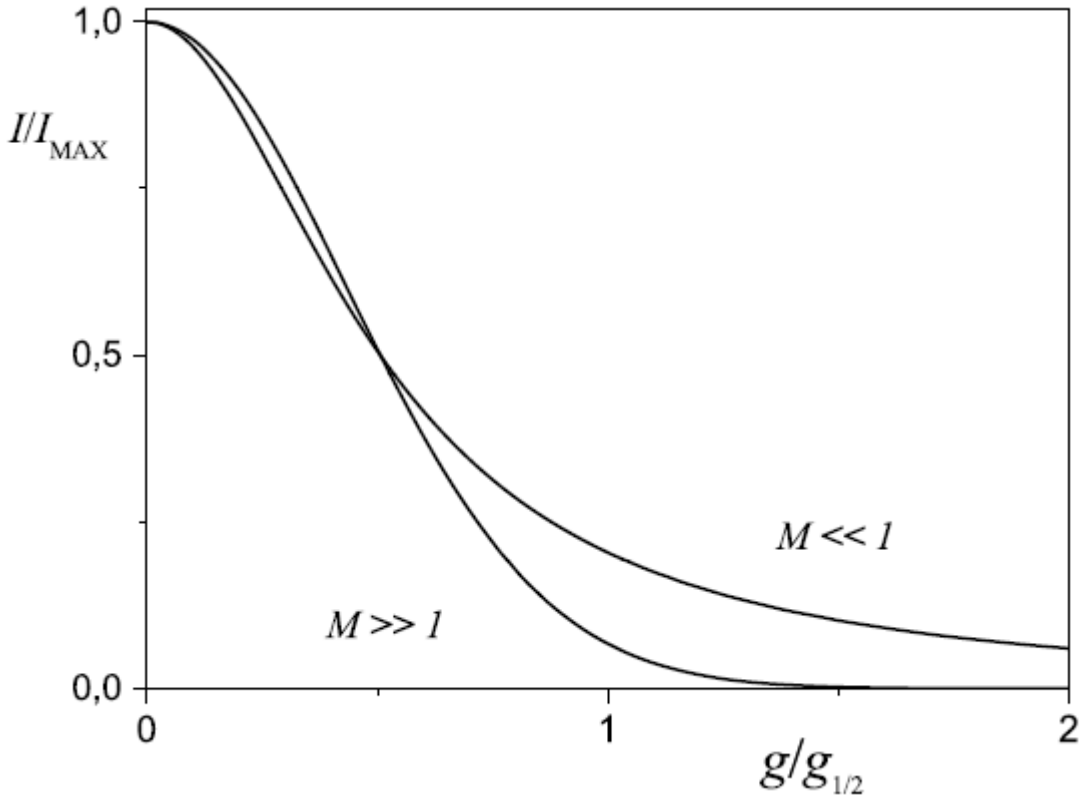

Fig. 2.2: The normalized strain profile, M is the parameter for dislocation arrangement. Reproduced from Fig. 2(b) in Ref. (Bobérly & Ungár, 2012).

The *hkl* dependence of $\langle \varepsilon_t^2 \rangle$ is usually called strain anisotropy, which means neither the breadths not the Fourier coefficients of the distortion related diffraction profiles are monotonous functions of diffraction angle (Ungár & Borbély, 1996). Strain anisotropy can be in connection with diffraction effect of dislocations or dislocation-like lattice defects. In equation (2.25), it is described by the contrast factor C.

The contrast factor, C, of a single dislocation can be written as (Borbély et al., 2003)

$$C = \frac{1}{\pi}\int_0^{2\pi} F^2(\varphi)\mathrm{d}\varphi \ , \qquad (2.28)$$

where $\mathrm{F}(\varphi)$ is a function depending on the elastic constants of the crystal and on the relative orientation of the diffraction vector, the Burgers vector and the line vector of the dislocation. The function $\mathrm{F}(\varphi)$ can be written as

$$\mathrm{F}(\varphi) = \sum_{i=1}^{3}\sum_{j=1}^{2}\gamma_i\gamma_j\beta_{ij}(\varphi) \ , \tag{2.29}$$

where γ_i and γ_j are the direction cosines of the diffraction vector with regard to the axes of the slip coordinate system, $\beta_{ij}(\varphi)$ is the angular part of the distortion tensor, which is obtained from the gradient of the displacement field u:

$$\beta_{ij}(\varphi) = \frac{2\pi r}{b}\frac{\partial u_i}{\partial x_j} \ , \tag{2.30}$$

where u can be calculated according to the anisotropic elasticity theory of solids. The expression of u is given by (Borbély et al., 2003)

$$u_k = \frac{1}{\pi}\sum_{\alpha=1}^{3} A_{k\alpha}D_\alpha \ln(x_1 + p_\alpha x_2) \ , \tag{2.31}$$

where p_α are the roots with positive imaginary parts of the sextic equation, $A_{k\alpha}$ and D_α are the functions of the roots p_α and the second-order elastic constants of the crystal.

If the sample is a texture free polycrystal or an ideal powder specimen, the contrast factor for a particular reflection has to be obtained by averaging over all the possible *hkl* permutations. For the crystals with equally populated dislocations of all possible slip systems, the same averaging also holds. As shown in equation (2.25), the contrast factor C is proportional to the mean square strain $\langle\varepsilon_t^2\rangle$. It can be written as

$$C \propto \left\langle\left[\frac{\partial}{\partial\xi}(\mathbf{gu})/\mathrm{g}\right]^2\right\rangle = \left\langle\left(\frac{\mathbf{g\beta g}}{\mathrm{g}^2}\right)^2\right\rangle \ . \tag{2.32}$$

Since g^4 is a fourth order invariant of the *hkl* indices, the average of $C\mathrm{g}^4$ over the *hkl* permutations can be expressed as a linear function of all the fourth order invariants (Ungár & Tichy, 1999).

For cubic crystals, $\bar{C}$ is (Ungár et al., 1999):

$$\bar{C} = \bar{C}_{h00}(1 - qH^2) \ , \tag{2.33}$$

where $\bar{C}_{h00}$ is the average dislocation contrast factor of $h00$ reflections, and

$$H^2 = \frac{h^2k^2+h^2l^2+k^2l^2}{(h^2+k^2+l^2)^2} \ . \tag{2.34}$$

For hexagonal crystals, $\bar{C}$ is (Dragonir & Ungár, 2002):

$$\bar{C} = \bar{C}_{hk0}(1 + q_1x_1^2 + q_2x_2^2) \ , \tag{2.35}$$

where $\bar{C}_{hk0}$ is the average dislocation contrast factor of $hk0$ reflections, $x = (2/3)(l/ga)^2$, a is the lattice constant in the basal plane.

Because of the concision of the forms, equations (2.33) and (2.35) can be conveniently incorporated into whole profile fitting procedures (Ungár et al., 2001; Scardi & Leoni, 2002). Strain anisotropy peak broadening caused by dislocations provides measured values of the q parameter or the q_1 and q_2 parameters. The q parameter or the q_1 and q_2 parameters are the constants for all reflections, and depend on the elastic constants of the crystal and the dislocation characters. A program ANIZC developed by Borbély et al. (2003) can be used to calculate the theoretical values of the individual or average contrast factors. Based on the calculated values of the average contrast factors, the parameters C_{h00}, q, and C_{hk0}, q_1 and q_2 have been evaluated numerically and compiled for cubic and hexagonal crystals, respectively (Ungár et al. 1999; Dragomir & Ungár, 2002). Comparing the measured and the theoretical values of the q parameter or the q_1 and q_2 parameters, one can obtain slip activity of dislocations in cubic and hexagonal crystals, respectively. In the case of single crystals or textured materials, if the slip systems are not randomly distributed, the individual contrast factors will be applied instead of the average contrast factors (Cordier et al., 2004; Ribárik & Ungár, 2010).

2.4 Practical usage of CMWP

In Section 2.1, the kinematical theory of X-ray diffraction in imperfect crystals are briefly reviewed. To simulate diffraction line profiles, various microstructural models have been well established. The effects of crystallite size and dislocations on diffraction pattern are presented in Sections 2.2 and 2.3, respectively. Inversely, from a whole diffraction pattern the microstructural information can be deduced using ab initio theoretical functions. For this purpose, a computer program of Convolutional Multiple Whole Profile (CMWP) fitting has been developed (Ribárik et al., 2004). It can be downloaded via webpage: http://www.renyi.hu/cmwp after a user registration. In the CMWP program, the calculated diffraction pattern is the convolution of all the microstructural and the instrumental profiles, which can be matched directly to the measured pattern. In the end of the fitting procedure the microstructural parameters such as crystallite size, dislocation density and probabilities of planar defects can be determined.

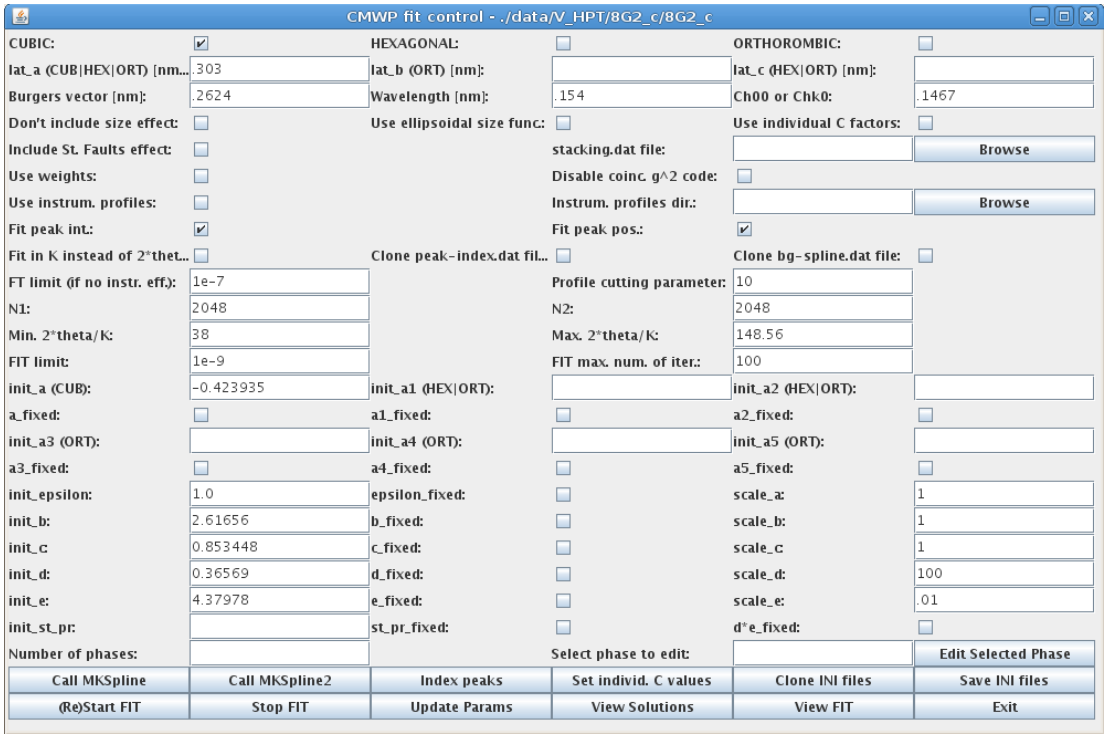

Fig. 2.3: The main control panel of the CMWP program.

The main control panel of the CMWP program is shown in Fig. 2.3. Using the graphic interface, it's convenient to input the microstructure and configuration parameters for

the evaluation. The function of any specific application can be activated by clicking the corresponding button. The diffraction data should be prepared in form of whole pattern for the CMWP program. It's unnecessary to separate overlapping diffraction peaks or eliminate instrumental broadening in the measured pattern. If a pattern is broken by several blank intervals, these intervals should be filled with artificial intensity. The background of the diffraction pattern is determined by invoking a program MKSpline. Using this program, the base points of the background can be selected interactively, then a background spline will be created. The background spline is allowed to adjust again when the iterations of CMWP are converged or stopped. The indices, positions and intensities of all peaks in a diffraction pattern are determined by using a program IndexPeaks. The peak intensities and positions will be refined during the evaluation of CMWP, if the corresponding options are selected. If the resolution of the diffractometer is not too high to ignore, the instrumental effect can be corrected in the CMWP procedure. For this, the directory of instrumental profiles can be selected by clicking the relevant button "Browse".

Depending on the crystal system and the physical origin of peak broadening, the input parameters should be specified. The initial values of these parameters need to be given before the nonlinear least squares refinement. In general, if the primary sources of peak broadening are crystallite size and dislocations, the theoretical models of line profiles can be simplified. For the spherical crystallites with lognormal size distribution, two parameters, the median, m, and the logarithmic variance, σ, are needed to define the size distribution function. The mean square strain is described by using the dislocation density, ρ, the dislocation arrangement parameter, M, and the contrast factor, C. If the specimen is a random powder or a texture free bulk polycrystal, or the possible slip systems are equally populated, the average contrast factor $\bar{C}$ is given in terms of the parameters $\bar{C}_{h00}$ and q for cubic crystals, or $\bar{C}_{hk0}$, q_1 and q_2 for hexagonal crystals. These microstructure parameters are used to construct the theoretical diffraction pattern, and are refined during the fitting procedure. In the other particular cases, the number of the parameters may be increased. For example, if the crystallites are of ellipsoidal shape, the ellipticity parameter ε should be taken into account; for single crystals or strongly textured specimens, the individual dislocation contrast factor C_{hkl} of each reflection will be applied.

Additionally, the effects of planar defects on the diffraction pattern are also considered systematically in CMWP (Balogh et al., 2006, 2009). Therefore, the intensity profile is extended to be the convolution of the profiles of crystallite size, dislocations and planar defects. The line profile of planar defects is composed of several types of subreflections, and the peak shape of each subreflection is *hkl* dependent. The diffraction peaks have been simulated by Balogh et al. (2006, 2009) using the program DIFFAX for stacking faults and twins in *fcc* crystals and the common twinning systems in *hcp* crystals, respectively. For *fcc* crystals, the subreflections can be classified into one or more groups. The group of subreflections unaffected by planar defects is a delta function, the other groups are Lorentzian functions. The full widths at half maxima (FWHM) and the shifts of the subreflections can be expressed as fifth order polynomials, in which the variable is the probability of intrinsic or extrinsic stacking faults or twin boundaries (Balogh et al., 2006). For *hcp* crystals, four common twinning systems, including {10.1}<10.2> and {11.2}<11.3> compressive twinning and {102.}<10.1> and {11.1}<11.6> tensile twinning, are taken into account. The intensity profile of twinning is found to be the sum of symmetrical and antisymmetrical Lorentzian functions. The antisymmetrical Lorentzian function results from the interference between two overlapping subreflections corresponding to the parent and the twin crystal, respectively. The FWHMs and the the antisymmetry parameter A have also been parameterized as fifth order polynomials of twinning probability (Balogh et al., 2009). The fractions and the coefficients of the fifth order polynomials of each type of subreflections have been evaluated and deposited at http://metal.elte.hu/~levente/stacking for *fcc* and *hcp* crystals, respectively. These data files have been incorporated into the CMWP program and can be used to determine the probability of stacking faults or twin boundaries in materials.

In the scheme of the CMWP program, the Fourier coefficients of the theoretical physical profiles and the measured instrumental profiles are multiplied. The calculated intensity profile is expressed as the inverse Fourier transform of the product of the Fourier coefficients. The measured diffraction pattern is matched by the calculated diffraction pattern using the Marquardt-Levenberg fitting algorithm. There're two parameters used as the limits of stopping: one is the relative change of the weighted-sum-of–squared-residuals (WSSR) between two iteration steps, the other is the maximal number of iterations. Once anyone of the criteria is reached, the evaluation

procedure will stop. The microstructural information about crystallite size, dislocations, and even stacking faults and twins will be provided by the CMWP program. Therein, the average contrast factor $\bar{C}$ in terms of q for cubic crystals, or q_1 and q_2 for hexagonal crystals can be used to determine the fraction for the active dislocation slip systems. In the case of *fcc* or *bcc* crystals, there is usually one type of slip system. The fraction of the edge or the screw dislocation is obtained analytically from the measured parameter q. In the case of *hcp* crystals, there're totally 11 sub-slip systems and just two measured parameters q_1 and q_2. In order to determine the fractions of the dislocation systems, a program has been developed to examine all possible combinations of the sub-slip systems (Máthis et al., 2004; Ungár et al., 2007). The measured and the calculated values of q_1 and q_2 were compared for each combination. The combination will be accepted if the difference of the measured and the calculated q_1 and q_2 values is less than the specific tolerance. Then the fractions of the populations of the $\langle a \rangle$, $\langle c \rangle$ and $\langle c+a \rangle$ Burgers vector types can be counted. Using the fractions and the theoretical C_{h00} or $C_{hk0}b^2$ of each active slip system, the average value of C_{h00} or $C_{hk0}b^2$ for all the active slip systems will be obtained. As shown in equation (2.25), the mean square strain is given by the product of $\rho\overline{Cb^2}$ in the program CMWP. If the value of $\overline{Cb^2}$ is already known, the true dislocation density ρ will be naturally determined.

Chapter 3

Nuclear materials for fission and fusion reactors

3.1 Nuclear fission and fusion reactions

Energy of nuclear power releases from nuclear reactions taking place in a nuclear reactor, which is similar to that thermal energy comes from burning fossil fuels in a conventional thermal power station. The origin can be explained directly by the formula of mass-energy equation, $\Delta E = \Delta mc^2$, where ΔE is binding energy, c is light speed, Δm is mass difference (Whittle, 2016; De Sanctis et al., 2016). The mass of any nucleus is always less than the total mass of constituent nucleons. If the constituent nucleons are separated completely from a nucleus, the energy equal to Δmc^2 needs to be absorbed. In contrast, if the nucleons combine into a nucleus, the binding energy ΔE will be released. The average binding energy ε is obtained from the division of the binding energy ΔE and the nucleon number A. It is also denoted as the specific binding energy, $\varepsilon = \Delta E/A$. The relation curve of the specific binding energy ε vs. the number of nucleon A is shown in Fig. 3.1. As illustrated in the figure, the ε value increases approximately with nucleon number in the range of light nucleus; it reaches a maximum value, ~8.8 MeV, in the range of medium nucleus; then, it drops again in the range of heavy nucleus. The fluctuation of the curve of the specific binding energy is just the physical base of two different kinds of nuclear reactions as described below.

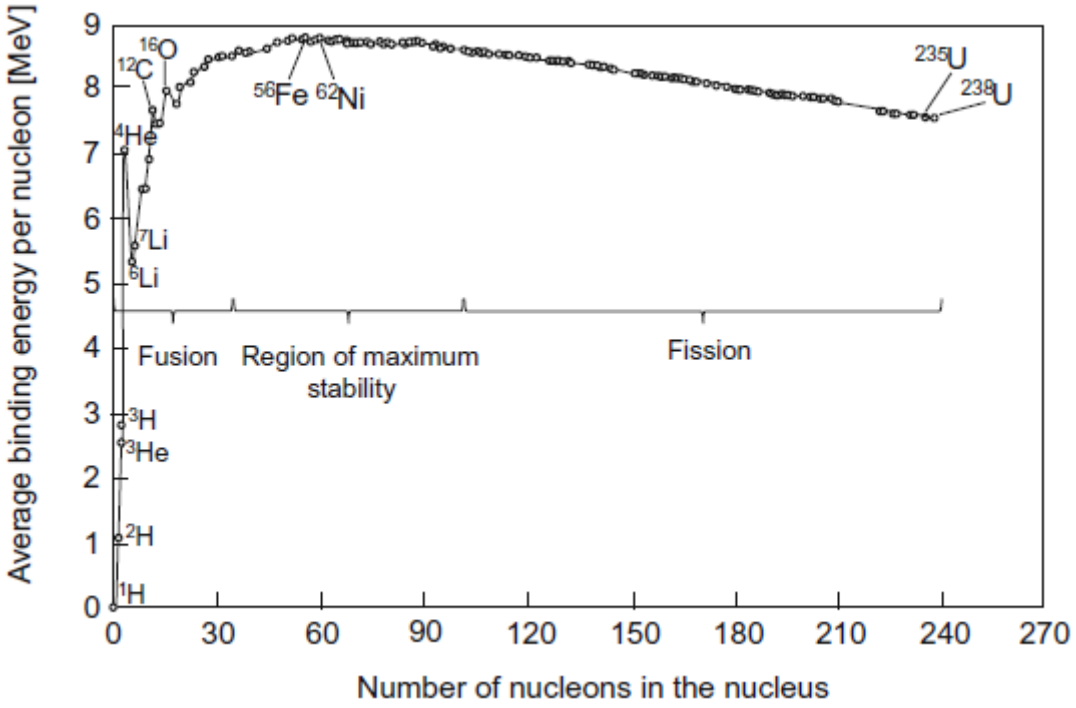

Fig. 3.1: The specific binding energy for the elements. Reproduced from Fig. 1.8 in Ref. (De Sanctis et al., 2016).

The specific binding energy of heavy nucleus is less than that of medium nucleus, which indicates the energy can be released when a heavy nucleus splits into two medium nuclei. Such a reaction is called nuclear fission reaction. For example, as a heavy nucleus, ^{235}U has a comparably small ε value of ~7.6 MeV. If ^{235}U absorbs a neutron, it will split into two medium nuclei and 2~3 neutrons, and meanwhile a large amount of energy, ~214 MeV, will be released. The fission reaction can be expressed as

$$^{235}U + n \rightarrow X_1 + X_2 + (2\sim3)n + Q \quad ,$$

where X_1, X_2 and 2~3 neutrons are fission products of two medium nuclei, Q is released fission energy. The products of fast neutrons will be moderated to thermal neutrons. And one thermal neutron can induce a new fission reaction. Thus, the process of the fission reaction will continue, which is known as nuclear fission chain reaction, as illustrated schematically in Fig. 3.2. The chain-like fission reaction can be kept stable in a controllable manner, which means the losing and the producing of neutrons are nearly equal in reactor. Finally, the released energy from the chain-like reaction will be converted by a cooling system.

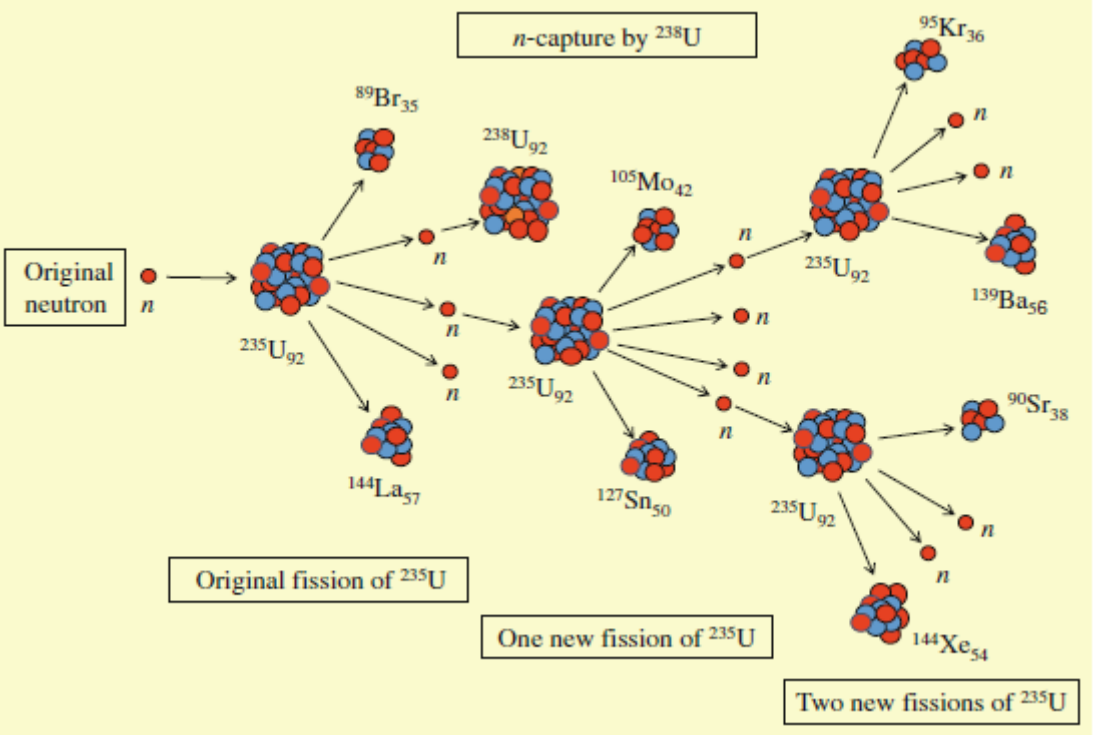

Fig. 3.2: A chain reaction induced by nuclear fission of ^{235}U. Reproduced from Fig. 3.5 in Ref. (De Sanctis et al., 2016).

The specific binding energy rises in the range of light nucleus. If two lighter nuclei combine into a heavier nucleus, the energy will be released. Such a reaction is called nuclear fusion reaction. As shown in Fig. 3.1, the specific binding energy increases dramatically, which means fusion energy must be huge. For example, the released energy of (*D*, *D*) and (*D*, *T*) fusion is 3.6 MeV for each nucleon, which is ~3 times higher than that of fission reaction. Some typical fusion reactions are listed as follows,

$$^2D + {}^2D \rightarrow {}^3T + P + 4.04\ \text{MeV}\ ,$$
$$^2D + {}^2D \rightarrow {}^3He + n + 3.27\ \text{MeV}\ ,$$
$$^2D + {}^3T \rightarrow {}^4He + n + 17.58\ \text{MeV}\ ,$$
$$^2D + {}^3He \rightarrow {}^4He + P + 18.34\ \text{MeV}\ ,$$

where ^2D is deuton, ^3T is triton, n is neutron, P is proton. During the fusion reaction, a heavier nucleus and a particle will be produced accompanying with kinetic energy. Because of positive charge of nucleus, coulomb repulsive force makes the occurrence of fusion reaction extremely difficult. Initial kinetic energy of fuel elements needs to be

provided in order to drive atoms to close each other. One of available methods is heating fuel elements to extraordinarily high temperature above millions Celsius degrees. These fuel elements will be ionized into a hot cloud of positive ions and electrons. The cloud should be constrained in a high vacuum and enclosed space, which is normally called the state of high-temperature and high-density plasma. Fusion reaction can be realized in such a state. For the confinement of plasma, a magnetic field is widely used. Therefore, it's well known as magnetic confinement fusion.

3.2 Materials for nuclear fission reactor

Nuclear reactor is one kind of equipment carrying out nuclear reactions in controllable manner. The released energy of nuclear fission reaction could be harnessed to drive a steam turbine for producing electricity. Since the first nuclear power plant was constructed in 1954, various types of civil nuclear reactors have been proposed and built all over the world (Hoffelner, 2013; Whittle, 2016; De Sanctis et al., 2016; Collum, 2017). Currently, commercial nuclear reactor includes pressurized water reactor (PWR), boiling water reactor (BWR), heavy water reactor (HWR) and so on. Figs. 3.3 and 3.4 show schematically the structure of power stations of PWR and BWR, respectively. It's noted that PWR is of most favorable and mature reactor type. According to the annual report RDS2 of IAEA (2018), PWR has a proportion of ~65% in all nuclear power plants and ~70% in gross power of nuclear electricity, respectively. PWR is composed of reactor core, fuel element, control rod, moderator, reflector, coolant, pressure vessel, containment, shielding layer and structural components etc.

Nuclear power plant can be understood as a strong field full of neutrons, heat flow and high pressure. The operation stability of power plant is highly dependent on the performance of the components. However, the service conditions are not the same for all the components, the requirement of materials for each component is therefore different. For three typical types of reactors, PWR, BWR and HWR, the main components and the corresponding materials are listed in Table 3.1.

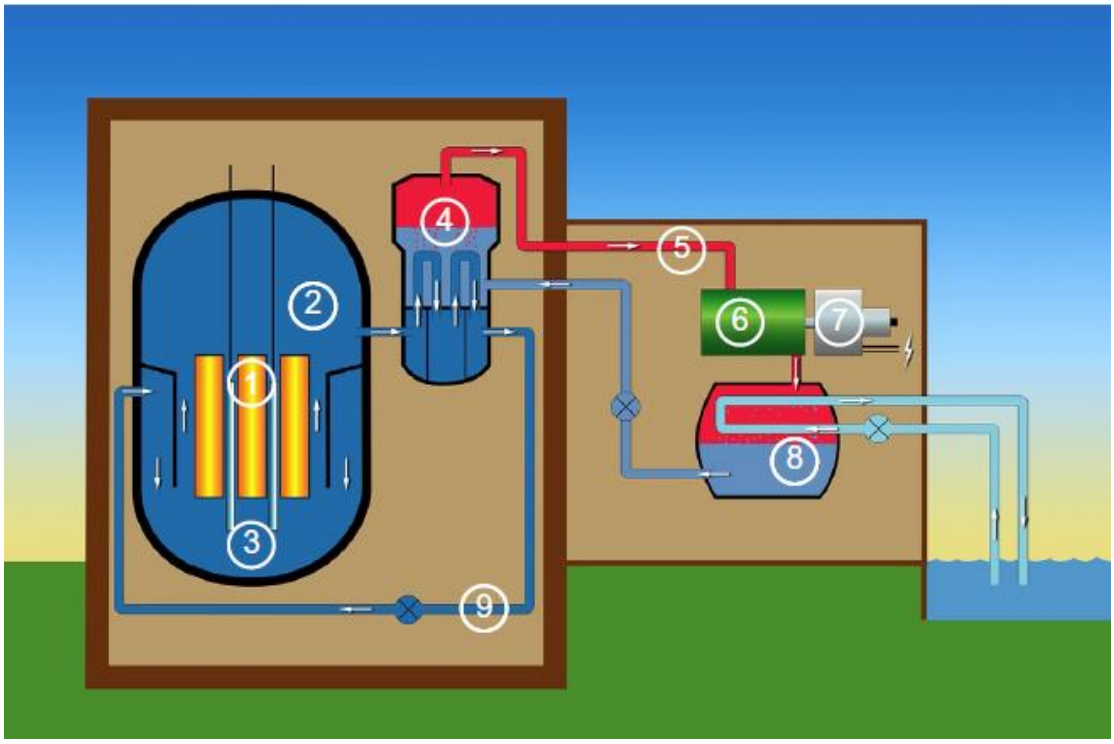

Fig. 3.3: Schematic diagram of pressurized water reactor. 1: fuel, 2: pressurized water, 3: control rods, 4: steam generator, 5: steam, 6: turbine, 7: electricity generator, 8: condenser, 9: water. Reproduced from Fig. 1.15 in Ref. (Collum, 2017).

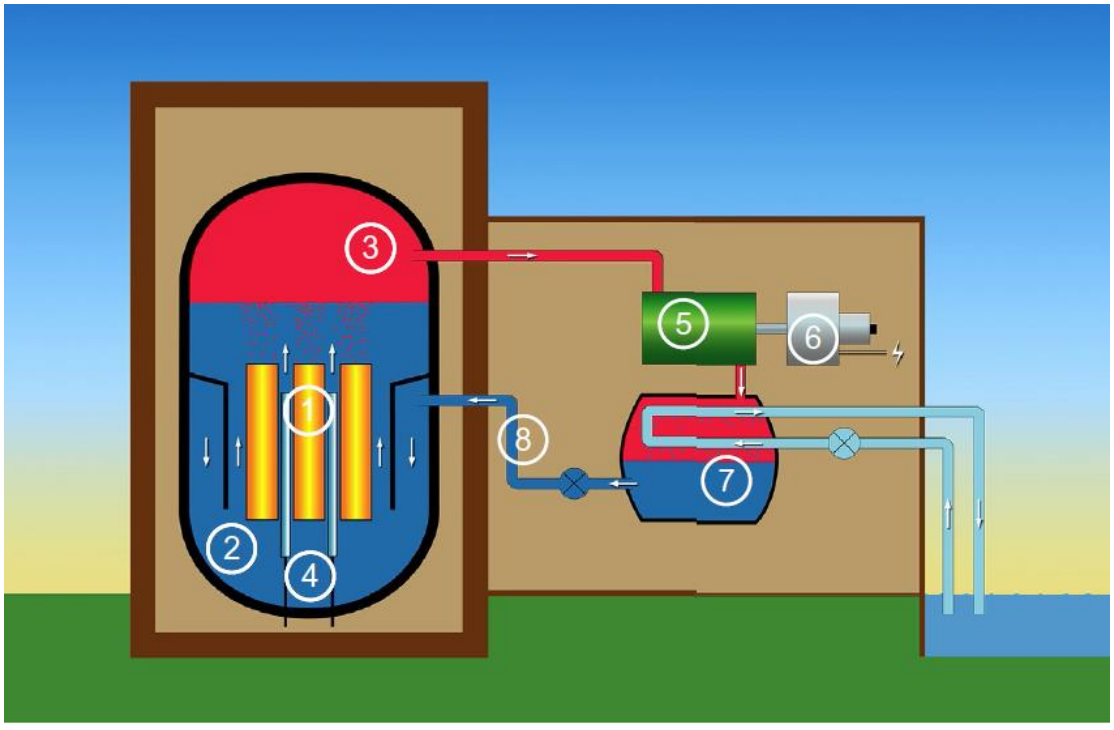

Fig. 3.4: Schematic diagram of boiling water reactor. 1: fuel, 2: boiling water, 3: steam, 4: control rods, 5: turbine, 6: electricity generator, 7: condenser, 8: water. Reproduced from Fig. 1.17 in Ref. (Collum, 2017).

Table 3.1: The main components and the corresponding materials in PWR, BWR and CANDU.

Component	Materials		
	PWR	BWR	CANDU
Fuel	low enriched UO_2	low enriched UO_2	natural UO_2
Cladding	Zr-4	Zr-2	Zr-4
Control rods	AgInCd/316 SS	B_4C/304 SS	Cd/316 SS
Moderator	H_2O	H_2O	D_2O
Coolant	H_2O	H_2O	D_2O
Pressure vessel	A533B, $A508_3$	A533B	Zr-2.5Nb
Loop pipe	304 SS, 316 SS	304 SS	304 SS

The elements, including ^{235}U, ^{233}U and ^{239}Pu, are easily fissionable. However, it is just ^{235}U that exists naturally. The abundance of ^{235}U in natural uranium is 0.714% (Whittle, 2016). Low-enrichment uranium oxide is generally used as nuclear fuel in PWR and BWR, while natural uranium oxide is used in HWR. The nuclear fuels are loaded into a set of sealed tubes, which is arranged as a nuclear fuel assembly in the reactor core. Once the reactor starts, sustainable chain-like fission reactions take place in the nuclear fuel assembly.

The functions of the sealed tubes are preventing the fission products from escaping, avoiding the fuels to be corroded by the coolant, and transferring the heat effectively. For reaching these aims, the cladding materials need to fulfill some requirements on the aspects of the nuclear properties, the thermal conductivity, the stability of tube dimension, and the compatibility between either the fuels or the coolant. Zircaloys such as Zr-2, Zr-4 and Zr-2.5Nb are consistent well with these requirements, and widely used as the structural materials in water-cooled reactor.

During the operation of the reactor, the reactivity is given as an indication parameter for the deviation from the critical status of the reactor. For adjusting the value of the reactivity, the control rod is applied. It's made of the elements, like B, or Cd, or Hf, with a large cross section of neutron absorption. If the control rod is inserted in or extracted from the reactor core, the reactivity will be changed corresponding to the

start-up, the normal running or the shutdown of the reactor.

The released energy of nuclear reaction needs to be brought out by the coolant of the primary loop. The suitable coolant is usually light water or heavy water in water-cooled reactor. In addition, in order to increase the probability of fission reaction and reduce the loss of neutrons, water can also be used as the moderator or the reflector. For the pressurized water reactor, the coolant keeps unboiling state under the pressure of 14~16 MPa. The primary loop and the pressure vessel are critical for enclosing the irradiated coolant with high temperature and high pressure. The hot circulating-water of the primary loop flows into the steam generator, then the thermal energy is transferred to the secondary loop. The water in the secondary loop becomes boiling and converts into steam. The steam rotates the turbine blade with high speed, then the electricity is generated continuously.

3.3 Materials for nuclear fusion reactor

Nuclear fusion reactor is a device designed for the controlled thermonuclear fusion power. So far different concepts of fusion reactor, like magnetic confinement, inertial confinement and a few others, have been proposed and investigated over years. One of the leading designs is tokamak. In the tokamak device, a high intensity of magnetic field with a configuration of torus is provided for the confinement of a hot plasma. Fig. 3.5 illustrates schematically the basic components of the tokamak fusion device. It consists of first wall, divertor, blanket, and magnetic field system.

The thermonuclear material, including D, T and ^{3}He, can be used as the fusion fuel. Nuclear fusion reaction is implemented via one of the routes of (D, D), (D, T) and (D, ^{3}He). (D, T) reaction is considered primarily in the design of a fusion reactor since it's practically easiest to occur in all the routes. In the reactor core, the fuel is heated to a plasma state, then the fusion reaction takes place accompanying with a huge amount of energy.

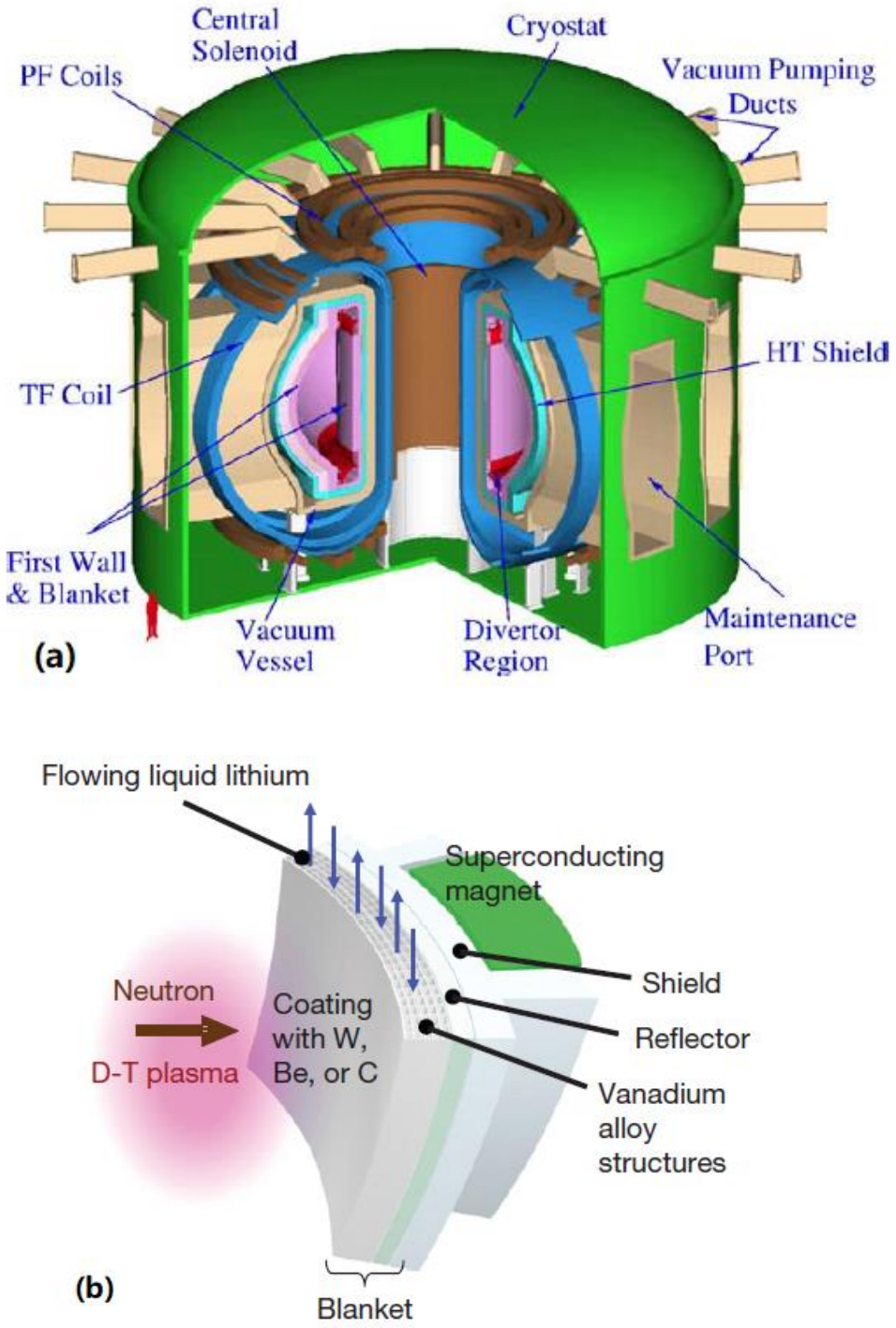

Fig. 3.5: Structure of a fusion reactor (a) and a self-cooled Li blanket with vanadium alloy (b). Reproduced from Fig. 1 in Ref. (Najmabadi et al., 2006) and Fig. 1 in Ref. (Muroga, 2012), respectively.

The first wall is the component closest to the plasma in the fusion reactor, which will interact directly with high energy neutrons and other irradiations. The surface of the first wall is composed of plasma facing material. Usually, the low atomic number material, such as graphite or beryllium, is chosen as the plasma facing material. Its role is to prevent the erosion of the structural material and the contamination of the plasma. Escaping plasma and impurities will be collected by a divertor. The thermal load of the divertor is one order higher than that of the surface of the first wall. The high-thermal-load part of the divertor could be made of one of Cu, Mo and Nb alloys.

Surrounding the reactor core there's a blanket. It is composed mostly of structural material, tritium breeding material and coolant. For the structural material, vanadium alloys, SiC/SiC composites and low activation ferritic and martensitic steels are competitive candidates. Because of excellent high-temperature strength, and better resistance to creep and irradiation swelling, vanadium alloys have been received considerable attentions. Tritium breeding material could be the material containing Li, such as ceramic material, liquid metal, molten salt, or the solution of lithium salt. Via the reaction of ^{6}Li(n, α)T, tritium can be produced and provided as the fusion fuel. Thus, one of the important roles of the blanket is tritium breeding. Additionally, the blanket can also be used to transfer the energy from fusion reaction to generate electricity. The coolant could be water, helium, molten salt or liquid metal.

3.4 Microstructure of zirconium alloys

As mentioned in Section 3.2, due to low absorption of thermal neutrons, comprehensive mechanical performance and acceptable corrosion resistance, zirconium alloys are used prevalently in a water-cooled reactor (Lemaignan, 2012). For instance, cladding, pressure and calandria tubes are made of one of zirconium alloys such as Zr-2, Zr-4 or Zr-2.5Nb (Lemaignan & Motta, 1994). Usually, the manufacturing of zircaloy tubes includes rolling, heat treatment and pilgering (Holden et al., 2006, Gurao et al., 2014; Singh et al., 2015). During the manufacturing process, different kinds of microstructure, like texture and dislocations, could be introduced in the final product (Tenckhoff & Rittenhouse, 1970; Holden et al., 2002; Gloaguen et al., 2014). The circumstance of a running reactor is complex, in which the structural components should experience cyclic loadings of stress and heat flux. The initial and the evolution of the

microstructure are unavoidable to influence the in-service performance of the components (Tomé et al., 1996; Castelnau et al., 2001). Besides that, irradiation damages should be considered specifically for the long-term operation of a reactor. For zirconium alloys, two types of dislocation loops, <a>- and <c>-type loops, are gradually formed due to neutron irradiation (Onimus & Béchade, 2012). The dislocation loops can further impede the movement of dislocations. Correspondingly, the strength of the zircaloy tubes increases, while the ductility decreases (Grossbeck, 2012). At high fluence of neutrons, the dimension of zirconium fuel cladding can exhibit instability and even result in failure. In addition, hydride embrittlement of zirconium alloys could take place during long term service. The strength and cracking have been observed to be dependent on the properties of the hydride precipitates (Allen et al., 2012). In order to achieve a deep understanding of the macro-behaviors of the Zr-based components, the microstructures including texture, dislocations and hydride precipitates, should be characterized in detail. Here, some recent experimental works related to X-ray or neutron diffraction line profile analysis are reviewed in what follows.

Zr-Excel alloy (Zr-3.5Sn-0.8Mo-0.8Nb) obtained via different heat treatment conditions has a typical microstructure with bimodal grain sizes. Both the initial and the martensitic grains in the solution treated Zr-Excel alloy are the hexagonal close-packed crystallographic structures. For studying the influence of the microstructure on the mechanical behavior of the heat-treated Zr-Excel alloy, Ahmmed et al. (2016) carried out neutron diffraction measurements to achieve dislocation densities and subgrain sizes corresponding to different components of such a bimodal microstructure. The results show that the microstructures of both components are obviously different. The initial phase has a lower dislocation density and a larger subgrain size, whereas the martensitic phase has a higher dislocation density and a smaller subgrain size (see Fig. 3.6). It's expected the Zr-Excel samples can be regarded as metal matrix composites, whose overall strength depends highly on the defect structures and the volume fraction of the individual components. In textured *hcp* metals or alloys there are different grain populations, corresponding to different texture components, in which plastic deformation can generate different dislocation densities with different prevailing Burgers vector types. In order to characterize the substructures by line profile analysis in different texture components the *hkl* diffraction peaks corresponding to the same texture component have to be identified and treated separately (Ribárik & Ungár, 2010;

Csiszár et al., 2012; Jóni et al., 2013; Ungár et al., 2015). The dislocation densities and the prevailing slip systems in a cold-rolled and additionally compressed Zircaloy-2 specimen were determined in the four texture components by neutron diffraction line profile analysis (Ungár et al., 2015). In order to have as many as possible diffraction peaks, each corresponding to only one of the four existing texture components, the specimen was rotated into seven different pre-calculated orientations. In the time-of-flight SMARTS neutron diffractometer (Bourke et al., 2002) two diffraction patterns were recorded for each sample orientation (Ungár et al., 2015). All fourteen diffraction patterns were used to select diffraction peaks corresponding solely to one of the four texture components. The peaks were used to construct texture-specific diffraction patterns for each texture component separately (Ungár et al., 2015). It was found that in the basal texture component the dislocation density and the fraction of the <a>-type slip-system were smaller than in the other texture components.

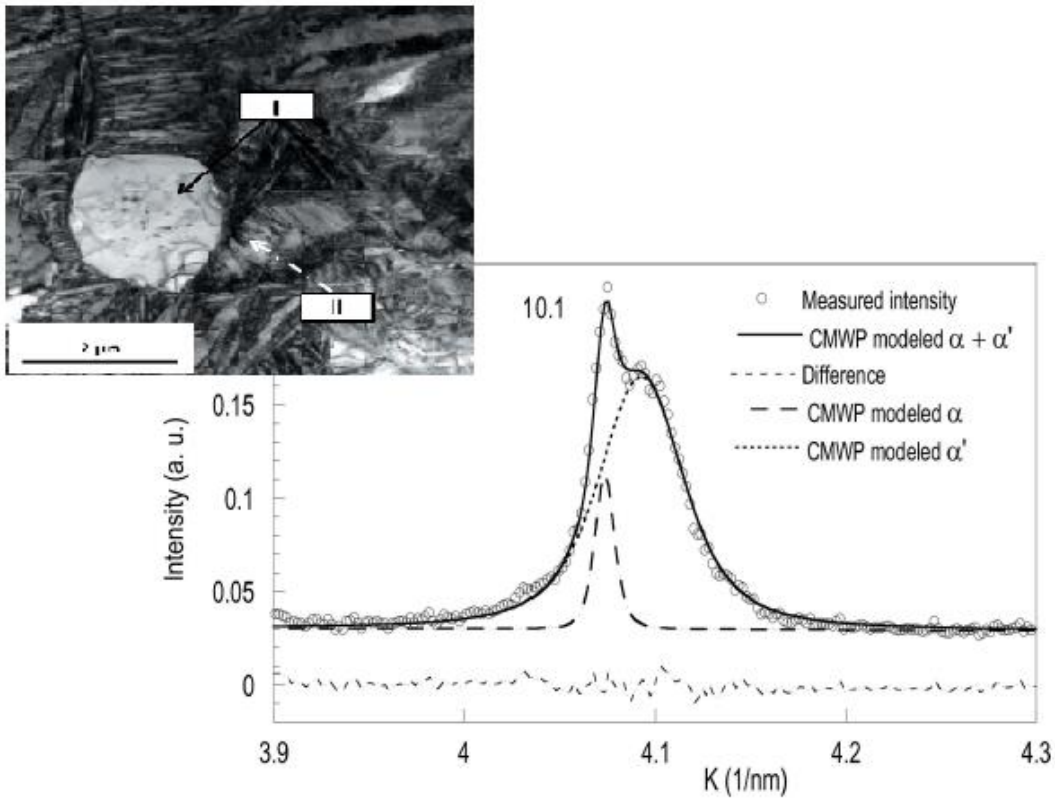

Fig. 3.6: The TEM and neutron diffraction measurements of a Zr-Excel alloy. 'I' and 'II' corresponds to primary and martensitic α phase, respectively. The neutron reflection shows a typical bimodal shape coming from primary and martensitic α phase. Modified from Figs. 6 and 10 in Ref. (Ahmmed et al., 2016).

The dislocation density evolution of <a>- and <c>-type loops of Zr-2 samples machined from fuel cladding and channel tubes were investigated by Seymour et al. (2017). The fluence range of the specimens is between 8.7×10^{25} n/m^2 and 14.7×10^{25} n/m^2 (E > 1 MeV). High-resolution synchrotron X-ray diffraction patterns of neutron-irradiated Zr-2 samples were collected and analyzed using the CMWP procedure. It is revealed by diffraction analysis that the total dislocation density increases as a function of fluence for the cladding materials. Further analysis shows the <a>-type loop density increases as well with fluence, while there's no clear trend for the evolution of <c>-type loop density. On the contrary, TEM measurements suggest the dislocation density of <a>-type loop reaches a saturation value with fluence, and <c>-type loop density increase with fluence. The authors suggested that more work is needed to clarify the discrepancy between the results of X-ray diffraction and TEM. Topping et al. (2018) observed the thermal stability of <a>-type dislocation loops in a proton-irradiated Zr-0.6Fe alloy by means of in-situ synchrotron X-ray diffraction. Synchrotron X-ray diffraction provides bulk information of microstructure in materials. Combined with in-situ annealing experiments, subtle variations of diffraction peaks can be detected, and the evolution of dislocation density of <a>-type loops can be evaluated as a function of annealing temperature, as shown in Fig. 3.7. The heating temperature was increased from 50 to 600 ^{o}C, with an incremental step of 50 ^{o}C and holding time of 60 min at each temperature. The diffraction measurements show there's no obvious change below the heating temperature of 300 ^{o}C, since then a dramatic recovery of <a>-type loops takes place between 300 and 450 ^{o}C. Inferred from the diffraction data the value of effective activation energy for the annealing process was 0.46 eV. These results are essential for the prediction of the annealing behavior of irradiated Zr-0.6Fe alloy, and offer an insight of the mechanisms of annihilation of dislocation loops induced by irradiation.

It's commonly observed that the strain-stress curves of neutron-irradiated Zr alloys exhibit irradiation hardening and ductility reduction (Himbeault et al., 1994; Onimus et al., 2004; Farrell et al., 2004; Onimus & Béchade, 2012). In order to gain a deeper understanding of the impacts of irradiated defects on the deformation behavior of Zr alloys, Balogh and co-workers (2012) investigated the dislocation structure of irradiated and subsequently deformed Zr-2.5Nb samples by neutron diffraction line profile analysis. The Zr-2.5Nb samples were machined directly from a seven years service pressure tube in a CANDU reactor. The diffraction measurements show neutron

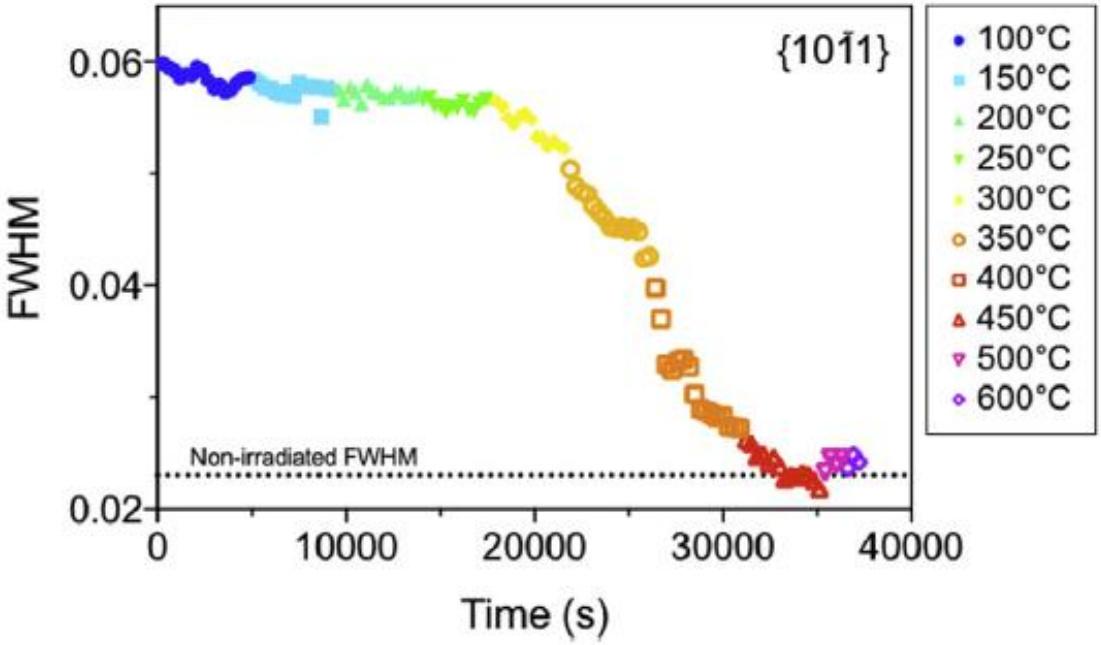

Fig. 3.7: FWHM of diffraction peak as a function of temperature measured by an in-situ synchrotron X-ray diffraction. Reproduced from Fig. 5 in Ref. (Topping et al., 2018).

irradiation result in a significant increasing of <a>-type dislocation loops in the irradiated sample, which is two times higher than the initial dislocation density in the sample (see Fig. 3.8). As barriers to dislocation glide, irradiation-produced dislocation loops together with point defects are the major factors for the increase in yield strength of the irradiated sample (Onimus et al., 2004). The irradiated sample was tensile deformed till failure. Further diffraction analysis of the irradiated sample after deformation demonstrates <c+a>-type dislocation density increases dramatically whereas <a>-type dislocation density keeps almost unchanged. It's found that the ratio of <a>- and <c+a>-type dislocations in the deformed irradiated-sample is nearly equal to that in the deformed unirradiated-sample. However, the densities and spatial fluctuations of dislocations in both cases are different. Localized deformation of dislocation channeling has already been observed in irradiated Zr alloys (Onimus et al., 2004; Farrell et al., 2004; Onimus & Béchade, 2012), which is expected to be responsible for the strain softening behavior of the deformed irradiated Zr-2.5Nb. In addition, diffraction line profile analysis revealed the evolution of the dislocation arrangement parameter *M* in the samples. The *M* parameter of the unirradiated Zr-2.5Nb is about 1, while the *M* of the irradiated sample increases to 3. The higher value of *M*

of the irradiated sample indicates that high energy dislocation structure could be produced and maintained under the circumstance of nuclear reactor. The plastic deformation results in the *M* value of the irradiated sample decreases from 3 to 1.6, which means more correlated and lower energy configuration of dislocation structure are formed. In contrast to the irradiated materials, the parameter *M* of the unirradiated samples keeps all along the level of 1 during the deformation.

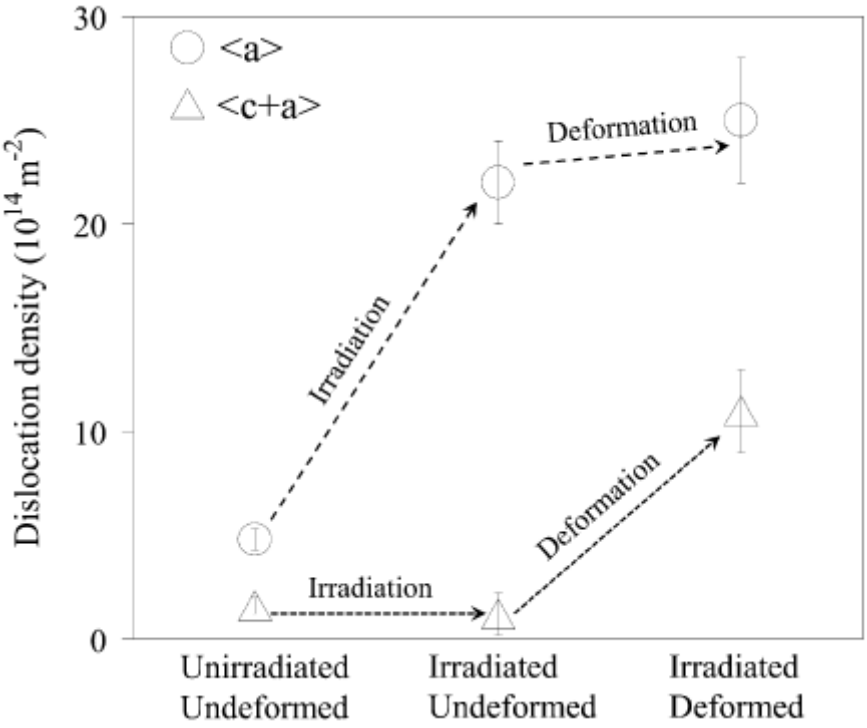

Fig. 3.8: Dislocation densities of Zr-2.5Nb sample after irradiation and deformation. Reproduced from Fig. 5 in Ref. (Balogh et al., 2012).

Hydride precipitates are formed via phase transformation of α-Zr with hydrogen absorption. Complex stresses are introduced in the hydride precipitates due to misfits between the precipitates and the zirconium matrix. One of the main factors leading to the failure of Zr-based components is hydride embrittlement. The information of microstructure prevailing in the hydrides is essential to understand the mechanical behavior of Zr alloy containing hydrides. By means of X-ray and neutron diffraction measurements, the texture of hydrides in Zr alloys have been revealed in detail (Santisteban et al., 2010; Alvarez et al., 2011, 2012). Besides that, Alvarez et al. (2016) characterized quantitatively the internal stresses and even the dislocation densities in FCC structure δ-hydride precipitates using the method of diffraction line profile

analysis. Two kinds of Zr alloys, Zr-2.5Nb and Zr-4, were investigated. Zr-2.5Nb specimens were from a CANDU pressure tube and then laboratory-charged to produce hydride blisters. Zr-4 specimens were machined from ten years service cooling channels of Atucha I nuclear power plant, where the H content and fluence of neutron irradiation are ~140 wt ppm and ~10^{26} n/m^2, respectively. Results show the broadening of diffraction peaks of the hydrides are originated mostly from the dislocations. The dislocation densities in the δ-hydrides increase with the H concentration. The range of the dislocation densities in the δ-hydrides is 5-20×10^{15} m^{-2}, which is far higher than in the α-Zr matrix, ~10^{14} m^{-2}, (see Fig. 3.9). In the case of the irradiated Zr-2.5Nb specimen, fast neutron irradiation produces a large amount of dislocation loops, and the dislocation density in the hydrides is therefore higher than in the unirradiated specimen. From the diffraction data, the *q* value of the contrast factor was determined, which indicates the elastic anisotropy of the δ-hydride is very high.

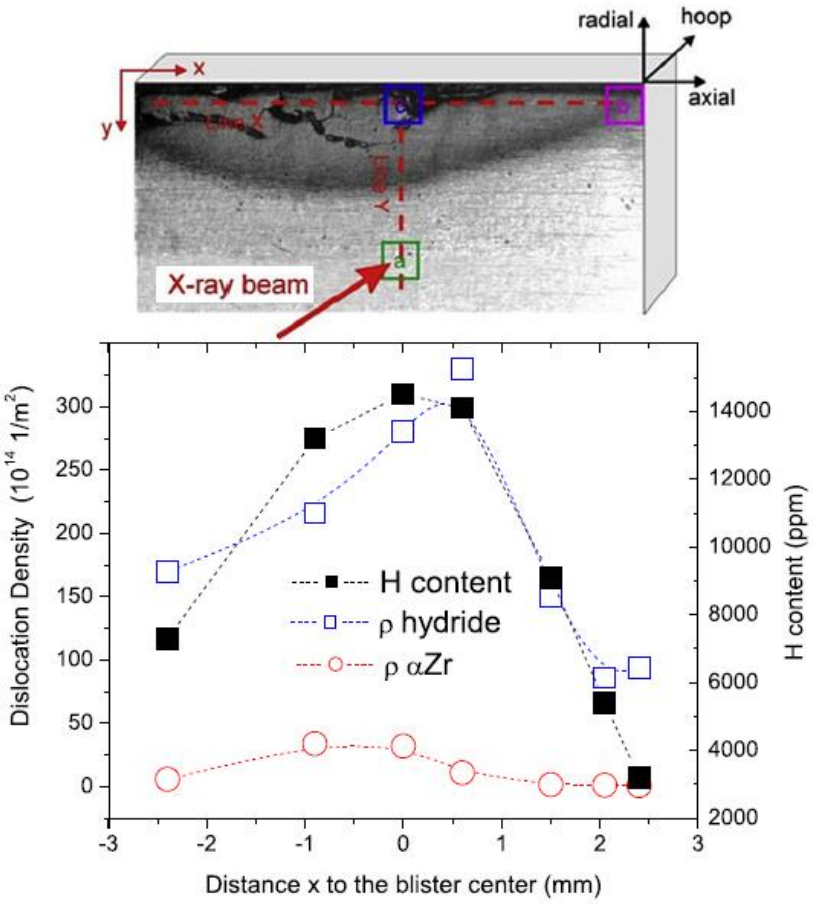

Fig. 3.9: Dislocation densities of δ-hydride and α-Zr and H content in the blister sample. Modified from Figs. 2 and 9 in Ref. (Alvarez et al., 2016).

3.5 Microstructure of vanadium alloys

As one advanced option of structural materials for the blanket of fusion reactor, vanadium alloys have several attractive properties, such as low induced activation, excellent mechanical properties, good compatibility with liquid lithium, high thermal conductivity and irradiation damage resistance (Muroga, 2012; Muroga et al., 2014). For the purpose of further improvement of vanadium alloys, different compositions of alloying elements have been attempted. The extensive survey indicated the addition of chromium is favorable for high temperature strength and corrosion resistance, while titanium is used for the resistance to irradiation swelling and hydrogen embrittlement. The total amount of Cr and Ti in vanadium alloy should not exceed 10% wt., otherwise the ductile-brittle transition temperature (DBTT) of alloy will increase dramatically (Matsui et al., 1996; Zinkle et al., 1998). Currently, much of the recent activities focused on V-(4-5)Cr-(4-5)Ti ternaries, which exhibit comprehensive performance in the anticipated environment of fusion reactor (Zinkle et al., 1998). The deformation behavior of V-5Cr-5Ti alloy during hot compression was modelled using constitutive equations (Li et al., 2015; Qu et al., 2016, 2018). It is recommended the optimal ranges of deformation temperature and strain rate are 1250-1400 ^{o}C and 0.001-0.02 s^{-1}, respectively (Qu et al., 2016, 2018). The impact and fracture properties were investigated for V-(4-5)Cr-(4-5)Ti alloys (Cai et al., 2010; Li et al., 2012; Tsisar et al., 2014, 2016; Li et al., 2017). The observations showed the fracture process is dominated by microvoid coalescence and dimple rupture (Cai et al., 2010; Li et al., 2012). The irradiation induced defects such as voids, dislocation loops and Ti-rich precipitates have been studied systematically (Gelles et al., 1998; Rice & Zinkle, 1998; Satou et al., 2000; Fukumoto et al., 2009, 2011; Zhu et al., 2015; Gao et al., 2016; Ding et al., 2017; Wang et al., 2018). Because excellent high temperature strength of the blanket materials benefits to the compact structure of blanket components, and therefore the enhancement of tritium breeding ratio, advanced vanadium alloys with high strength level are still being developed until now. In what follows, we'll review the works related to the correlation between novel processing techniques and microstructure of vanadium alloys (or pure vanadium in some cases).

The strengthening effects of thermo-mechanical treatments for V-4Cr-4Ti alloys were investigated by Chen and coworkers (Chen et al., 2006, 2008; Zheng et al., 2011; Fu et

al., 2013). In the Ref. (Fu et al., 2013), the authors demonstrated the fabrication process of a 30 kg large-scale ingot of V-4Cr-4Ti alloy (SWIP-30). To improve the high temperature strength of V-4Cr-4Ti alloy, several different combinations of cold working and aging were applied. Solution annealing, cold working and aging were denoted as SA, CW and A, respectively (Fu et al., 2013). The treatments, including SAA, SACWA, SAACW and SACWACWA, were carried out and compared each other, as shown in Fig. 3.10. Ti-rich precipitates could form during aging, and dislocations would be introduced by cold working. The grain size is ~30 μm and coarse Ti-CNO precipitates of ~200 nm exist upon any of the treatments. High densities of coarse precipitates are distributed along the grain boundaries in the alloy of SAACW, which is adverse for high temperature mechanical performance. For the alloys of SACWA and SACWACWA, much smaller dispersed precipitates are observed in the grain interior. It indicated that the cold working before the aging can suppress the coarsening of the precipitates (Zheng et al., 2011). According to the hardness, tensile and creep tests, the thermo-mechanical treatment SACWACWA has better comprehensive mechanical properties (Zheng et al., 2011; Fu et al., 2013). Based on the high plastic strains of vanadium alloys could be obtained at room temperature, the procedure of multiple multi-directional forge molding (MDFM) was developed (Tyumentsev et al., 2004, 2011, 2015; Ditenberg et al., 2012, 2013). During the cycles of the thermo-mechanical treatment, the specimen shape of V-4Cr-4Ti could keep invariable after a deformation corresponding to true logarithmic strains e ≈ 2-4 (Tyumentsev et al., 2011). It's supposed that high diffusion of point defects induced by such a plastic deformation would promote the dissolution of coarse Ti-CNO precipitates. Therefore, the larger amount of fine precipitates was formed in the matrix of the alloy. In addition, the high stored deformation energy can increase highly nucleation centers of new grains at the final step of annealing, which should benefit the formation of recrystallization grain. The results of MDFM showed that the sizes of grain and Ti-CNO precipitates are in the range of 3-5 μm and 10-20 nm, respectively (Tyumentsev et al., 2011). Fine-grained structure and uniformly distributed second phase particles in the specimens improved both the strength and the plasticity of the alloy significantly.

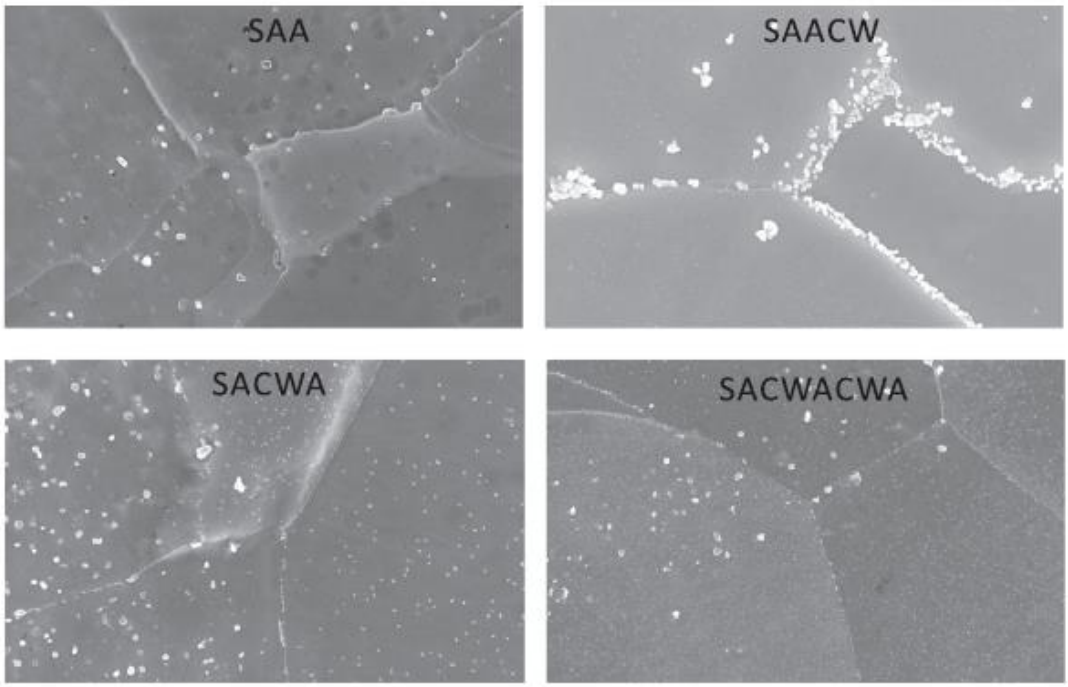

Fig. 3.10: Precipitates in V-4Cr-4Ti alloy after different thermo-mechanical treatments. Reproduced from Fig. 7 in Ref. (Fu et al., 2013).

For the purpose of achieving vanadium alloys with high-temperature strength, mechanical alloying was applied for a series of alloy systems (Kuwabara et al., 2006; Kurishita et al., 2006a, 2006b, 2007; Furuno et al., 2011; Sakamoto et al., 2011; Zheng et al., 2013, 2014a, 2014b). With respect to oxidation resistance, solid-solution hardening and swelling suppression, V-Cr-Ti alloy is considered as a more suitable matrix system. Zheng and coworkers manufactured V-4Cr-4Ti alloy with Y and TiC additions via MA followed by hot isostatic pressing (HIP) (Zheng et al., 2014b). The microstructure and the mechanical properties of V-4Cr-4Ti-1.5Y-0.3TiC alloy were investigated. The average grain size of the V-4Cr-4Ti-1.5Y-0.3TiC alloy with 40 h MA is ~0.3 μm, which is far smaller than that of NIFS-HEAT-2 with a standard heat treatment (STD) (~20 μm) (Muroga et al., 2002). The size and the density of nano-particles in the alloy are ~10 nm and ~$2\times10^{22}/m^3$, respectively. After one hour annealing at 1200°C for the as-HIPed alloy, the average grain size is ~0.4 μm, and the size and the density of nano-particles are ~5 nm and ~$3\times10^{22}/m^3$, respectively. The annealing resulted in coarsening of grains and formation of smaller nano-particles in the alloy. The hardness of the V–4Cr–4Ti–1.5Y–0.3TiC alloy increased continually with increasing MA time. The mechanical performance of vanadium alloy in MA, STD and

SACWA states is compared in Fig. 3.11. The tensile tests at 700ºC showed the strength and the plasticity of the mechanical alloyed specimen is better than that of NIFS-HEAT-2 with the standard heat treatment (STD) or the cold working and aging (SACWA) (Zheng et al., 2011, 2014b). It indicated that fine grain size and nano-particle dispersion are effective in the strengthening of the alloy via MA. The grain size with sub-micrometer is also favor for the elongation of the alloy. The nano-particles formed during MA are clarified as TiN and Y_2O_3, where Y_2O_3 has smaller size and larger density than TiN. The creep rate of the V-4Cr-4Ti-1.5Y-0.3TiC alloy is similar or lower than that of NIFS-HEAT-2 under the stresses below ~160 MPa. However, with increasing the stress the creep rate of the V-4Cr-4Ti-1.5Y-0.3TiC alloy is higher than that of NIFS-HEAT-2. It's known that grain boundary sliding of fine grains leads the promotion of creep deformation. But the results of creep test showed under lower stresses nano-particles are effective to improve the creep resistance of the MA alloy. Thermal stability of nano-particles is critical for the application of the MA alloy at high temperatures. Different additives of TiC, SiC and Ti_3SiC_2 together with yttrium were further compared (Zheng et al., 2014a). It was found that Ti_3SiC_2 is most stable and effective for the strengthening of MA alloy at high temperatures.

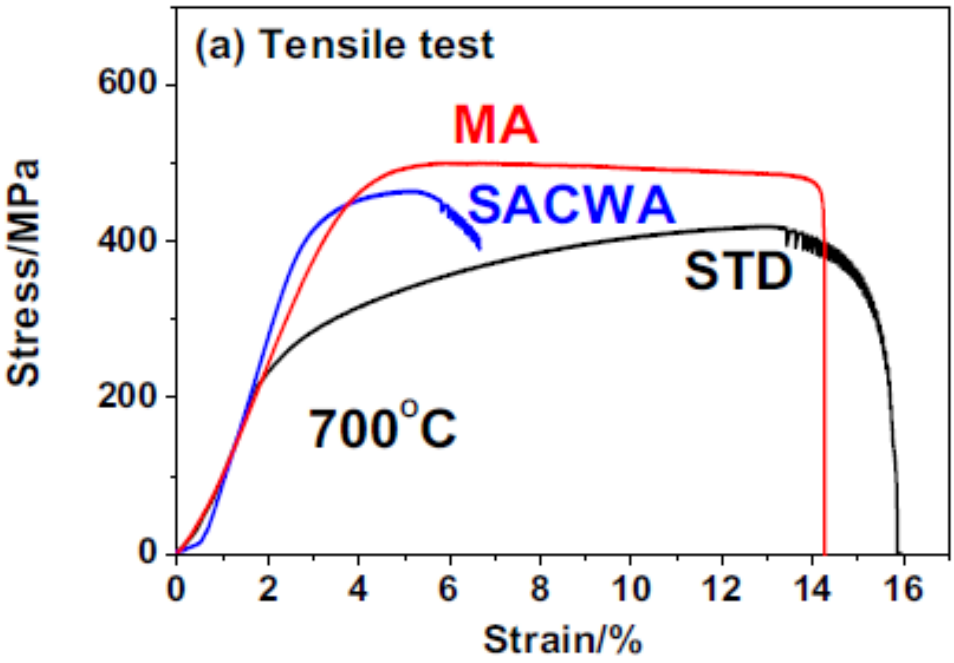

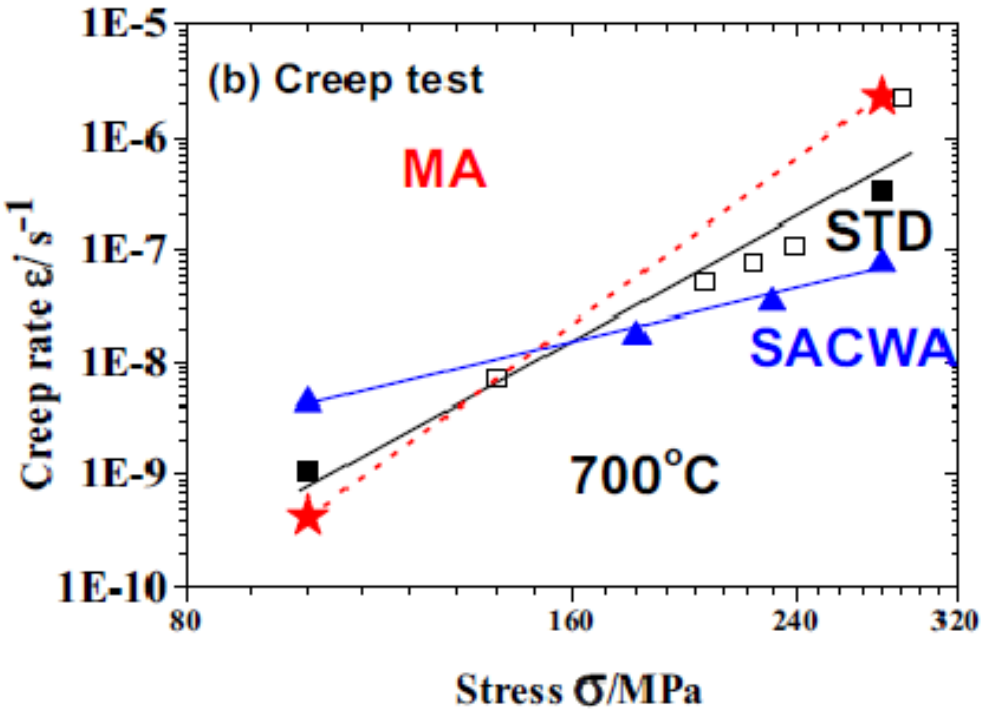

Fig. 3.11: Comparison of mechanical performance of mechanical alloyed vanadium alloy via mechanical alloying and in STD and SACWA states. Reproduced from Fig. 5 in Ref. (Zheng et al., 2014b).

Equal channel angular pressing is one of severe plastic deformation (SPD) techniques, which can refine grains in metals or alloys by imposing high strains. Hwang and coworkers attempted to process pure vanadium applying the method of ECAP (Jiang et al., 2008; Chun et al., 2009, 2010). The microstructure and the tensile properties of the samples were investigated. The initial grain size of the sample is ~100 μm. After eight passes of ECAP at 350 ºC, the grain size was reduced extensively to 0.2 μm (Jiang et al., 2008). The fine grain size and the high dislocation density induced by ECAP therefore enhanced the strength of the sample. The ultimate tensile strength (UTS) at room temperature increased from 247 MPa in the original state to 751 MPa in the final state. For the further refinement of grain size of vanadium, they combined ECAP and cryogenic rolling (Chun et al., 2009, 2010). Before the rolling, the plate of the sample was soaked into liquid nitrogen for 3 min. Such a low temperature is prone to suppress dynamic recovery of dislocations during the cryogenic rolling. The additional 60% cryorolling to ECAP processed vanadium resulted in the refinement of the grain size to 0.14 μm, and concurrently an enhancement of the UTS to 918 MPa. The significant

increase of the strength of the samples was accompanied by a loss of the plasticity. The total elongation of the as-ECA pressed sample is 14%, it fell to 8.5% after the cryorolling. Both the values are far lower than that of the original specimen, 57%. To recover the plasticity of the samples subjected to large strains, the annealing heattreatment was applied subsequently (Jiang et al., 2008; Chun et al., 2009, 2010). During the annealing, dynamic recovery and continuous recrystallization are two important mechanisms dominating the microstructure evolution of the samples. After the annealing at 850 °C for 30 s, the complete recrystallization of the sample was realized, and the grain size increased to ~1 μm. Correspondingly, the UTS and the total elongation are ~400 MPa and 30%, respectively. The plasticity and strength are comparable to the level of a V-4Cr-4Ti alloy (Jiang et al., 2008). Tensile stress-strain curves of ECA-pressed vanadium are shown in Fig. 3.12. A balance between the strength and the plasticity could be obtained via the annealing heattreatment after the ECAP and the cryogenic rolling.

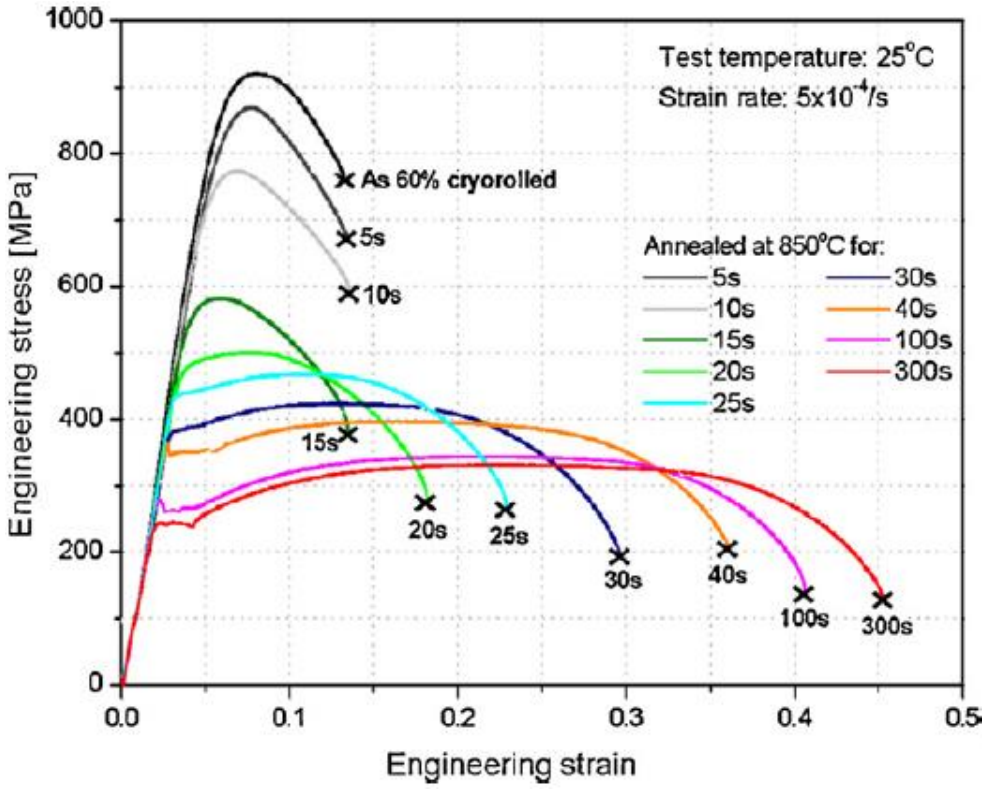

Fig. 3.12: Tensile stress-strain curves of ECA-pressed with additionally cryorolled and annealed vanadium. Reproduced from Fig. 4 in Ref. (Chun et al., 2009).

Microstructure and mechanical properties of pure vanadium (Lee et al., 2010; Hohenwarter & Wurster, 2016; Huang et al., 2016) and vanadium alloys (Ditenberg et al., 2011, 2012; Smirnov et al., 2016; Grinyaev et al., 2016, 2017; Ditenberg & Tyumentsev, 2015, 2018) processed by high pressure torsion were investigated. In the work of Huang et al. (2016), fine grains and enhanced strength of pure vanadium were achieved using the procedure of HPT under 6 GPa pressure at ambient temperature. After 10 turns, the grain size was refined from the initial value of ~27 μm to the final value of ~0.4 μm, and the fraction of high-angle grain boundaries (misorientation difference > 15°) is about 90%. The Vickers microhardness HV of the original sample is ~85. With increasing strains, the hardness reached to a saturation level with the HV value about 240. The samples processed through 10 turns were then subjected to an annealing process of 15 minutes. Fig. 3.13 shows the variation of microhardness and grain size of the post-HPT samples as a function of annealing temperature. The grain size keeps nearly constant till the annealing temperature 873 K. When increasing the temperature to 973 K, the recrystallization occurred obviously and the grain size increased to ~0.6 μm. The grain size eventually grew to ~2.8 μm at the annealing temperature 1073 K. Correspondingly, the microhardness value dropped at 873 K, which could be primarily related to the recovery of dislocations. At higher annealing temperatures, due to the recrystallization the microhardness value continued to decrease and reached a plateau. Tensile tests at room temperature show the UTS and the elongation of the sample of 10 turns are ~920 MPa and ~29%. After the annealing at 873 K, the UTS of the sample decreased to ~750 MPa, while the elongation increased to ~39%. Grinyaev and coworkers studied the microstructures and thermal stability of V-Cr-Zr-W alloy deformed by HPT under 7 GPa at room temperature (Grinyaev et al., 2016, 2017). TEM observations revealed two-level nanostructured states were formed during the process of HPT. Nanocrystallites of 5-20 nm with a dipole or multipole character were prevailing in the submicrocrystallites. The dimension of submicro-crystallites is anisotropic with 70-700 nm in the direction parallel to the anvil plane and 50-200 nm in the torsion axis direction. Subsequently, one hour annealing of the HPT deformed V-Cr-Zr-W alloy at the temperatures from 973 to 1473 K were carried out. The recovery process and primary recrystallization take place at about 1073 and 1173 K, respectively. The HPT processed V-Cr-Zr-W samples has higher thermal stability due to the formation of large fraction of 3-20 nm Zr(CNO) nanoparticles.

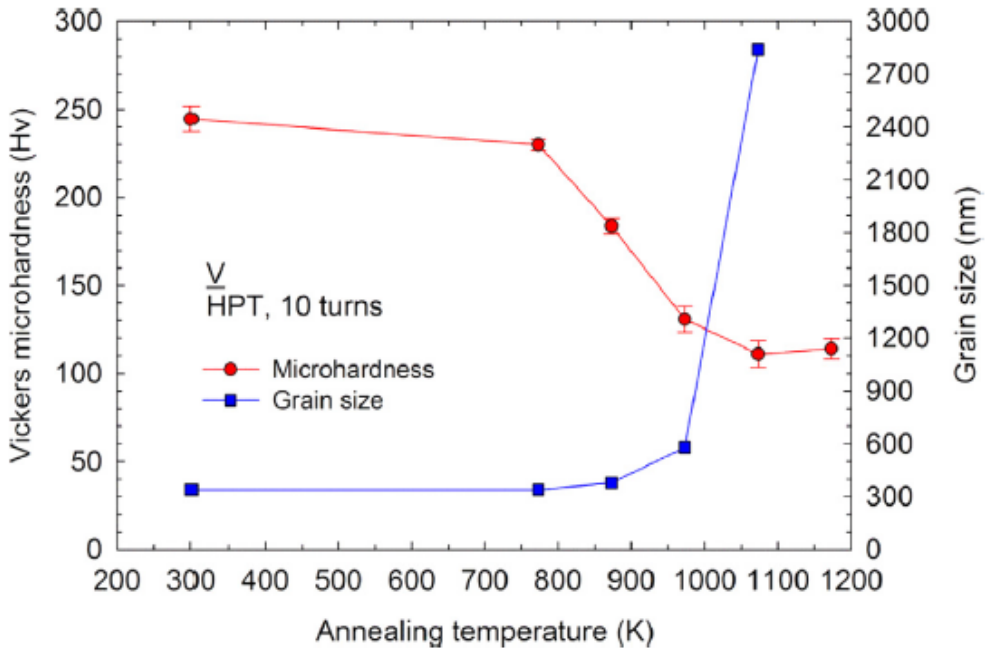

Fig. 3.13: Microhardness and grain size of vanadium as a function of annealing temperature. Reproduced from Fig. 5 in Ref. (Huang et al., 2016).

Chapter 4

Dislocation structure in textured zirconium tensile-deformed along rolling and transverse directions

In the present work high-resolution quasi-parallel-beam X-ray diffraction experiments are carried out to obtain high quality diffraction patterns for line profile analysis. The prevalent slip-system types and the average dislocation densities of each texture component in the deformed specimens are determined by using the convolutional multiple whole profile procedure. The mechanical properties of the specimens deformed along the RD and the TD directions are discussed in terms of deformation modes and dislocation densities.

4.1 Experimental

4.1.1 Samples

The high-purity Zr (99.99% in wt%) material investigated here was obtained from Northwest Institute for Non-ferrous Metal Research of China, with an equiaxed grain structure of average grain size of ~10 μm and the dislocation density less than $10^{12}/m^2$. Tensile specimens of dog-bone shape were machined from the cold rolled Zr plate with the RD and the TD directions parallel to the tensile direction, respectively. (Since the normal direction (ND) of the Zr plate was in the thickness direction, no ND oriented specimens could be prepared for a tensile experiment.) The gauge length, the width and

the thickness of the specimens are about 10, 3 and 1 mm, respectively. The specimens were tensile-deformed at room temperature at a constant strain rate of ~10^{-4} s^{-1} in an INSTRON-5967 materials testing machine. True-stress *vs*. true-strain curves of the RD and TD specimens, strained to the largest attainable strain values before necking set in, are shown in Fig. 4.1. Three samples were prepared from each of the RD and TD specimens: with 2.5%, 12%, and 17% true strains for the RD and 2.5%, 9%, and 13% true strains for the TD specimens, respectively. For the purpose of X-ray diffraction measurements the specimens were cut from the central part of the tensile-deformed samples perpendicular to the loading direction. Specimen surfaces were prepared by mechanical grinding with 1200 grit SiC, and then electropolished with an electrolyte of 70% alcohol, 20% perchloric acid and 10% glycerol.

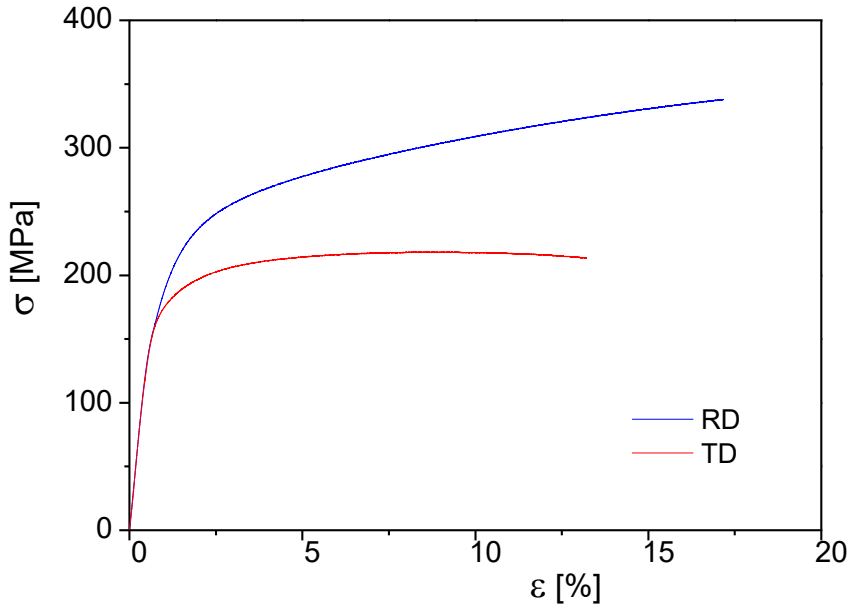

Fig. 4.1: True-stress true-strain curves of the Zr specimens tensile deformed along RD and TD.

4.1.2 Texture measurements

Polycrystalline materials are composed of many grains or crystallites with various orientations. In most cases, the grains or crystallites are arranged spatially along some specific directions. Such kind of orientation distribution is defined as preferred

orientation or texture. Due to the anisotropy of the properties of each crystallite, polycrystalline materials with specific texture naturally exhibit anisotropy at different level. In the processes such as deformation, recrystallization and phase transformation, the texture could be changed or the new texture will be formed in polycrystalline materials. Correspondingly, the properties of a material can be varied depending on the processing conditions. In order to investigate the relation between the texture evolution and the manufacture conditions, and even optimize the manufacture process, the determination of the texture of material is extremely important.

X-ray diffraction is a widely used technique to measure the texture of polycrystalline materials. The reflection intensity of specific crystallographic planes is proportional to the volume fraction of crystallites meeting the diffraction condition. Hence, the texture information obtained by X-ray diffraction experiments is the orientation distribution of crystallites averaged over the whole sampled volume. It is commonly referred as macrotexture.

Macrotexture measurements of the specimens were performed with a Bruker D8 Discover X-ray diffractometer operated at the air cooled microfocus copper sealed tube (IμS^{TM}) at 50 kV and 1000 μA. The diffraction data were collected using a two-dimensional photon-counting, Xe-based VÅNTEC-500 detector of 140 mm diameter, 4×10^6 pixels and 68 μm linear resolution. The size of the incident beam on the specimen was 0.5 mm in diameter. In order to improve the statistics of texture data the specimens were oscillated during the measurements by about ±2.5 mm in front of the X-ray beam. Six incomplete pole figures of $\{10\bar{1}0\}$, $\{0002\}$, $\{10\bar{1}1\}$, $\{10\bar{1}2\}$, $\{11\bar{2}0\}$ and $\{10\bar{1}3\}$ were measured in the 0° to 70° polar and 0° to 360° azimuth angle ranges, respectively. The measured pole figures were used to calculate the orientation distribution function (ODF) and the complete pole figures using the MTEX toolbox (Hielscher & Schaeben, 2008). The complete pole figures in the undeformed, the 17% strained RD and the 13% strained TD specimens are shown in Fig. 4.2.

4.1.3 X-ray diffraction experiments

X-ray diffraction measurements, for the purpose of line profile analysis, were carried out using a dedicated high-resolution double crystal diffractometer (Ungár et al., 1998).

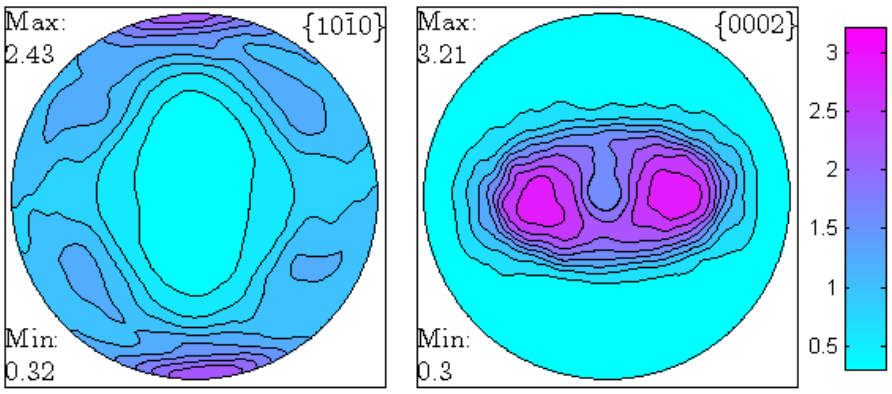

(a) Original sample

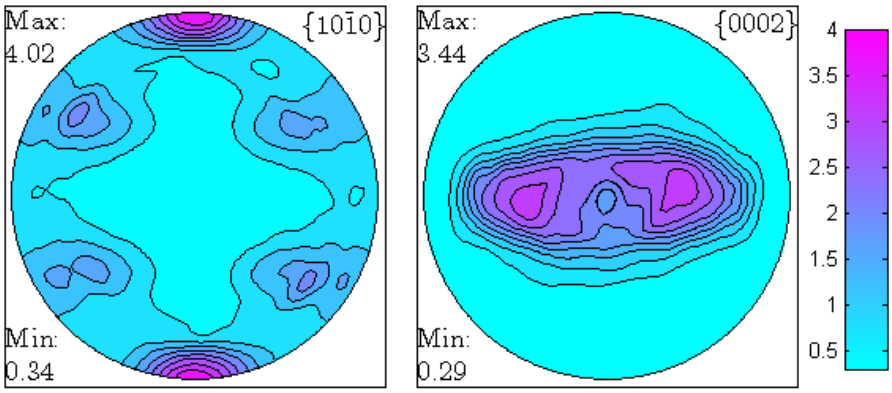

(b) RD sample at 17% strain

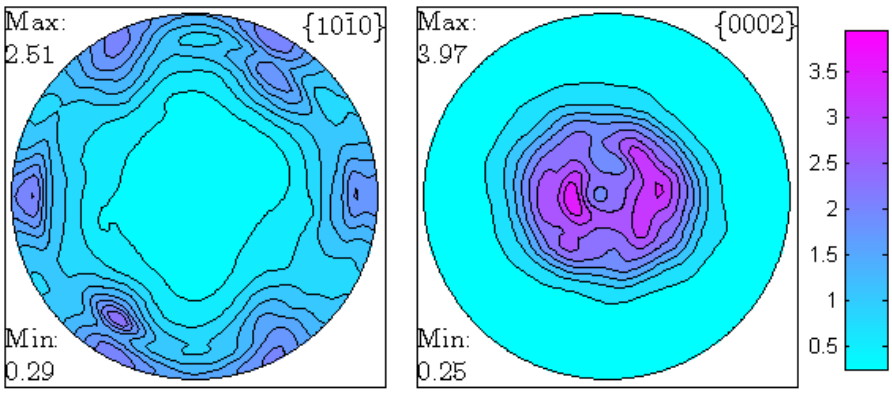

(c) TD sample at 13% strain

Fig. 4.2: The complete pole figures for the Zr specimens, (a) undeformed and (b) tensile-deformed along RD at 17% strain and (c) along TD at 13% strain, respectively.

The fine focus of the Rigaku, RAMultiMax9 rotating copper anode was operated at 40 kV and 100 mA. A combination of a plane Ge (220) primary monochromator and a 200 μm wide slit between the source and the monochromator was used to eliminate the Kα_2 component of the Cu Kα doublet. The size of the incident beam on the sample surface was about 0.2 mm×1.5 mm. The scattered radiation was registered by curve imaging plates (IPs) with a linear spatial resolution 50 μm. The distance between the specimen and the IPs was 200 mm, where the 2θ = 20° to 150° scattering angular range was covered. The diffraction patterns of the Zr specimens were collected at different sample orientations following a procedure described in the next section. Two typical IP readouts of the diffraction patterns for the RD specimen deformed at 17% strain are shown in Fig. 4.3. The two patterns were measured at the same incident angle of ω = 25° but on two different surfaces of the same specimen. The pattern in Fig. 4.3a corresponds to diffraction on the ND-TD plane, whereas Fig. 4.3b to RD-TD plane of the RD specimen.

The false colors in the figure clearly indicate the very different, though complementary, peak intensities due to the split-basal texture of the specimen. Diffraction patterns were obtained by integrating the intensity distributions along the Debye-Scherrer arcs in the central regions of the IPs. Two typical diffraction patterns corresponding to the IP readouts in Figs. 4.3a and 4.3b are shown in Fig. 4.4.

In textured materials, the measured diffraction peaks may consist of contributions from grains belonging to different texture components. Only specific peaks consist of diffraction from grains belonging to one specific texture component. Reflections of this type, belonging to a specific texture component, were selected from diffraction patterns collected at various sample orientations. We varied the incident angle of the X-ray beam on the sample surface and the orientation of the samples. The peaks corresponding mainly to one specific texture component were selected from the patterns measured at different sample orientations and merged into a single pattern in a somewhat similar manner as in Ref. (Ungár et al., 2015).

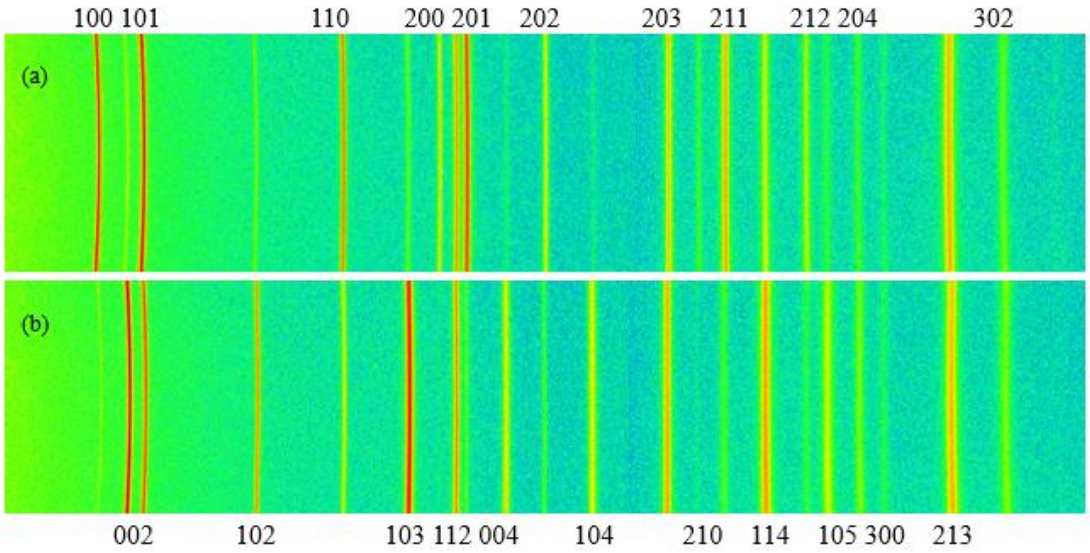

Fig. 4.3: IP readouts of the diffraction patterns for the Zr specimen deformed along RD at 17% strain measured on (a) the one sample surface parallel to the ND-TD plane and (b) the other was the RD-TD plane at the same incident angle 25°.

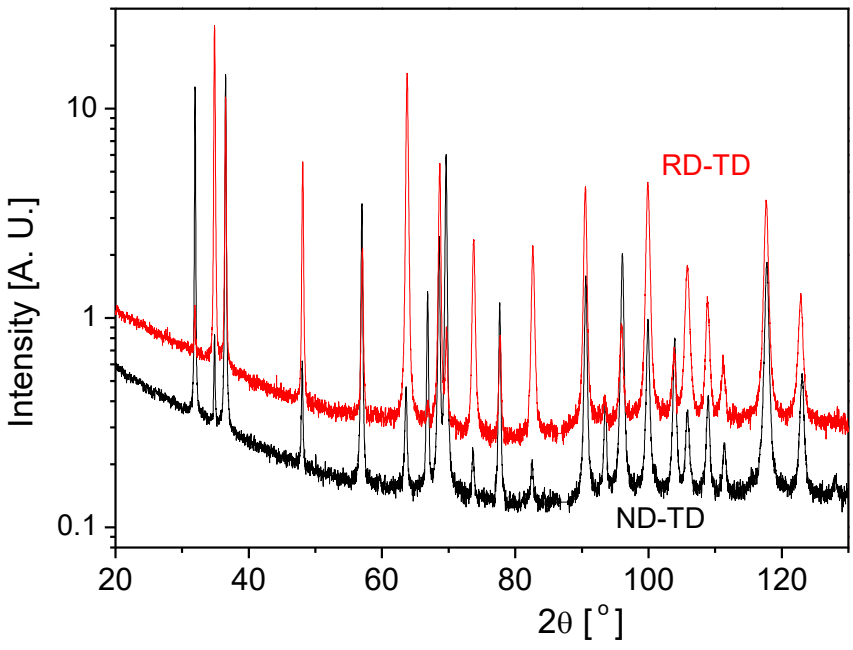

Fig. 4.4: Two typical diffraction patterns of the Zr specimen deformed along RD at 17% strain measured on the sample surfaces parallel to the ND-TD plane and the RD-TD plane at the same incident angle 25°.

4.1.4 Identifying diffraction peaks corresponding to the same texture component

In this section, we describe the procedure to identify diffraction peaks corresponding to different texture components. Fig. 4.5 shows the laboratory coordinate system, *x, y, z*, where *x* is parallel to the incoming beam, *y* is normal to the sample surface and *z* is normal to *x* and *y*. Since the diffraction geometry is of parallel-beam type, the incident angle ω, i.e. the angle between the incoming beam and the sample surface, is kept fixed with a stationary specimen. In order to increase the number of reflections corresponding to specific texture components, diffraction patterns can either be collected at different ω values (Jóni et al., 2013), or at several different specimen orientations (Ungár et al., 2015).

The schematic drawing of the rectangular plate like specimens are shown in Fig. 4.5. In Figs. 4.5b, 4.5c and 4.5d the TD, RD and ND directions are set parallel to the *y* axis of the laboratory coordinate system, respectively. When rotating the specimen around the *y* axis, any value of ω can be obtained. These rotations can be given by two rotation matrices in the *z*-*y*-*z* and *z*-*x*-*z* conventions. Denote the two rotations as $R_{\varphi_1,\varphi,\varphi_2} = R_z(\varphi_1)R_y(\varphi)R_z(\varphi_2)$ and $R_{\varphi_1,\varphi,\varphi_2} = R_z(\varphi_1)R_x(\varphi)R_z(\varphi_2)$, respectively, where *x*, *y*, *z* is the laboratory coordinate system and φ_1, φ, φ_2 are the Eulerian angles of rotation. We assume that in the initial position the TD, RD and ND directions of the specimens are set parallel to the *x*, *y* and *z* axis of the laboratory coordinate system, respectively. If the RD, TD, or ND directions of the specimen are parallel to the *y* axis, respectively, the rotation around the *y* axis from the initial position can be represented by the rotation matrix $R_{\varphi_1,\varphi,\varphi_2} = R_z(0)R_y(\varphi)R_z(0)$ in the *z*-*y*-*z* convention, and by $R_{\varphi_1,\varphi,\varphi_2} = R_z(90)R_x(\varphi)R_z(0)$ and $R_{\varphi_1,\varphi,\varphi_2} = R_z(0)R_x(90)R_z(\varphi_2)$ in the *z*-*x*-*z* convention (Engler & Randle, 2010; Ungár et al., 2015). Fig. 4.5 shows the rotations of the specimens around either the RD, or the TD, or the ND directions, schematically.

Setting one of the basal lattice constant, $\boldsymbol{a_1}$, parallel to *x* and the prismatic lattice parameter, $\boldsymbol{c}$ parallel to z, the unit vectors, $\mathbf{e}_{hk.l}$, normal to the (*hk.l*) planes in the laboratory coordinate system will be:

<table>
<tr><td> 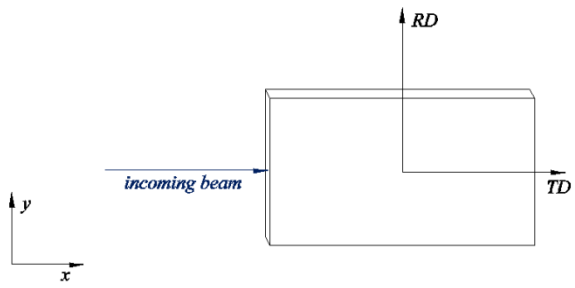
</td><td> 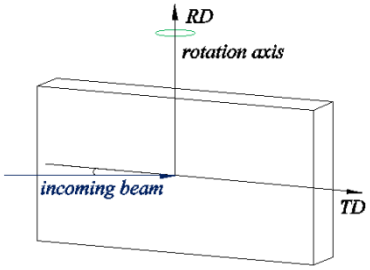
</td></tr>
<tr><td>(a) Definition of the specimen coordinate system</td><td>(b) Rotation of specimen in z-y-z:
$R_{\varphi_1,\varphi,\varphi_2} = R_z(0)R_y(\varphi)R_z(0)$,
φ: (-90°, 90°)</td></tr>
<tr><td> 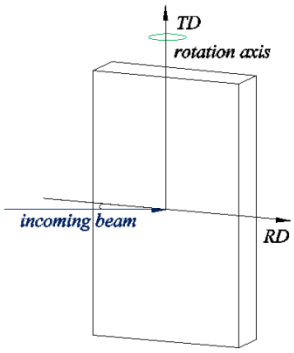
</td><td> 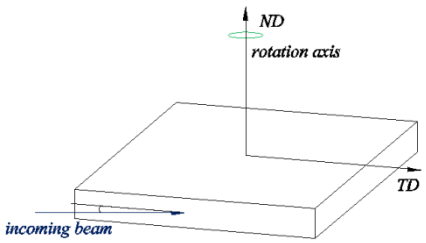
</td></tr>
<tr><td>(c) Rotation of specimen in z-x-z:
$R_{\varphi_1,\varphi,\varphi_2} = R_z(90)R_x(\varphi)R_z(0)$,
φ: (-90°, 90°)</td><td>(d) Rotation of specimen in z-x-z:
$R_{\varphi_1,\varphi,\varphi_2} = R_z(0)R_x(90)R_z(\varphi_2)$,
φ_2: (-90°, 90°)</td></tr>
</table>

Fig. 4.5: The initial position of the Zr specimen in the laboratory coordinated system is shown schematically in (a), where the *x* axis is parallel to the incoming beam, the *y* axis is normal to the surface of the sample stage, and *z* axis is normal to *x* and *y*. The rotations of the Zr specimens around three axes: (b) the rolling axis, (c) the transverse axis and (d) the normal axis from the initial position are described mathematically.

$$\mathbf{e}_{hk.l} = d_{hk.l}\left(\frac{h}{a}, \frac{2k+h}{\sqrt{3}a}, \frac{l}{c}\right) \ , \tag{4.1}$$

where $d_{hk.l}$ is the spacing of the ($hk.l$) planes, and a and c are the lattice parameters. Rotating the specimen by the Eulerian angles φ_1, φ, φ_2, the normal vectors, $\mathbf{e}'_{hk.l}$, of the ($hk.l$) planes of the different texture components in the specimen will be:

$$\mathbf{e}'_{hk.l} = R_{\varphi_1,\varphi,\varphi_2} R_{\alpha,\beta,\gamma} \mathbf{e}_{hk.l} \ , \tag{4.2}$$

where $R_{\alpha,\beta,\gamma}$ is the rotation matrix in the z-x-z convention and α, β and γ are the Eulerian angles of a texture component given by the X-ray macro-texture measurements.

Denote the direction of the diffraction vector in the laboratory coordinate system as $\mathbf{s}_{hk.l}$:

$$\mathbf{s}_{hk.l} = (-sin\theta_B, 0, cos\theta_B) \ . \tag{4.3}$$

The probability density, $f_{hk.l}(\chi)$, of the diffracted volume of the ($hk.l$) planes in the $\mathbf{s}_{hk.l}$ direction can be written as be:

$$f_{hk.l}(\chi) = \frac{\exp(-4ln2 \cdot \chi^2/H^2)}{2\pi \int_0^{\pi} \exp(-4ln2 \cdot \chi^2/H^2) sin\chi d\chi} \ , \tag{4.4}$$

where it is assumed that $\mathbf{e}'_{hk.l}$ follows a Gaussian distribution, χ is the angle between $\mathbf{e}'_{hk.l}$ and $\mathbf{s}_{hk.l}$, and H is the FWHM of the Gaussian distribution of $\mathbf{e}'_{hk.l}$. The intensity $I_{tot}(\mathbf{s}_{hk.l})$ of the $hk.l$ reflection collected by the IPs (or any two dimensional detector) can be given as:

$$I_{tot}(\mathbf{s}_{hk.l}) = K \sum_i \sum_{\{hk.l\}} V_i f_{i,hk.l}(\chi_i) + K V_r m_{hk.l}/4\pi \ , \tag{4.5}$$

where the coefficient K includes the Lorentz-polarization factor, the absorption correction and the square of structure factor, $m_{hk.l}$ is the multiplicity of the $hk.l$ reflection (Warren, 1969) and V_i and V_r are the volumes of the major and random texture components, respectively. The first term on the right side of Eq. (4.5) sums over all equivalent ($hk.l$) planes and texture components and the second term represents the

contribution from the grains in the random texture component. The intensity ratio of the major texture component to the total intensity is:

$$\frac{I_{tex}}{I_{tot}} = \frac{\sum_i \sum_{\{hk.l\}} V_i f_{i,hk.l}(\chi_i)}{\sum_i \sum_{\{hk.l\}} V_i f_{i,hk.l}(\chi_i) + V_r m_{hk.l}/4\pi} \quad . \tag{4.6}$$

The values of the ratios, I_{tex}/I_{tot}, can be investigated as a function of rotation angles φ or φ_2 for the three rotation modes, discussed before. This will show if it is possible to select suitable combinations of rotation angles for obtaining diffraction patterns with reflections pertaining to selected texture components.

4.1.5 Evaluation of the X-ray diffraction patterns

The texture specific diffraction patterns were evaluated using the CMWP procedure to obtain quantitative information of substructures in texture components. The crystallite or subgrain size is determined by assuming a log-normal size distribution with the median and the variance, m and σ_{LN}. The area average crystallite size is obtained as $d_{area} = m \times \exp(2.5 \times \sigma^2_{LN})$ (Hinds, 1982; Ungár et al., 2001). The strain broadening is given in terms of the mean square strain (Warren, 1959; Wilkens, 1970a):

$$\langle \varepsilon^2_{g,L} \rangle \cong \frac{\rho \overline{Cb^2}}{4\pi} f(\eta) \quad , \tag{4.7}$$

where g is the absolute value of the diffraction vector and L is the Fourier variable, ρ, C and b are the density, the contrast and the Burgers vector of dislocations and $f(\eta)$ is the Wilkens function (Wilkens, 1970a). In the function $f(\eta)$, the variable $\eta = L/R_e$, where R_e is the effective outer cut-off radius of dislocations. The correlation between R_e and the average dislocation distance, $1/\sqrt{\rho}$, is expressed in the dimensionless dislocation arrangement parameter, $M = R_e\sqrt{\rho}$ (Wilkens, 1970b). M characterizes the dipole character of dislocations. For dislocation arrangements with strong or weak dipole character M will be smaller or larger than unity. We shall use the M values in the discussion of the α parameter in Taylor's equation in paragraph 4.2.3. In the case of hexagonal crystals, the averaging of Cb^2 is extended to 11 slip-plane families, and for a particular ith slip-plane family the average contrast factors can be given as (Dragomir & Ungár, 2002):

$$\bar{C}_{hk.l}^{(i)} = \bar{C}_{hk.0}^{(i)}\left[1 + q_1^{(i)}x + q_2^{(i)}x^2\right] , \tag{4.8}$$

where $\bar{C}_{hk.0}^{(i)}$ is the average contrast factor of the *hk.0* reflections, $q_1^{(i)}$ and $q_2^{(i)}$ are parameters depending on the *i*th slip-plane family and the elastic properties of the material, and $x = \left(\frac{2}{3}\right)\left(\frac{l}{ga}\right)^2$. The $q_1^{(i)}$ and $q_2^{(i)}$ parameters and the values of $\bar{C}_{hk,0}^{(i)}$ were evaluated numerically and can be found in Ref. (Dragomir & Ungár, 2002). The CMWP procedure provides the $q_1^{(m)}$ and $q_2^{(m)}$ parameter values, where *m* indicates that these are the measured values. Matching of the measured, $q_{1,2}^{(m)}$ and theoretically calculated, $q_{1,2}^{(i)}$ values can provide the relative fractions of the <*a*>, <*c*+*a*> and <*c*> type families of dislocation (Máthis et al., 2004; Ungár et al., 2007).

4.2 Results and discussion

4.2.1 Mechanical response and texture evolution

The true-stress true-strain curves of the RD and TD specimens are shown in Fig. 4.1. The yield stress values, σ_y, were determined as the offset yield point at 0.1% plastic strain, i.e. $\sigma_y = R_{p0.1}$. It is found that, within experimental error, they are almost identical for the RD and TD samples: $\sigma_y(RD) \cong \sigma_y(TD) \cong 150$ (±15) MPa. At the same time, the work hardening in the two different directions is very different, as indicated by the figure. After yielding, the stress increases more gradually for the RD samples than the TD samples. The RD samples keep high strain-hardening rate and extended plasticity, whereas, the TD samples show almost no work hardening and somewhat smaller ductility. A slight necking was observed in the TD sample at the strain of about 13%.

The texture of the original Zr specimen is of typical split-basal rolling texture. The basal poles are inclined about ±30° from ND toward TD, and the $[01\bar{1}0]$ direction is parallel to RD. The texture of the RD specimens was nearly unchanged during tensile-deformation. In the TD samples, significant texture change was observed with increasing strain. At strains higher than 9% the prismatic poles were inclined towards the TD and the basal poles were reoriented slightly from the TD to the ND. Fig. 4.2 shows the prismatic and basal pole figures for the original specimen, the RD specimen

at 17% strain, and the TD specimen at 13% strain, respectively. The following Eulerian angles, FWHMs and volume fractions of the different texture component were obtained from the ODF data. In the original specimen and in the RD and TD specimens deformed up to 2.5% strain the Eulerian angles of the major texture components are (90°, 30°, 30°) and (270°, 30°, 30°), the FWHM is 50° and the volume fraction of the major texture component is 0.7, with the rest corresponding to random orientation grains. At larger strains of 9% and 13% the major texture component in the TD specimens split into four equivalent parts with Eulerian angles (60°, 16°, 30°), (120°, 16°, 30°), (240°, 16°, 30°) and (300°, 16°, 30°), respectively. The volume fraction of the major texture component is still 0.7 with equally distributed FWHM of 25°. The rest of the grains are randomly oriented. As mentioned before, the texture of the RD specimens does not change even at larger strains.

4.2.2 Dislocation densities and slip-system activities

The three rotation modes for diffraction measurements are illustrated in Fig. 4.5. Two different schemes were selected and applied for the Zr specimens. For the undeformed, the three deformed RD and the 2.5% strained TD specimens the TD was taken as the rotation axis, as shown in Fig. 4.5c. The incident angle, ω, was chosen ω = 25° on the sample surface either parallel to the ND-TD (see Fig. 4.5d) or to the RD-TD plane (see Fig 4.5c), respectively. For the TD specimens strained to 9% and 13% the rotation axis was the RD (see Fig. 4.5b), and the incident angle was selected ω = 25° on the sample surfaces either parallel to the ND-RD or the TD-RD planes (see Fig. 4.5b), respectively. The rotation around the ND axis (Fig. 4.5d) was not used, since this would have given only a few lower order reflections for the major texture component.

The I_{tex}/I_{tot} ratios for the undeformed and 9% strained TD specimens collected on the two different sample surfaces are shown in Figs. 4.6a and b and Figs. 4.7a and b, respectively. Two bounds of intensity ratios were selected, with an upper bound of 0.7 for intensity ratios selecting those peaks in which the volume fraction of the major texture component is larger than 70%, and a lower bound of 0.4, where the majority of scattered intensity corresponds to randomly oriented grains. In the next step reflections above the upper or below the lower bounds were selected to construct patterns, i.e. TSDPs, for the major or the random texture components, respectively. Figs. 4.6c and

4.7c show the selected reflections for the undeformed and 9% strained TD specimens, respectively. Two typical TSDPs of the TD specimen deformed at 9% strain are shown in Fig. 4.8 for the major and random texture components. The TSDPs were evaluated using the CMWP procedure to obtain the dislocation densities ρ, the fraction of slip-system types, $h_{<a>}$ and $h_{<c+a>}$, and the area average crystallite size d_{area}, which are listed in Tables 4.1 and 4.2.

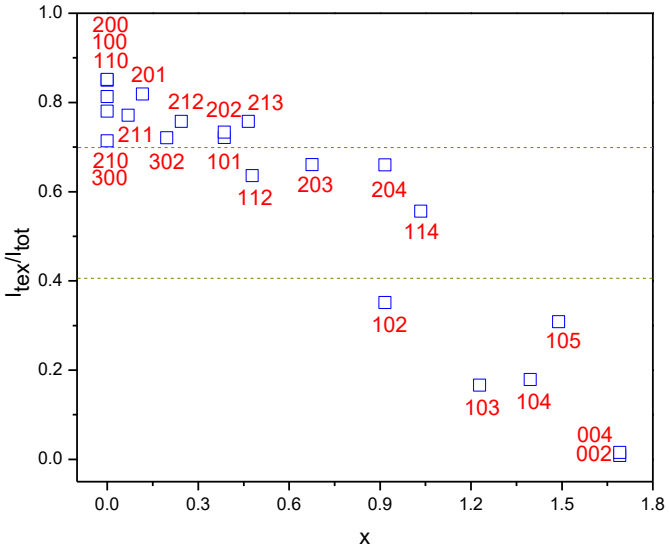

(a)

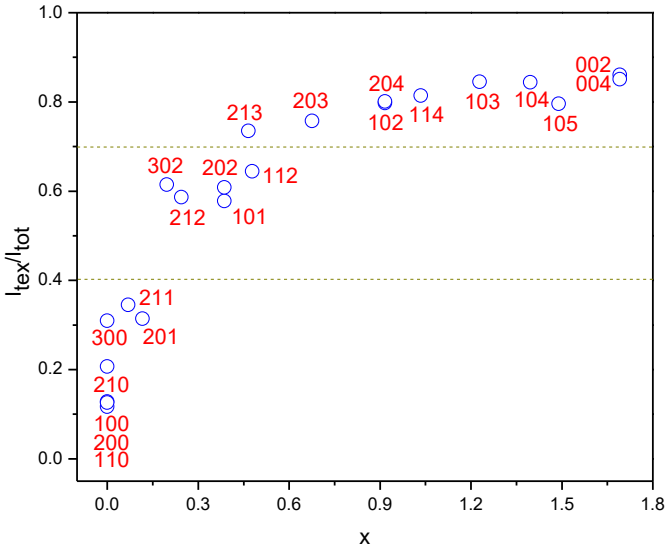

(b)

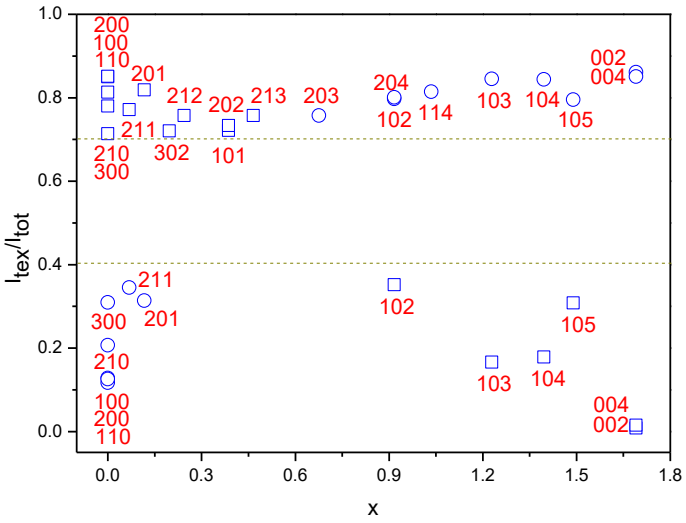

(c)

Fig. 4.6: The calculated values of the intensity ratios, I_{tex}/I_{tot}, for the rotation manner around the TD axis for the original specimen, the incident angle ω is 25° on the sample surface parallel to (a) the ND-TD plane and (b) the RD-TD plane, respectively, where $x = (2/3)(l/ga)^2$. Two dash lines divide the reflections into three groups from top to down, which are the group of the major texture component, the mixing component and the random texture component, respectively. (c) The reflections in the groups of the major and random texture components are selected and used to construct TSDP.

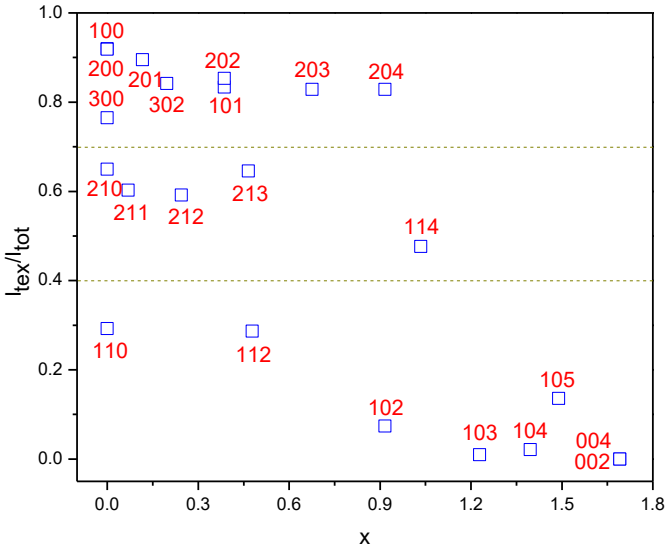

(a)

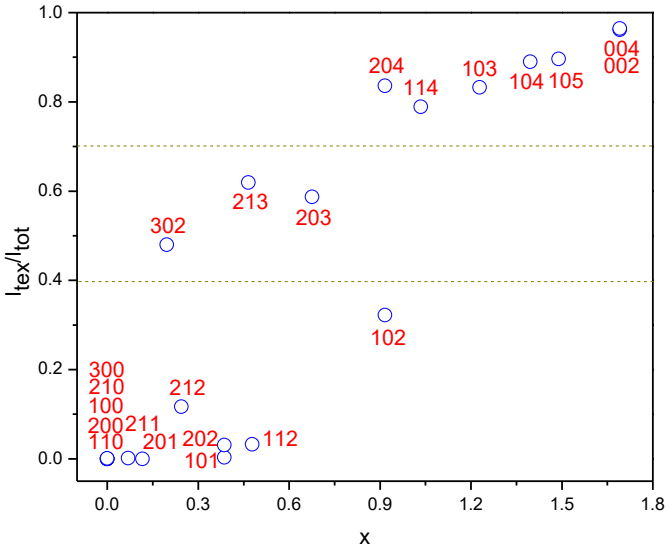

(b)

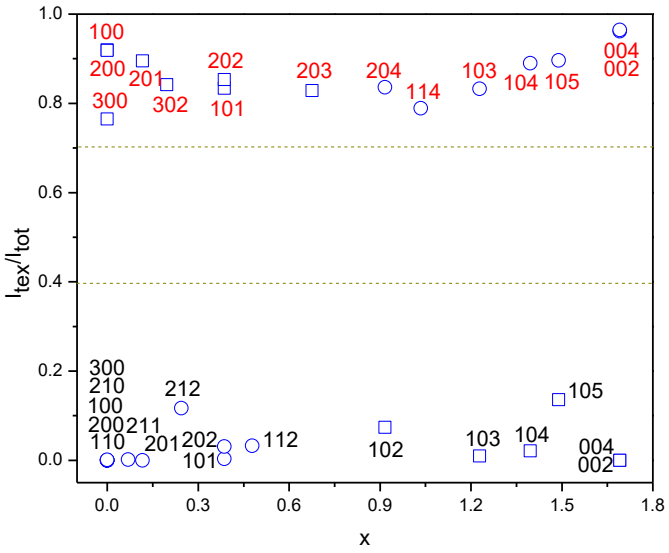

(c)

Fig. 4.7: The calculated values of the intensity ratios, I_{tex}/I_{tot}, for the rotation manners around the RD axis for the TD specimen at 9% strain, the incident angle ω is 25° on the sample surfaces parallel to (a) the ND-RD plane and (b) the TD-RD plane, respectively, where $x=(2/3)(l/ga)^2$. Two dash lines are the same as those in Fig. 4.6. (c) The reflections in the groups of the major and random texture components are selected and used to construct TSDP.

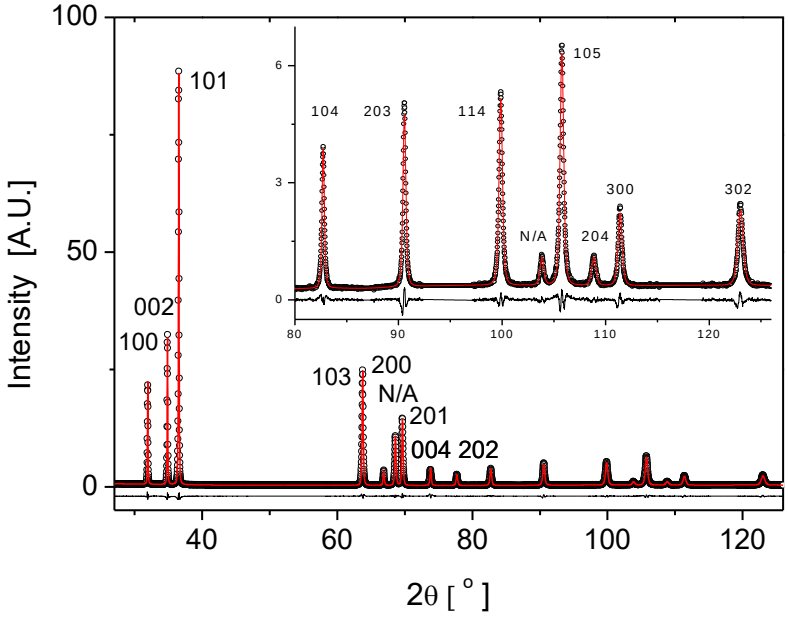

(a)

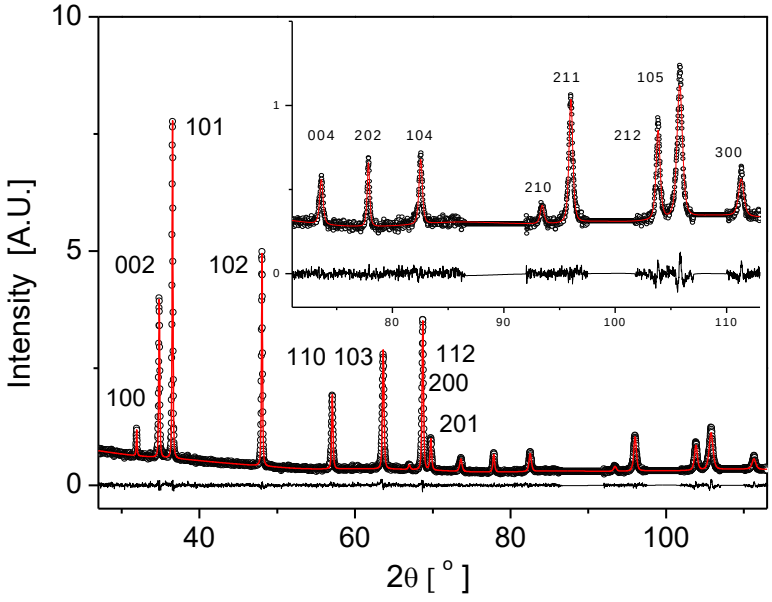

(b)

Fig. 4.8: The typical TSDP of the TD specimen at 9% strain for the (a) major and (b) random texture components. The black open circles and the red solid lines are the measured data and the calculated pattern by the CMWP procedure. The difference between the measured and calculated patterns is shown at the bottom of the figure. The labels 'N/A' indicate the reflections correspond to the other texture components.

The evolution of the dislocation densities in the major and random texture components with strain is shown for the RD and TD specimens in Fig. 4.9a. The fraction of <a>-type slip-systems vs. strain for the RD and TD specimens in the two texture components is shown in Fig. 4.9b. For the RD specimens, the dislocation densities in the major and random texture components increase with increasing deformation. At 2.5% strain the major texture component has a high fraction of <*a*>-type dislocations, whereas in the random texture component <*a*> and <*c*+*a*>-type dislocations are equally present. After 17% strain, the fraction of <*c*+*a*>-type dislocations increases in the major texture component, whereas it decreases in the random texture component. In the TD specimens, the dislocation densities in both, the major and the random texture components, reach a maximum at 9% strain and decrease slightly at 13% strain. In the major texture component up to 9% strain the <*a*> and <*c*+*a*>-type dislocation fraction does not change. At larger strain the fraction of <*a*>-type dislocations decreases. In the random texture component the <*a*>-type dislocations are dominating at all strain levels. The subgrain size values are varying between about 60 and 120 nm throughout the specimens and strain levels. The evaluation procedure to determine slip modes and Burgers vector types has also shown that the existence of <a>-type and <c+a>-type screw dislocations is statistically possible for the deformed RD and TD specimens. The details of this procedure can be found in Ref. (Ungár et al., 2007). This means that cross-slip can play a role in dynamic recovery during the deformation process of the present samples.

During the CMWP evaluation procedure {10.2} or {11.1} type tensile twinning and {11.2} or {10.1} type compressive twinning were allowed using the data files produced by Balogh et al. (2009). In all evaluated diffraction patterns the CMWP procedure gave zero density for all four twinning modes, even when data files were applied in combinations. The absence of tensile or compressive twinning provided by the X-ray line profile analysis in the present case is interpreted in the following manner. (a) The stress-strain curves shown in Fig. 4.1 do not indicate substantial twinning. (b) X-ray line broadening is affected only by twinning if the average distance between twin boundaries is smaller than about 2 μm. If the twinned regions between two twin boundaries are wider in average than this lower limit then they will not affect line profiles. This means that if X-ray line broadening indicates no twinning this only means that there are no narrow twin lamellae.

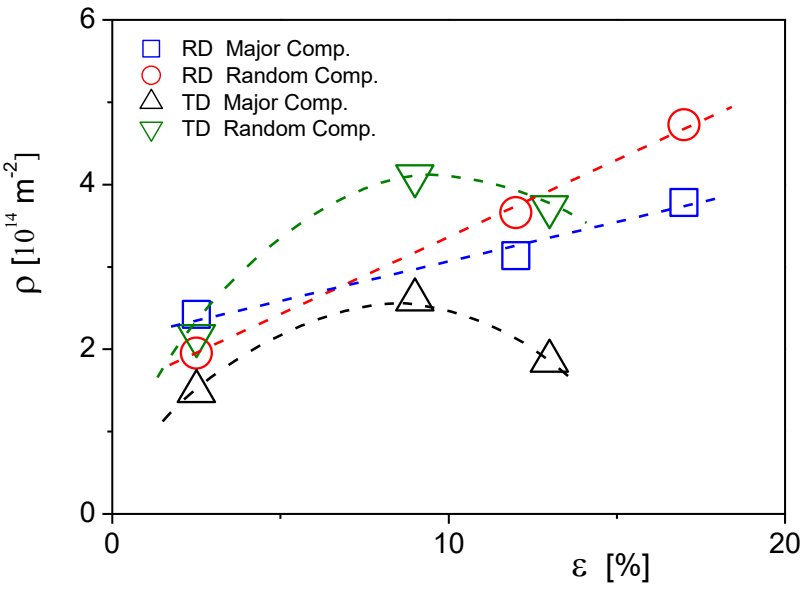

(a)

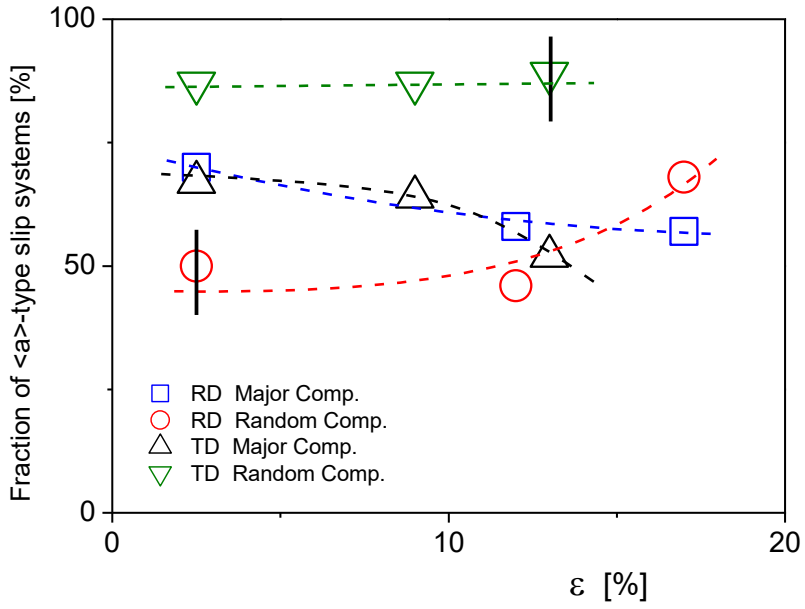

(b)

Fig. 4.9: (a) The dislocation densities, ρ, and (b) the fractions of the <a>-type slip-systems vs. the true strain, ε, for the RD major (open blue squares), the RD random (open red circles), the TD major (open black up-triangles) and the TD random (open olive down-triangles) texture components, respectively. The thick vertical lines are for error bars. The dashed lines only guide the eyes. Detailed errors are given in Tables 4.1 and 4.2.

Table 4.1: The area average mean crystallite size, d_{area}, the dislocation densities, ρ, the fractions of the prevailing dislocation types, $h_{<a>}$ and $h_{<c+a>}$ and the dislocation arrangement parameter M for the Zr samples deformed along RD.

Strain		d_{area} [nm]	ρ [10^{14} m^{-2}]	$h_{<a>}$	$h_{<c+a>}$	M
Major texture component	2.5%	100 (±6)	2.4 (±0.4)	70 (±10)	30 (±4)	5 (±1)
	12%	95 (±5)	3.1 (±0.6)	58 (±6)	42 (±5)	5 (±1)
	17%	90 (±5)	3.8 (±0.6)	57 (±6)	43 (±5)	4 (±1)
Random texture component	2.5%	65 (±4)	2.0 (±0.4)	50 (±6)	50 (±5)	3 (±1)
	12%	85 (±5)	3.7 (±0.6)	46 (±6)	54 (±5)	6 (±1)
	17%	60 (±4)	4.7 (±0.8)	68 (±7)	32 (±4)	7 (±1)

Table 4.2: The area average mean crystallite size, d_{area}, the dislocation densities, ρ, the fractions of the prevailing dislocation types, $h_{<a>}$ and $h_{<c+a>}$ and the dislocation arrangement parameter M for the Zr samples deformed along TD.

Strain		d_{area} [nm]	ρ [10^{14} m^{-2}]	$h_{<a>}$	$h_{<c+a>}$	M
Major texture component	2.5%	120 (±8)	1.5 (±0.3)	67 (±10)	33 (±4)	4 (±1)
	9%	120 (±8)	2.6 (±0.4)	64 (±10)	36 (±4)	5 (±1)
	13%	130 (±10)	1.9 (±0.3)	52 (±8)	48 (±5)	5 (±1)
Random texture component	2.5%	90 (±5)	2.2 (±0.4)	86 (±12)	14 (±3)	5 (±1)
	9%	85 (±5)	4.1 (±0.6)	87 (±12)	13 (±3)	4 (±1)
	13%	90 (±5)	3.7 (±0.5)	89 (±12)	11 (±3)	4 (±1)

4.2.3 Correlation between the microstructure and strength

Texture evolution and the activated slip-systems are closely correlated during the plastic deformation of Zr (Prakash et al., 2015). Since the deformation of the samples was imposed mostly on the major texture component, we investigate the mechanical response of the samples in terms of the microstructures of the major texture component firstly. As mentioned in §4.2.1, the yield stress, σ_y, of the RD samples is close to that of the TD samples, which means that the yield stress has no influence on the activation of the primary slip-systems in the two different specimens. The calculation of Schmid factor is consistent qualitatively with the observation. At the maxima of the major

texture component in the RD and TD samples, the Schmid factors of the primary slip-system $\{10\bar{1}0\}<11\bar{2}0>$ are 0.43 and 0.32, respectively. However, as shown in Figs. 4.1, 4.2 and 4.9b, the strain hardening, the texture evolution and the evolution of the fractions of <*a*> and <*c*+*a*>-type dislocation are significantly different in the two different loading directions. The increasing or the saturation trends in the stress-strain curves and the evolution of the dislocation densities are in good correlation with each other in the RD or TD samples.

We show that the texture evolution, described in detail in paragraph 4.2.1, can be explained directly by the evolution of the fractions of <*a*> and <*c*+*a*>-type dislocation in the RD or TD samples. Let us define the angle between the slip direction and the applied stress as λ, and the angle between the slip-plane normal and the applied stress as Φ. In the RD specimen two equivalent prismatic and four equivalent pyramidal <*a*>-type slip-systems can be activated for which the λ and Φ angles fulfill the condition: $\Phi > 45^{o} > \lambda$. In the RD samples multiple slip takes place in the early stage of deformation. For the loading direction along TD, there are also two equivalent prismatic <*a*> slip-systems and two equivalent pyramidal <*a*> slip-systems to be activated, however, since in this case the Φ and λ angles fulfill a different inequality, i.e. $\Phi < 45^{o} < \lambda$, a geometrical softening occurs with increasing strain (Partridge, 1967). As a consequence, the initial split-basal texture component splits up into four parts, as shown in Fig. 4.2c.

The evolution of texture and slip system activity will be discussed by taking into account that (i) the material consists of the major and the random texture components and that (ii) during plastic straining these two components have to be accommodated. In the major texture component of the RD samples the fraction of <*a*>-type dislocations decreases, while that of <*c*+*a*>-type dislocations increases with strain and the ductility of these samples is enhanced by increasing of <*c*+*a*>-type dislocation fractions. This behavior is consistent with the in-situ neutron diffraction analysis of a Zr-2.5Nb sample (Balogh et al., 2012; Long et al., 2016), in which the fraction of <*c*+*a*>-type slip-systems increased from 25% to 35% during tensile deformation in the RD. In the random texture component the opposite trend is observed, again to balance strain incompatibility between the two texture components. At low strains there are more <*c*+*a*>-type dislocations in the random texture component, whereas at the larger strains

there are more <*c*+*a*>-type dislocations in the major texture component. In the RD specimens stress partitioning and accommodation of strain incompatibility between the major and random texture components results in enhanced plasticity.

In the TD samples, up to 9% strain, the grains are aligning the [01$\bar{1}$0] direction parallel to the loading direction. During this process <*a*>-type slip-systems are dominating in both, the major and the random texture components. This indicates that <*a*>-type dislocations play a decisive role in the texture evolution. The plastic anisotropy in the TD samples is stronger than in the RD samples (Turner et al., 1995; Xu et al., 2008). Xu et al. (2008) have shown that the plastic strain ratio in tensile deformed Zircaloy-2 is about three times larger in the TD than in the ND directions, i.e. $R^{TD}(\varepsilon_{RD}:\varepsilon_{ND}) = 3.46$ and $R^{ND}(\varepsilon_{RD}:\varepsilon_{TD}) = 1.13$, respectively. This means that the TD samples are deformed almost in a plane-strain mode with the principle strain components in the RD-TD plane. Once the texture has changed, the TD sample continues to deform up to about 13% with new type of texture. However, in the random texture component the <*a*>-type slip-system is still dominating up to 13% stain, indicating that the internal stresses in these grains are not large enough to active more <*c*+*a*>-type dislocation activity. Once necking occurs in the TD samples, more stress concentrates in the necking region, activating more <*c*+*a*>-type dislocations even in the major texture component.

The flow stresses, σ, can be correlated with the dislocation densities, ρ, using the Taylor equation (Taylor, 1934):

$$\sigma = \sigma_0 + \alpha M_T G b \sqrt{\rho} \ , \tag{4.9}$$

where σ_0 is the friction-stress, α is a constant between zero and unity, G is the shear modulus, and M_T is the Taylor factor. We take $\sigma_y = R_{p0.1}$ for the value of σ_0. As discussed in paragraph 4.2.1 the offset yield points for the two directions, RD and TD, are the same: $R_{p0.1}$ = 150 (±15) MPa. Therefore, we set σ_0 = 150 MPa and G is 33 GPa. The Burgers vector, b, is the average of Burgers vectors weighted in terms of the fractions of the <*a*>-type and <*c*+*a*>-type dislocations, as listed in Tables 4.1 and 4.2. The dislocation density, ρ, is the volume average value of the dislocation densities for the major and random texture components.

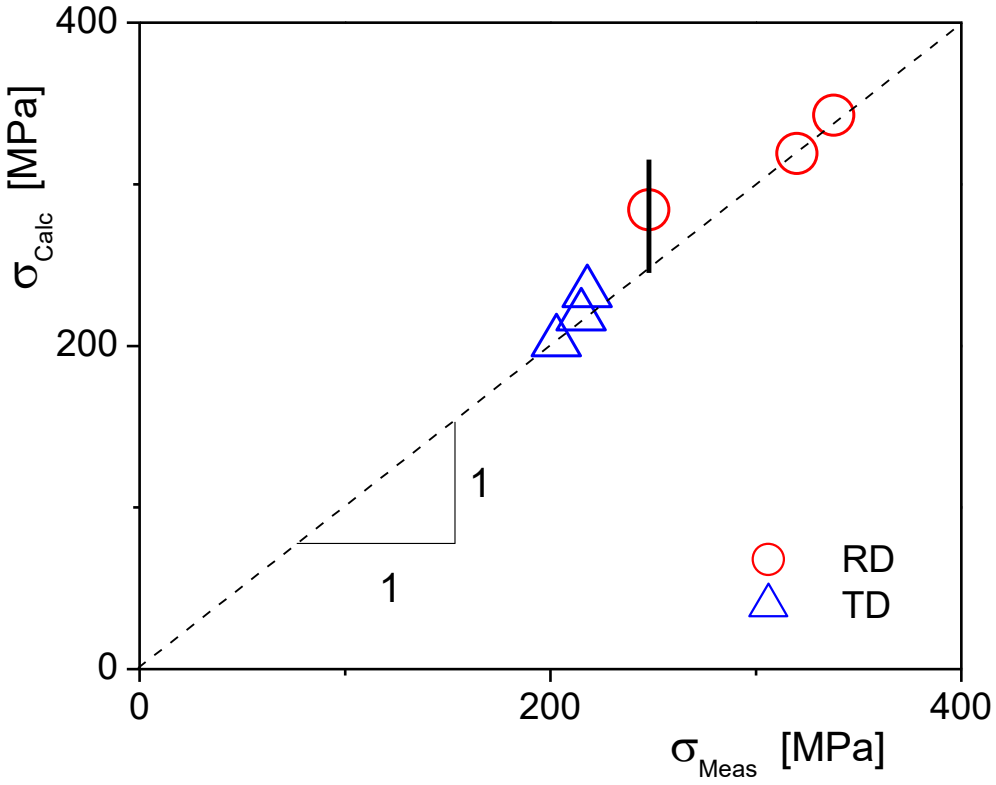

Fig. 4.10: Calculated σ_{Calc} vs. measured σ_{Meas} flow-stress values of the RD and TD samples, using eq. (4.9). The error bar is shown as a thick vertical line. The dashed line indicates the one-to-one correlation.

The appropriate Taylor factor and α values are assessed by matching the measured flow stress values in eq. (4.9). MacEwen et al. (1981) discussed the possible Taylor factor values in textured alpha-Zr and concluded that any value between 2.5 and 4 would be possible. Based on the work of Luton and Jonas (1972), Troyanova et al. (1985) are using $M_T = 2$, whereas Dunlop et al. (2007) assume $M_T = 4$. The value of α shows the effectiveness of the dislocation structure in work hardening (Mughrabi, 2016) and it is in strong correlation with the dipole character of the dislocation structure (Mughrabi, 1987). The dipole character of the dislocation arrangement, as discussed in paragraph 4.1.5, is given by the *M* parameter. The *M* values given by the CMWP evaluation are listed in Tables 4.1 and 4.2. The *M* values vary between 3 and 7 indicating an average dipole character which is substantially the same in the two sample types and does not change with deformation. From this we conclude that the α value is the same in the TD and RD samples and remains the same during plastic straining. Assuming $\alpha \cong 0.16$ and

using the other values for eq. (4.9) as discussed above the Taylor factor values are obtained as follows: M_T = 2.5 for the TD and M_T = 3.5 for the RD specimens. The calculated and the measured flow stress values, σ_{Calc} and σ_{Meas}, are shown in Fig. 4.10. The two Taylor factor values, M_T = 2.5 and M_T = 3.5, for the TD and RD specimens are rather effective values complying more with the experimental stress-strain curves than purely with the Schmid factors of the active slip systems. The Schmid factor only takes into account the slip geometry and ignores the work needed to activate the slip systems with very different Burgers vectors in the different slip systems in *hcp* Zr. To account for such an energetic aspect in the Taylor factor needs further considerations beyond the scope of the present work.

Chapter 5

Microstructure and strength of a V-5Cr-5Ti alloy processed by high pressure torsion

We investigate the processes of grain refinement and dislocation density evolution induced by HPT up to shear strain values of γ = 290 at two different hydrostatic pressures of 4 and 8 GPa, respectively. We have also investigated the thermal stability of the deformed microstructure up to 1200 °C. Microhardness was measured at different positions of the HPT deformed specimens and quasi stress-strain curves were obtained. X-ray diffraction patterns were measured at different positions of the HPT disks by a dedicated high-angular resolution X-ray diffractometer capable of micro-diffraction. The diffraction patterns were evaluated for dislocation density, crystallite size and dislocation arrangement parameters using the procedure of X-ray line profile analysis. The mechanical properties and the microstructure of the specimens were analyzed in terms of the Taylor equation.

5.1 Experimental

5.1.1 Samples

Severe plastic deformation techniques have been widely used to produce bulk nanostructured materials (Valiev et al., 2000, 2006). After the deformation with a very high strain, huge amounts of dislocations are prevailing and arranged into low- or high-

angle grain boundaries in the bulk solid. Therefore, the grain size of the coarse-grained material is refined down to micrometer and even to the nanometer level. The fine grains and high density of dislocations can improve significantly the strength of the bulk nanostructured material. During the SPD processing, the overall dimensions of the material are nearly retained, and both the contamination and the porosity could be avoided. Now, there're several available SPD procedures, such as equal channel angular extrusion (Valiev & Langdon, 2006), high pressure torsion (Zhilyaev & Langdon, 2008), multidirectional forging (Salishchev et al., 1993), accumulative roll bonding (Saito et al., 1998), and cyclic extrusion and compression (Richert & Richert, 1986).

As one of SPD techniques, HPT procedure, proposed firstly by Bridgman (1943), received considerable attentions in the last several decades. The specimen is machined in the form of a disk, and located between two anvils. A high pressure is applied on the sample, and the lower anvil is rotated simultaneously. Because of the surface friction between the sample and the anvils, the sample is subjected to continuous torsional straining. During the HPT processing, some materials are actually flowed outward which is usually denoted as the case of quasi-constrained. The component of high hydrostatic pressure imposed on the sample can suppress the dynamic recovery process of dislocations, therefore extremely fine grain size could be obtained. After a certain number of revolutions, the microstructure is homogeneously distributed in the disk due to large torsional straining.

The HPT specimens of 10 mm diameter and ~0.7 mm thickness were cut from the V-5Cr-5Ti alloy. The discs were machined from an annealed metal bar produced by the General Research Institute for Nonferrous Metals, China. The chemical composition of the specimens is given in Table 5.1. For the initial V-5Cr-5Ti specimens, the grain size was ~200 μm and the dislocation density was below about 10^{12} m^{-2}. Two pressure values of 4 and 8 GPa were selected for the HPT deformation at room temperature. These relatively large pressure values were selected in order to avoid slipping of the disks during HPT. Six different rotations, i.e. 0.25, 0.5, 1, 2, 4 and 8, were implemented at a speed of 0.2 rotation/min at each of the two pressure values, respectively. Shear deformation, γ, as a function of the radius, r in the HPT deformed disk has been evaluated as (Skrotzki et al., 2013):

$$\gamma = \frac{r2\pi\chi}{l360^\circ}\ , \qquad (5.1)$$

where χ is the angle of rotation in degrees and l is the thickness of the disk. Measurements carried out on HPT deformed specimens are denoted by the pressure, rotation and radial position. For example the notation 4G-2rot-0.5*R* means that the specimen was deformed by 2 rotations at 4 GPa pressure and the measurement was done at half radius of the disk. In order to avoid surface damage by the HPT plunger the disks were polished and chemically etched before hardness and X-ray diffraction measurements.

Table 5.1: The chemical composition of the V-5Cr-5Ti specimens in wt%.

Element	Cr	Ti	Fe	Cu	Si	O	N	C	V
Composition	5.06	4.94	≤0.02	≤0.005	≤0.03	≤0.03	≤0.01	≤0.01	left

5.1.2 X-ray diffraction experiments

X-ray diffraction measurements were carried out in a special high-resolution diffractometer dedicated to line profile analysis with a plane Ge (220) primary monochromator operated at the Cu Kα fine-focus rotating copper anode (Rigaku, RA-MultiMax9) at 40 kV and 100 mA (Ungár et al., 1998). The distance between the source and the monochromator was 240 mm. A slit of 160 μm was put before the monochromator to cut off the $K\alpha_2$ component of the X-ray beam. With this arrangement the Cu $K\alpha_1$ beam on the specimen surface has a size of about 0.2×1.5 mm. The diffraction geometry is of parallel-beam type. With the stationary specimens the scattered radiation was registered by two flat imaging plates with a linear spatial resolution of 50 μm. The IPs were placed at a distance of 300 mm from the specimen covering the 2θ angular range between 38 and 148 degrees. The distance between the specimen and detector was selected such that the instrumental effect was always less than 10% of the physical broadening of the peaks. The diffraction patterns were obtained by integrating the intensity distributions along the corresponding Debye-Scherrer arcs on the IPs. Only the central parts of the arcs were used for the integration where the curvature does not affect line broadening. The X-ray beam was positioned on the specimen surface by using a low-depth-resolution microscope coupled to a television screen. The X-ray diffraction measurements were done at the center, at half

radius and close to the edge of the samples, denoted as 0R, 0.5R and 1R, respectively. Two more positions at a quarter and three-quarter radius, i.e. 0.25R and 0.75R, were also measured on the specimens deformed by 4 and 8 rotations, respectively.

5.1.3 Microhardness measurements

The strength of the HPT processed specimens has been investigated by measuring the Vickers hardness HV in a Zwick/Roell-ZHμ-Indentec microhardness tester. HV measurements were done at the same positions of the specimens where the X-ray diffraction experiments were carried out. The HV values at the same radius, HV(r), were averaged and used to calculate the flow stress as a function or r: $\sigma(r)$ = HV(r)/3. The flow stress $\sigma(r)$ is shown as a function of shear deformation in a quasi stress-strain curve in Fig. 5.1. The figure shows that the flow stress values of the specimens deformed at 4 and 8 GPa are the same within experimental error with the same saturation value of about 1220 (±40) MPa.

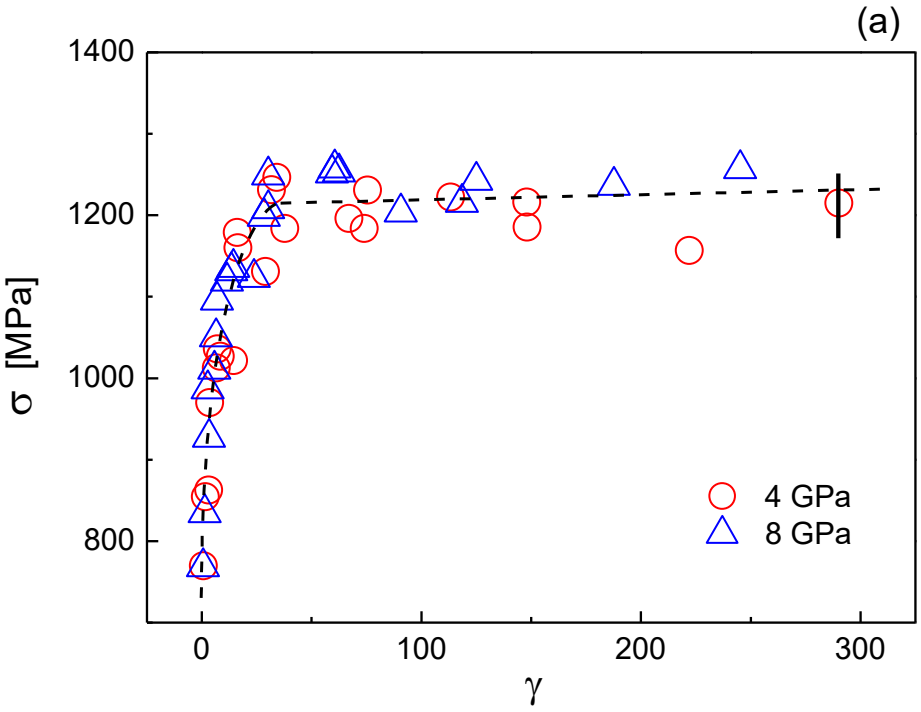

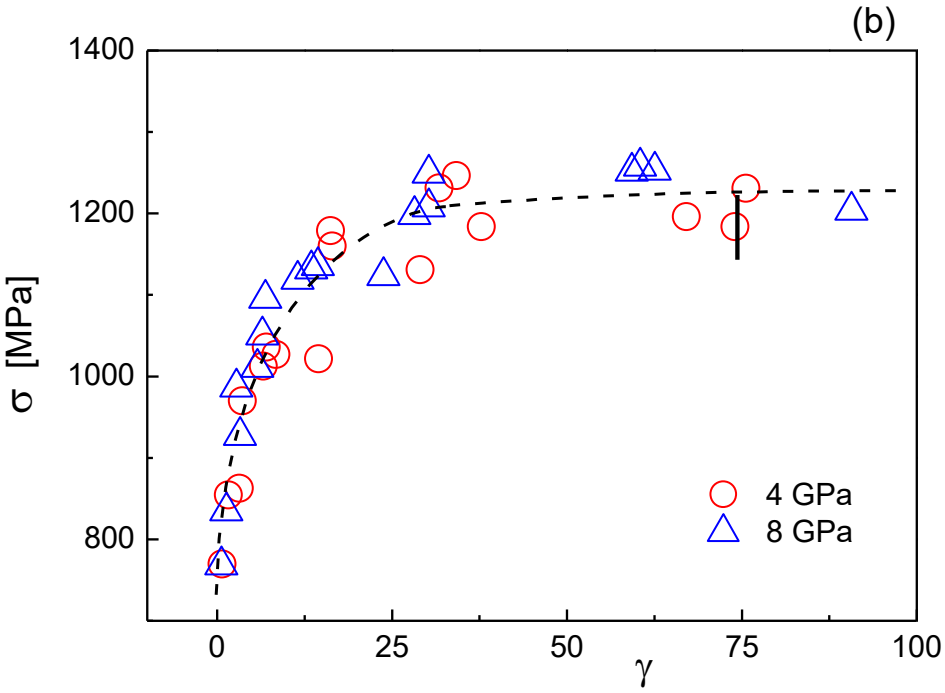

Fig. 5.1: (a) Quasi stress-strain curves of the V-5Cr-5Ti specimens deformed by applying 4 (open red circles) and 8 GPa (open blue triangles) pressures. (b) Zoomed γ range up to γ = 100 showing the first part of work hardening. The dashed lines are to guide the eye. Error bars are shown as thick vertical lines.

5.1.4 Electron microscopy and heating experiments

The transmission electron microscope studies were carried out in a Philips CM-20 electron microscope working at 200 KeV. TEM thin-foil specimens were prepared from the 4 and 8 GPa specimens, each HPT deformed to about γ = 300. After mechanical polishing the specimens were prepared by the conventional twin-jet electropolishing technique using a solution of 25 vol.% nitric acid and 75 vol.% methanol. Two typical TEM micrographs of the specimen deformed at 4 GPa by 4 rotations and taken from the half-radius and from the disk edge region are shown along with the corresponding grain-size distribution bar diagrams in Fig. 5.2. The thermal stability of the microstructure was tested by heating experiments up to 1200 °C. Three quarter pieces of the 4 GPa 4 rotation HPT deformed specimen were heated in a SETARAM DTA-92 type differential thermal analyzer in dry Ar atmosphere to 800, 1000 and 1200 °C and kept at each temperature for 30 min. After heat treatment the specimens were cooled in

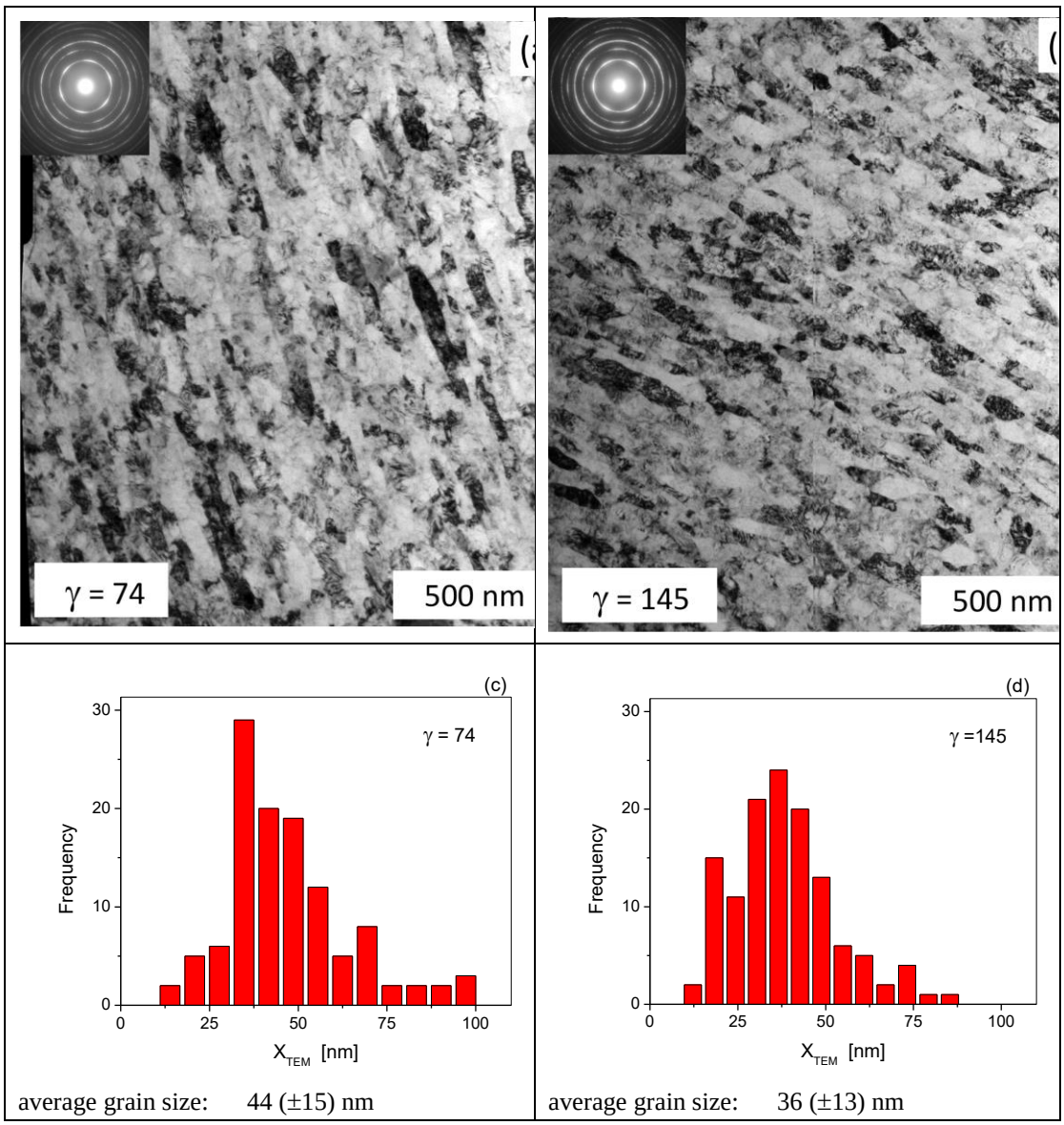

Fig. 5.2: TEM micrographs of the specimens deformed to γ = 74 (a) and γ = 145 (b). Grain size distributions from the two micrographs are in (c) and (d). The numbers in brackets in (c) and (d) are the standard deviations of the average grain size values.

the DTA equipment. Chemical etching was applied to remove the damaged surface layer before X-ray measurements for line broadening.

5.1.5 Evaluation of the X-ray diffraction experiment

Usually, HPT produces large dislocation densities and sub-micron grain size due to large torsional deformation. According to the kinematical theory of X-ray diffraction, small crystallite size and large lattice distortions are causing peak broadening in diffraction patterns (Warren, 1959). The dislocation density and arrangement, the dislocation characters and the crystallite size have been evaluated by using the CMWP line profile analysis procedure (Ungár et al., 1999, 2010; Ribárik et al., 2019). The theoretical models of dislocation and crystallite size implemented in the CMWP are described briefly as follows. According to the Krivoglaz-Wilkens theory the mean square strain $\langle \varepsilon_{g,L}^2 \rangle$ in dislocated crystals is (Wilkens, 1970a; Krivoglaz, 1996):

$$\langle \varepsilon_{g,L}^2 \rangle \cong \frac{\rho \bar{C} b^2}{4\pi} f(\eta) , \tag{5.2}$$

where g is the length of the diffraction vector, L is the Fourier variable, ρ and b are the density and the Burgers vector of dislocations, $\bar{C}$ is the average dislocation contrast factor and $f(\eta)$ is the strain function. The $f(\eta)$ function describes the L dependence of the mean-square-strain with $\eta = L/R_e$, where R_e is the effective outer cut-off radius of dislocations. The dislocation contrast factors can be averaged over the permutations of *hkl* if the sample is a polycrystalline or if all possible Burgers vectors are activated. For cubic crystals the average contrast factor can be given as (Ungár & Tichy, 1999):

$$\bar{C} = \bar{C}_{h00}(1 - qH^2) \ , \tag{5.3}$$

where $\bar{C}_{h00}$ is the average contrast factor of the *h00* reflections and $H^2 = (h^2k^2+h^2l^2+k^2l^2)/(h^2+k^2+k^2)^2$. The q parameter depends on the elastic constants of the crystal and the type of dislocations, and can be evaluated numerically (Ungár et al., 1999; Borbély et al., 2003). The crystallite size, i.e. the coherent domain size, obtained from X-ray line broadening is evaluated by assuming log-normal size distribution given by the median, m and the variance, κ (Hinds, 1982). Experience has shown that the best correlation with grains size in TEM is obtained with the area average mean crystallite

size (Ungár et al., 2005):

$$\langle x \rangle_{area} = m \times \exp(2.5\kappa^2) \, . \qquad (5.4)$$

Although the CMWP procedure can also provide the density of planar defects in the present case we did not use this option because the V-5Cr-5Ti alloy has a high stacking fault energy and no twinning was observed under quasi-static deformation conditions (Gui et al., 2016). Typical CMWP evaluated diffraction patterns are shown in Fig. 5.3. The measured (open circles) and calculated (solid red lines) diffraction patterns of specimens deformed at 4 GPa γ = 0.37 and 8 GPa γ = 125 whereas 4 GPa γ = 37 and held at 1200 °C for 30 min are compared in Figs. 5.3a and 5.3b, respectively. The patterns are in logarithmic intensity scale and are shifted relative to each other to avoid overlapping.

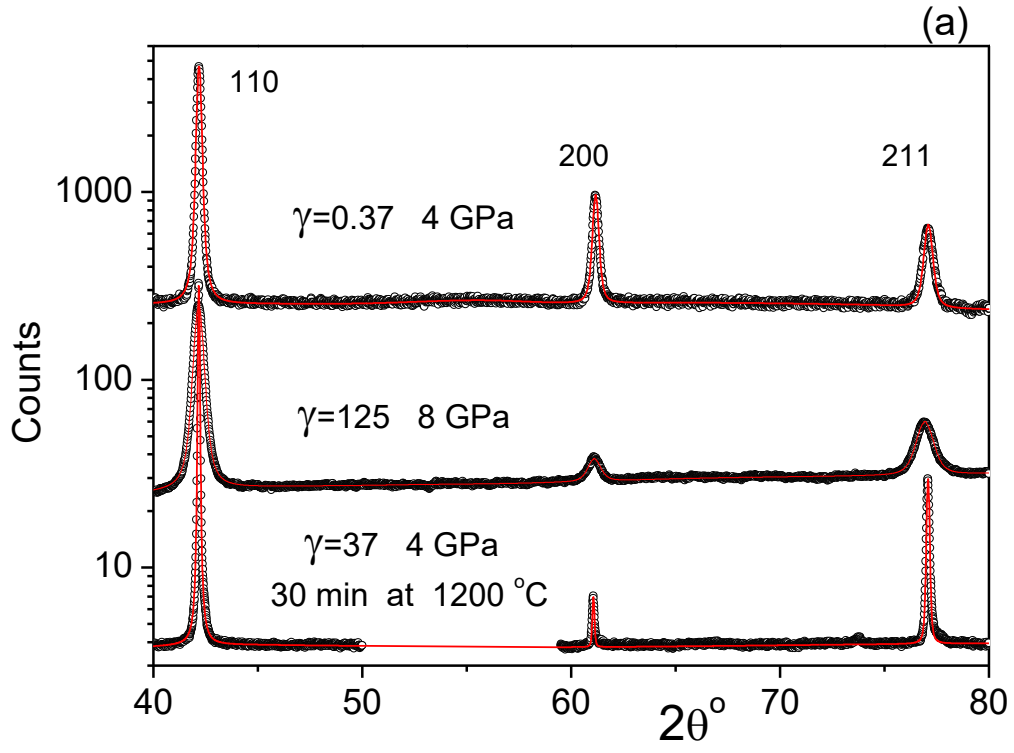

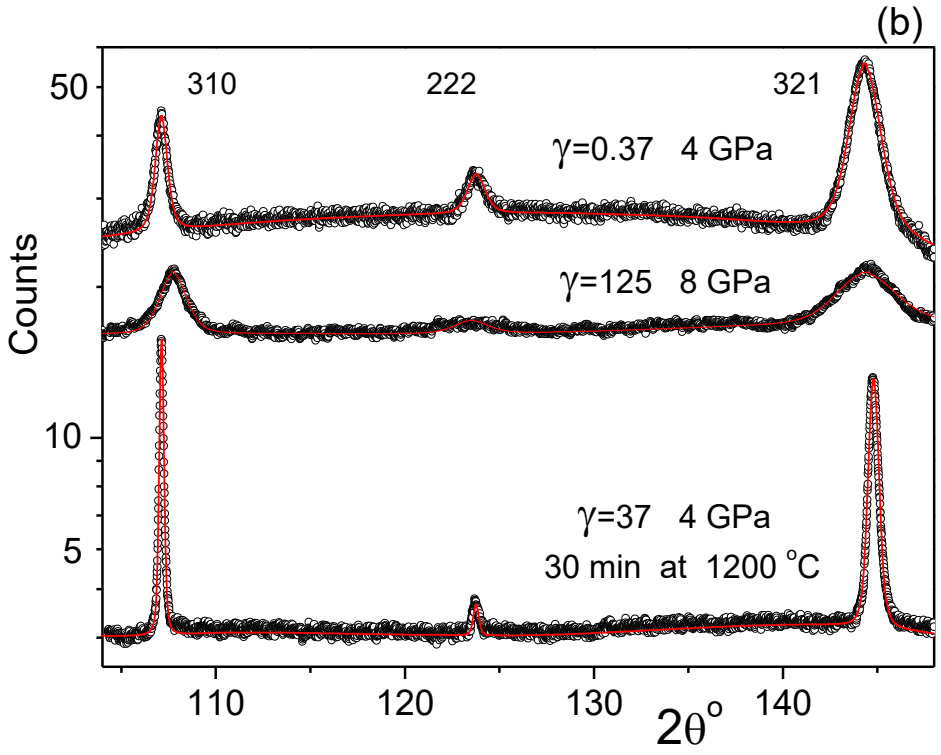

Fig. 5.3: The measured (open black circles) and the fitted (solid red lines) diffraction patterns of the V-5Cr-5Ti specimens deformed at 4 GPa $\gamma = 37$ and 8 GPa $\gamma = 125$ and the 4 GPa $\gamma = 37$ deformed sample held at 1200 °C for 30 min. (a) is the first and (b) the second half of the diffraction patterns, respectively.

5.2 Results and discussion

5.2.1 Dislocation densities and crystallite size of the HPT deformed specimens

The effect of microstrain and crystallite size on line broadening can be well observed qualitatively in the Williamson-Hall (WH) (Williamson & Hall, 1953) and modified Williamson-Hall (mWH) (Ungár & Borbély, 1996) type plots of full widths at half maxima. If the elastic anisotropy in the materials is strong the FWHM values in the WH plot reveal strongly non-monotonous increase versus K, where $K = 2\sin\theta/\lambda$ (Ungár & Borbély, 1996). The effect of elastic anisotropy can be rationalized in the mWH plot by replacing K by $K\sqrt{\bar{C}}$ (Ungár & Borbély, 1996). In the mWH plot the FWHM values usually follow a straight line where the slope is qualitatively proportional to the

microstrain, and the intercept at $K = 0$ is inversely proportional to the crystallite size. The WH and mWH plots of the V-5Cr-5Ti specimens deformed at 4 or 8 GPa to different rotations and measured on the disks at the center (black open triangles), at 0.5R (red open circles), and at 0.75R (blue open squares) positions are plotted in Figs. 5.4a to 5.4d, respectively. The FWHM values in the WH plots almost follow a linear trend in accordance with the relatively weak elastic anisotropy of V, i.e. $2c_{44}/(c_{11}-c_{12}) \cong 0.779$ (Bolef et al., 1971). In the mWH plots the same average contrast factors were used as provided by the CMWP evaluation. The slopes of the straight lines in these plots are increasing with deformation up to about $\gamma \cong 40$ while the intersections at $K = 0$ are increasing in agreement with decreasing crystallite size within the same deformation range.

Quantitative evaluation of line broadening was done by the CMWP procedure. The results of the crystallite size d_x and the dislocation density ρ are shown in Fig. 5.5 for the samples after deformation at 4 and 8 GPa pressures. The crystallite size decreases with shear strain up to a value of about $\gamma = 15$. Beyond that the crystallite size remains nearly unchanged at a value of $d_x \cong 31$ (±2) nm, as shown in Fig. 5.5c. The TEM micrographs in Fig. 5.2 show that the grains are elongated in the shear direction, a typical grain morphology in HPT deformed specimens (Stolyarov et al., 2003; Lowe & Valiev, 2004; Toth & Gu, 2014). The grain size, d_{TEM} is determined normal to the shear direction. It was obtained for strain values of $\gamma = 74$ and $\gamma = 145$ from the TEM micrographs in Figs. 5.2a and 5.2b as $d_{TEM} = 44$ (±15) nm and $d_{TEM} = 36$ (±13) nm, respectively, as shown in Figs. 5.2c and 5.2d. respectively. Both d_{TEM} values are larger than the saturation value of subgrain size, i.e. $d_x \cong 31$ (±2) nm. However, the TEM grain size is still decreasing after $\gamma = 15$ indicating that grain refinement proceeds while the subgrain size has already been saturated. The TEM grain size at $\gamma = 145$ normal to the shear direction, i.e. $d_{TEM} = 36$ (±13) nm, is almost identical to the subgrain size given by X-ray diffraction, i.e. $d_x \cong 31$ (±2) nm. The fact that the subgrain size saturates at a relatively early deformation stage at about $\gamma = 15$ and that the TEM grain size approaches this value at $\gamma = 145$ indicates that the lowest grain size attainable by plastic deformation at RT in this alloy is most probably around 31 (±2) nm.

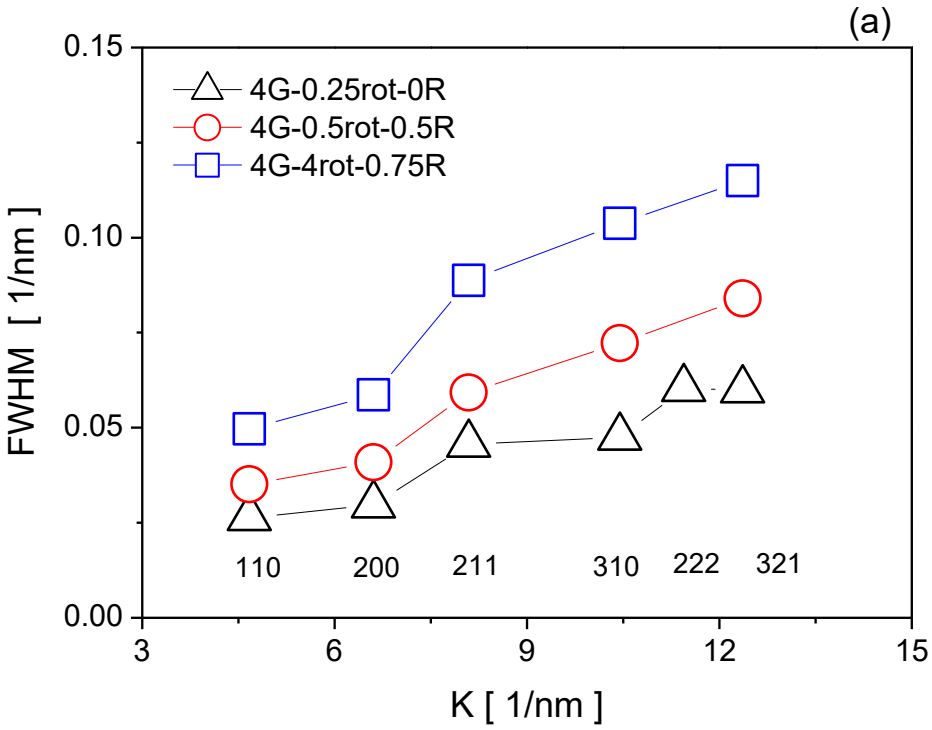
(a)
0.15
0.10
0.05
0.00
FWHM [1/nm]
4G-0.25rot-0R
4G-0.5rot-0.5R
4G-4rot-0.75R
110
200
211
310
222
321
3
6
9
12
15
K [1/nm]

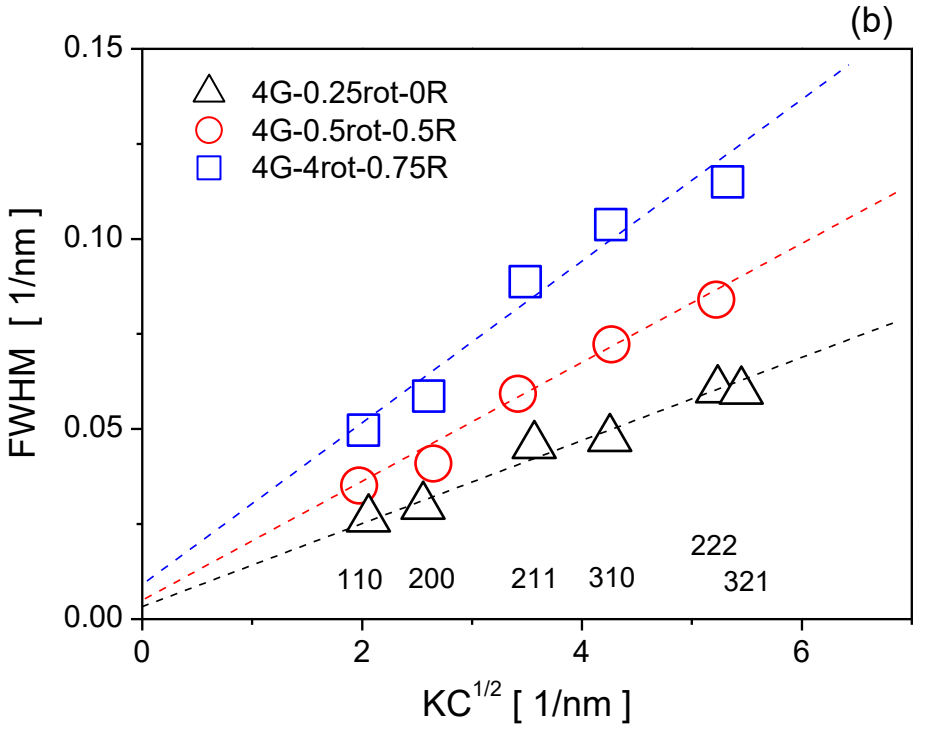
(b)
0.15
0.10
0.05
0.00
FWHM [1/nm]
4G-0.25rot-0R
4G-0.5rot-0.5R
4G-4rot-0.75R
110
200
211
310
222
321
0
2
4
6
KC^1/2 [1/nm]

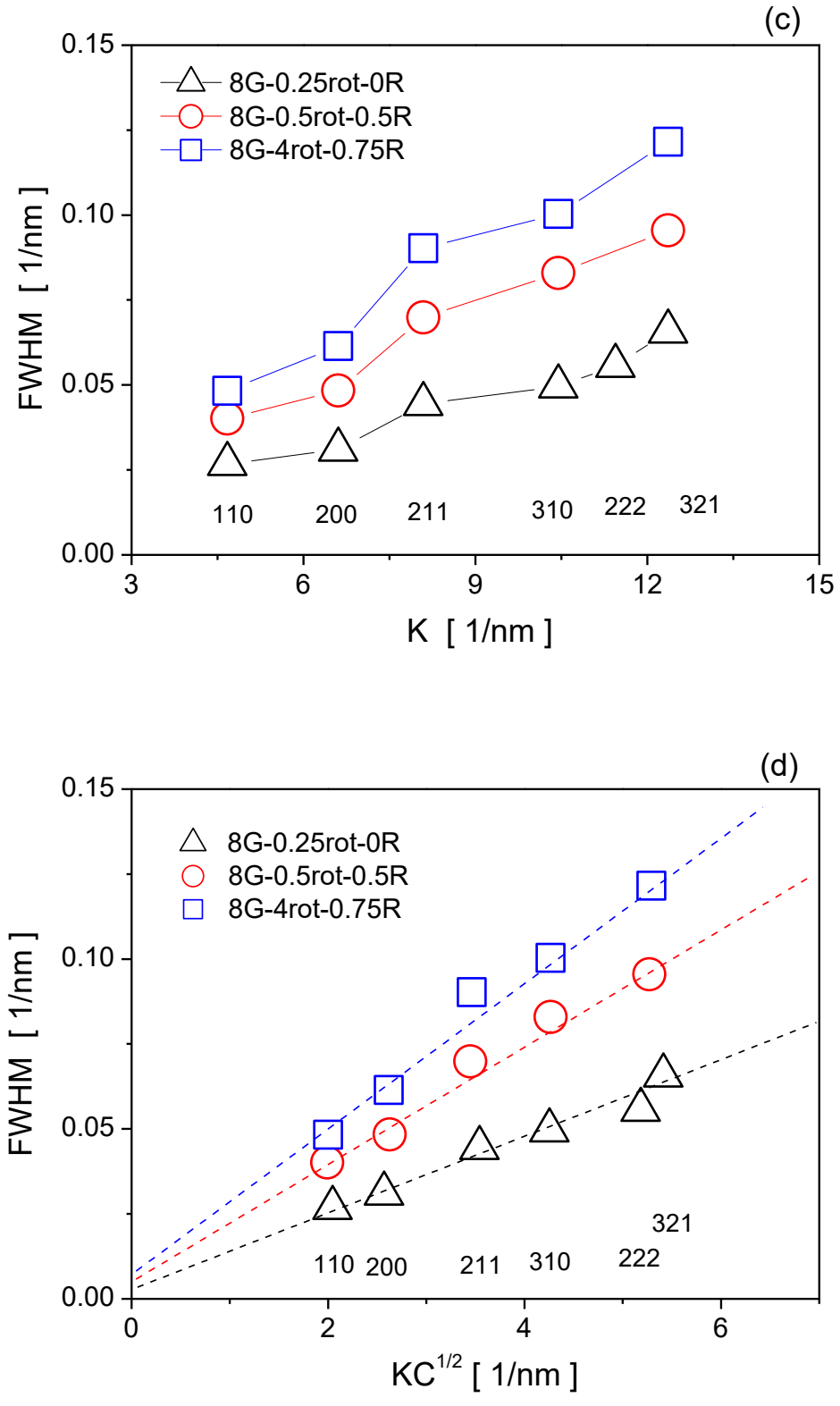

Fig. 5.4: WH (a) and mWH (b) plots of the FWHM after deformation at 4 GPa pressure. WH (c) and mWH (d) plots of the FWHM after deformation at 8 GPa pressure.

The dislocation density increases and saturates only at a much larger strain than the crystallite size, i.e. it increases up to about $\gamma = 75$ and saturates at a value of about 82×10^{14} m^{-2}. This is shown in Fig. 5.5c, where ρ and d_x are plotted together up to $\gamma = 100$. The crystallite size stops decreasing while the dislocation density is still increasing with strain. A similar phenomenon was also observed earlier in HPT deformed Nb and Ta (Jóni et al., 2013). Comparing the values of the crystallite size and the dislocation density in the V-5Cr-5Ti specimens at 4 and 8 GPa pressures, they are nearly the same within the experimental uncertainty.

In pure *fcc* Cu and in pure *bcc* Nb and Ta, the dislocation density was found to be smaller after HPT deformation at higher pressure (Schafler, 2010; Jóni et al., 2013). In the case of these pure metals this was explained by the reduced vacancy mobility under large hydrostatic pressures (Jóni et al., 2013). During large plastic deformation in HPT deformation most of the dislocations carrying strain annihilate creating large numbers of excess vacancies and interstitials. While the pressure is applied point defect mobility is hampered resulting in retaining of excess point defects. When the specimen is unloaded and the hydrostatic pressure released the mobility of point defects is instantaneously enhanced. This enhanced diffusion enables substantial annihilation of dislocations. At larger pressure the retention of excess point defects is larger, therefore the instantaneous annihilation of dislocations at the moment of unloading will also be more effective. In the present HPT experiments we could not observe any remarkable differences in the dislocation densities of specimens deformed either at 4 or 8 GPa. Fig. 5.5b shows that the dislocation densities saturate around the same level of about 82×10^{14} m^{-2} within experimental error. This remarkable result indicates that in the V-5Cr-5Ti alloy even an enhanced point defect concentration cannot easily annihilate the dislocations produced by plastic deformation. The heating experiments, discussed below, show a fairly stable microstructure up to about 800 °C in correlation with the relatively stable dislocation density discussed here.

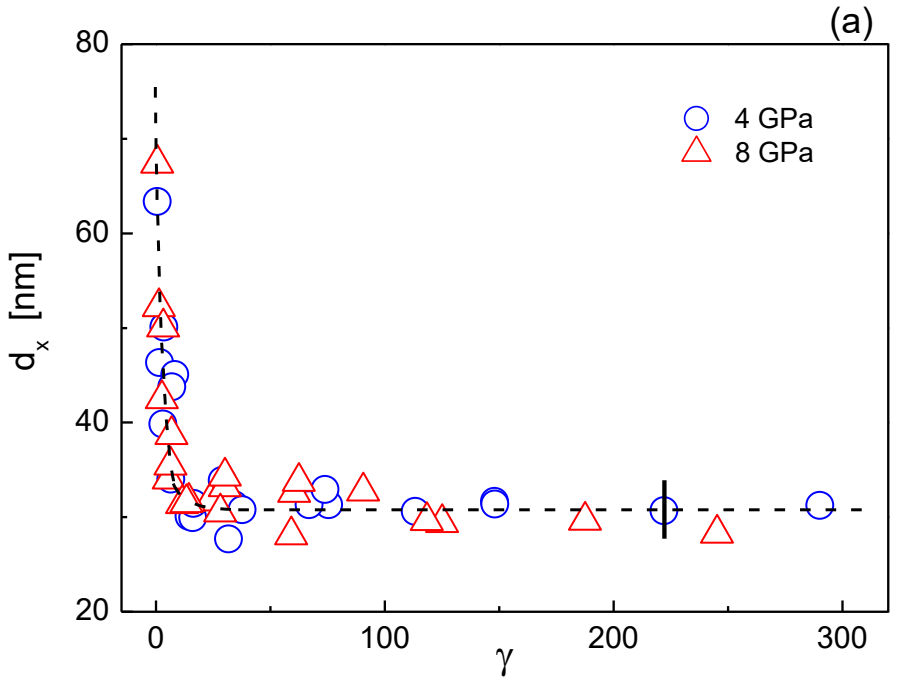
(a)
80
60
40
20
d_x [nm]
0
100
200
300
γ
4 GPa
8 GPa

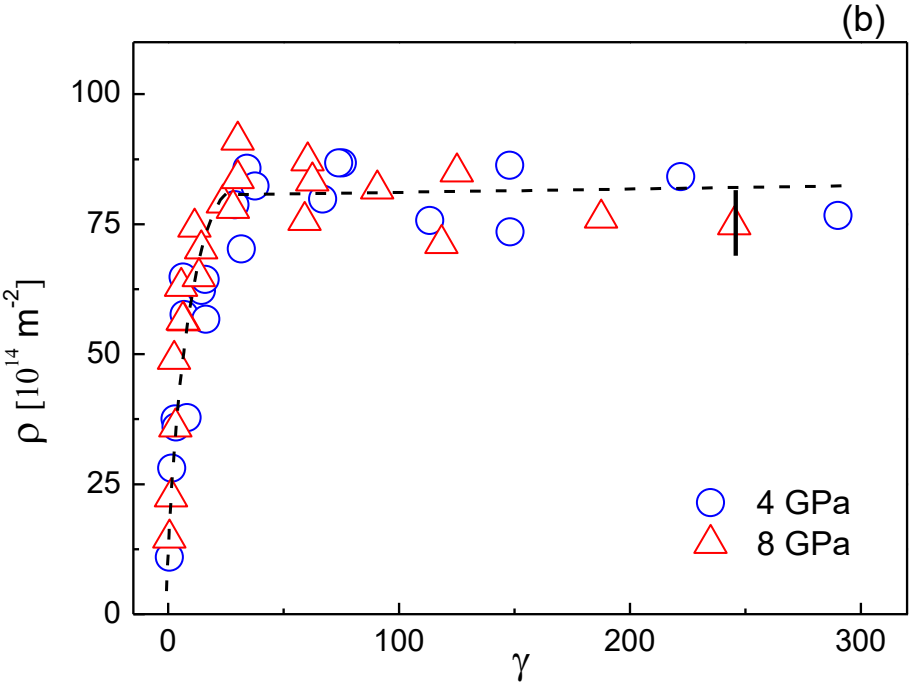
(b)
100
75
50
25
0
ρ [10^{14} m^{-2}]
0
100
200
300
γ
4 GPa
8 GPa

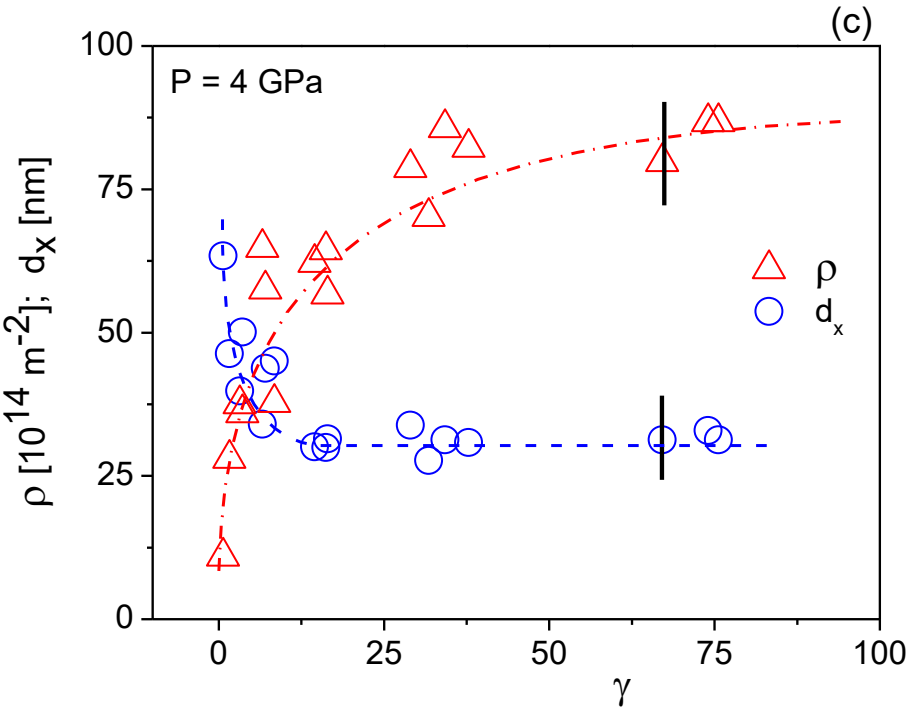

Fig. 5.5: (a) Area average mean crystallite size d_x, (b) dislocation density ρ of the V-5Cr-5Ti specimens after deformation at 4 and 8 GPa pressures *vs*. the shear strain γ. (c) The d_x and ρ values *vs*. γ up to γ = 100 for the specimen deformed at 4 GPa. Error bars are shown as thick vertical lines.

5.2.2 Dislocation character and arrangement

Strain anisotropy of peak broadening in the diffraction pattern is accounted for by the average dislocation contrast factor, $\bar{C}$. It is given by Eq. (5.3), where q is the physical parameter fitted in the CMWP procedure. As discussed above q depends on the edge or screw character of dislocations and the elastic anisotropy of the crystal. According to the numerical calculations (Ungár et al., 1999; Dragomir & Ungár, 2002b; Borbély et al., 2003), the theoretical values of q are -1.4 and 1.7 for the edge and screw dislocations in the a/2<111>{110} slip system, respectively. As shown in Fig. 5.6a, the experimental values of q vary in the range of -1.4 and 0, which indicates that the majority of dislocations are of edge character. The results are in good correlation with the earlier work on *bcc* Nb and Ta, where also edge dislocation character was found to be dominant after HPT deformation (Jóni et al., 2013). Solute atoms can also shift the dislocation character towards edge type as it was found in mechanically alloyed Al-Mg

(Gubicza et al., 2004). With increasing the nominal Mg content the dislocation character was shifting towards edge type. This finding is in correlation with stronger pinning of edge dislocations by solute atoms. In the present V-5Cr-5Ti alloy substantial Cr and Ti additions are in solid solution preferentially pinning edge dislocations. The dislocation arrangement parameter, $M = R_e\sqrt{\rho}$, describing the dipole character of dislocations, is shown *vs.* γ in Fig. 5.6b. Smaller M values co rrespond to stronger dipole character (Wilkens, 1970a, 1970b). The value of M parameter decreases rapidly to a level of about $M = 6$ (± 1) with increasing strain. The result indicates that the dipole character of dislocations becomes somewhat stronger compared to the initial state of the sample, however, even at large strains it does not become really significant. This behavior is in good correlation with the TEM micrographs in Fig. 5.2 which show that in this specimen there is no dislocation cell formation. In pure Cu which is a typical dislocation cell forming metal the M value can reach around $M \cong 1$ when persistent slip bands are forming (Wilkens et al., 1980).

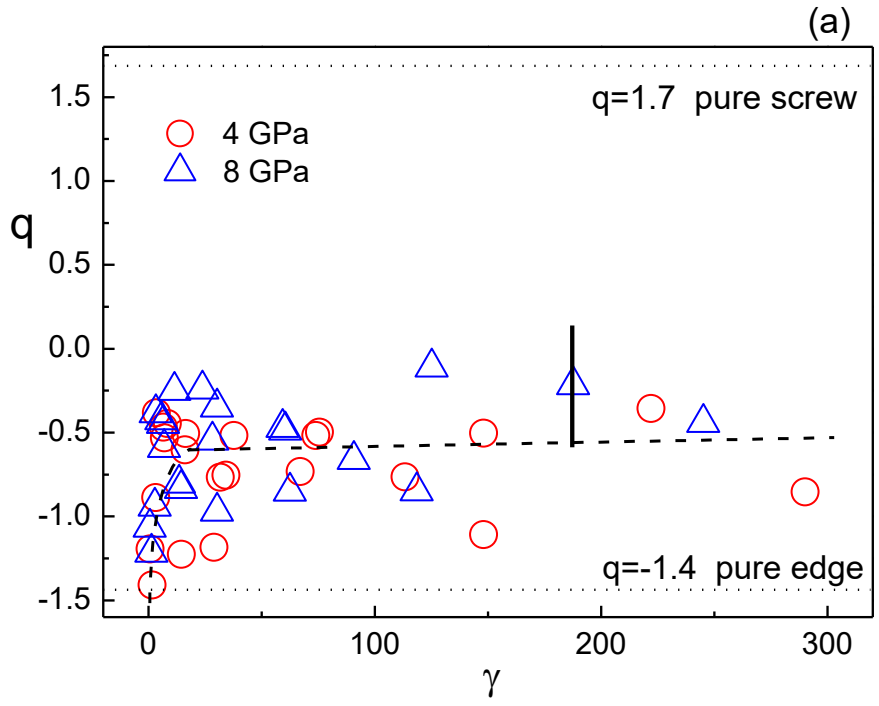

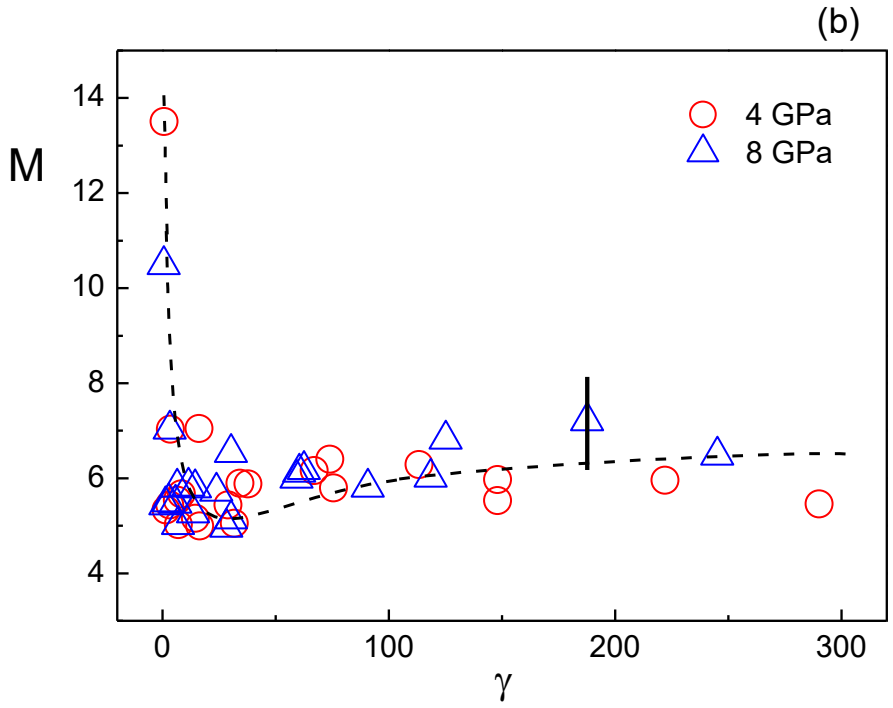

Fig. 5.6: (a) The *q* parameter, (b) the *M* parameter of the V-5Cr-5Ti specimens after deformation at 4 and 8 GPa pressures *vs*. the shear strain γ. Error bars are shown as thick vertical lines. The dotted horizontal lines in (a) indicate the q values for pure edge or screw character dislocations, respectively.

5.2.3 Thermal stability of the dislocation structure

The dislocation density, ρ, the subgrain size, d_x and the dislocation dipole character parameter, *M* in the initial state and after two high temperature annealings of the specimen HPT deformed at 4 GPa by 4 rotations are shown in Fig. 5.7. Up to 800 °C the dislocation density and the subgrain size are unchanged within the experimental error. The *M* value, however, decreases from $M = 5.8$ (±0.4) in the initial state to $M = 1.6$ (±0.2) at 800 °C indicating that the dipole character becomes stronger at heating to this temperature. With stronger dipole character the screening of strain fields is more efficient and the corresponding stored energy is smaller (Wilkens, 1969). Wilkens showed that when the *M* parameter is smaller the tails of diffraction peaks become longer (Wilkens, 1970b). Fig. 5.7b shows the intensity distributions of the 211 reflections of the specimen in the initial state (blue curve) and heated to 800 °C (red curve). In order to see the difference in the shape of the two profiles the intensities are

normalized to the maximum and the breadths to the FWHM, respectively. The tail of the annealed specimen peak is considerably longer than that of the initial specimen peak in good correlation with the theoretical calculated peak profiles shown in Fig. 2 in reference (Wilkens, 1970b). The mWH plot of the initial, the 800 and 1000 °C annealed specimens is shown in Fig. 5.7c. The slope of the FWHM values of the initial specimen is much larger than that of the 800 °C one, although the CMWP calculated dislocation densities of the two specimens are the same within experimental error. The slope in the mWH plot is proportional to the microstrain which obviously depends on both the dislocation density and the character of strain fields of dislocations (Wilkens, 1970b). In the present case, in the initial state the dipole character is considerably weaker than after annealing at 800 °C. During annealing at 800 °C the dislocation arrangement is changing while the dislocation density remains unchanged. The dipoles character increases, i.e. the strain field of dislocations becomes more of short range type. The process can be considered intermediate towards full recovery which, however, occurs only above 800 °C.

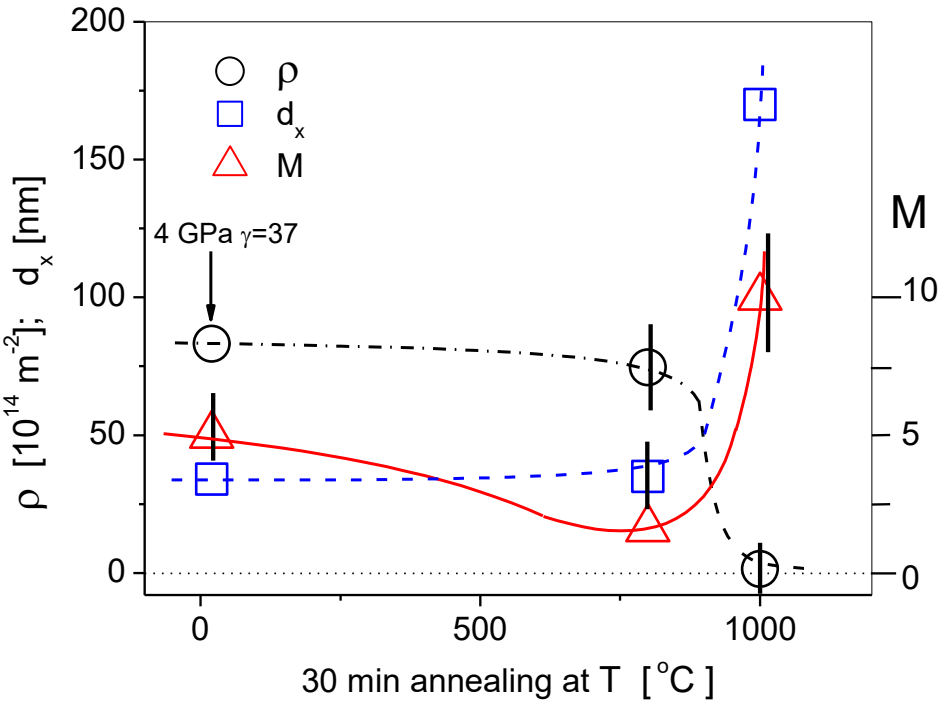

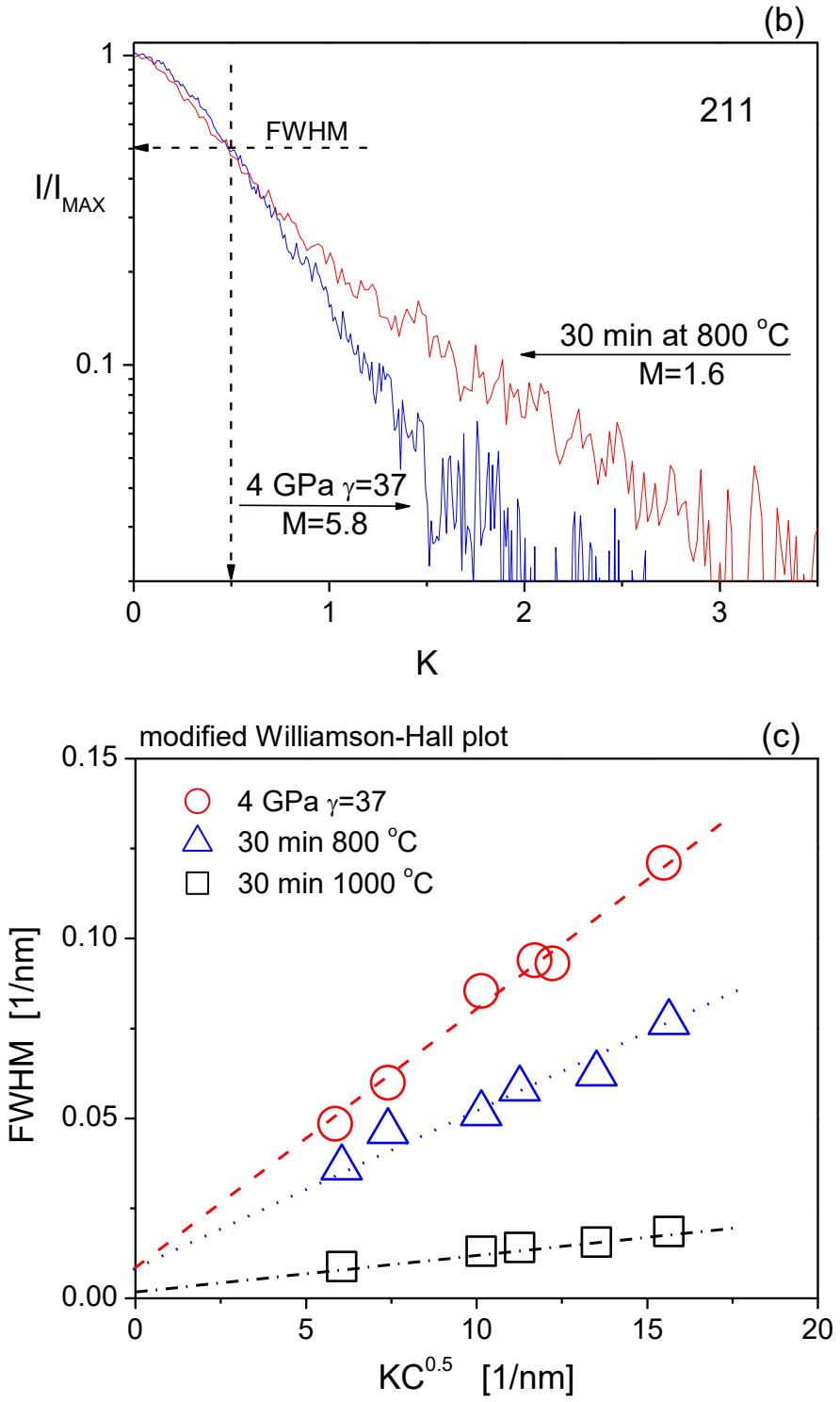

Fig. 5.7: Results of the heating experiment. (a) Dislocation density, ρ, subgrain size d_x, and the dipole character parameter, M, after 30 min holding at T. (b) Intensity distributions of the 211 reflections of the specimen in the initial state (blue curve) and after heated to 800 °C (red curve) with logarithmic intensity scale normalized to the maximum and the FWHM. (c) mWH plots of the FWHM for the same three states as in (a).

5.2.4 Correlation between the strength and microstructure

As shown in Fig. 5.5, large plastic deformation causes the simultaneous increase of the dislocation density and the reduction of crystallite size. Work hardening proceeds up to about $\gamma \cong 50$, the dislocation density increases up to about $\gamma \cong 75$ and the decrease of crystallite size stops at about $\gamma \cong 15$ as shown in Figs. 5.1b and 5.5c, respectively. This indicating that the leading mechanism in work hardening is dislocation accumulation. We correlate the flow stress with the dislocation density in Taylor's equation (Taylor, 1934):

$$\sigma = \sigma_0 + \alpha G b M_T \sqrt{\rho} \ , \tag{5.5}$$

where σ_0 is the yield stress of the coarse grain and dislocation-free material, α is a constant between zero and unity, G is the shear modulus and M_T is the Taylor factor for polycrystalline specimen. The best match between the measured and calculated flow stress values were obtained with $\sigma_0 = 523$ (±20) MPa and $\alpha = 0.20$ (±0.1) where G, b and M_T were taken as $G = 47$ GPa (Bolef et al., 1971), $b = 0.2624$ nm and $M_T = 3$. The calculated versus measured flow stress values, σ_{calc} *vs.* σ_{meas}, are shown in Fig. 5.8.

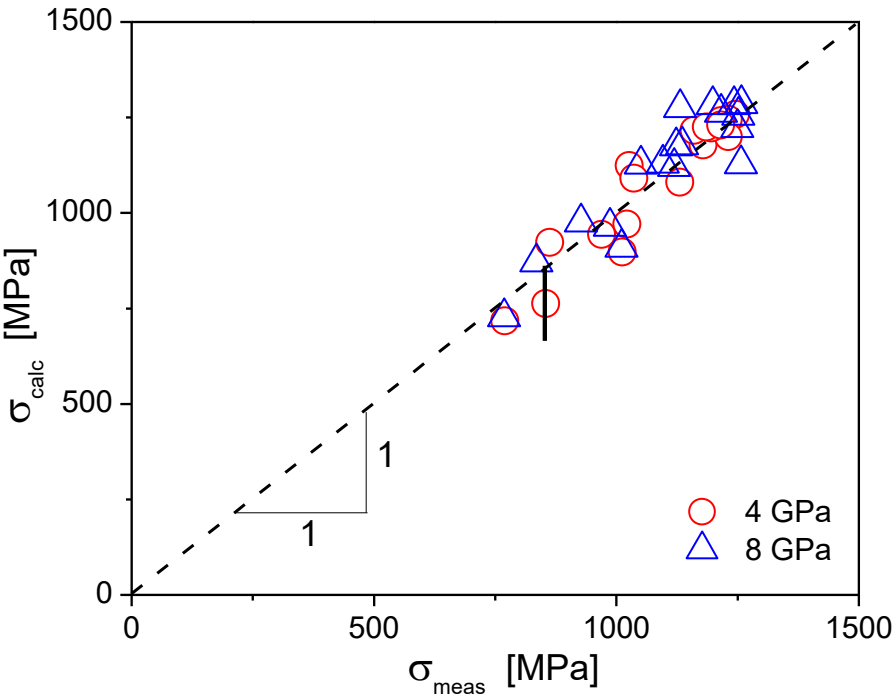

Fig. 5.8: Calculated, σ_{calc} *vs.* the measured, σ_{meas}, flow-stress values. The thick black vertical line indicates the error.

Chapter 6

Summary and Conclusions

Nuclear power, including fission and fusion energy, is more and more important in the overall energy system of the world. Currently, the electricity supply of fission reactors actually becomes indispensable, while the feasibility of fusion reactors is still on the struggling road. The service conditions in nuclear reactor are rigorous for structural materials, which should be able to endure high temperature, intense radiation, and mechanical stress. The performance of structural materials in such an extreme environment must guarantee reliable and efficient operation of reactor. Thereof, mechanical property is a critical issue for the development and application of structural materials. For this purpose, understanding the correlation between the microstructure and strength of structural materials is essentially necessary.

In this dissertation, two typical structural materials, Zr and V-5Cr-5Ti, are studied. Zirconium alloys are widely used as fuel cladding in commercial fission reactors. Vanadium alloys are regarded as promising structural materials for self-cooled lithium blanket in fusion reactors. The common roles of both materials are containing nuclear fuels and products, and meanwhile transferring released energy of nuclear reactions to the coolant. The high-resolution X-ray diffraction experiments and the CMWP procedure are applied to investigate the microstructural information of deformed Zr and V-5Cr-5Ti.

In Chapter 2, the kinematic diffraction theory and models of imperfect crystals together with the practical usage of the CMWP program are summarized. The effect of

crystalline imperfections on X-ray diffraction line profiles can be classified into size and strain broadening. The size profile is calculated using spherical crystallite shape and lognormal crystallite size distribution in most cases. The strain profile inherited from dislocations is described by the Krivoglaz-Wilkens model. The principles and steps of the CMWP procedure are presented, which is well established on the base of the defect-related physical models of line profiles.

Chapter 3 introduces nuclear materials for fission and fusion reactor, and gives a literature review about recent experiments of zirconium and vanadium alloys. In the beginning, the concepts of nuclear fission and fusion reactions are presented. The structures of fission and fusion reactors are shown respectively. Nuclear materials used in both kinds of reactors are illustrated in terms of functions. X-ray and neutron diffraction line profile analysis have been applied to determine microstructural information of zirconium alloys after heattreatment, or deformation, or irradiation. The mechanical performance and microstructure of vanadium and its alloys processed by different novel techniques have been explored.

In Chapter 4, the cold-rolled zirconium specimens were tensile-deformed along the rolling and the transverse directions. High resolution X-ray line profile analysis was used to determine the prevailing active slip-systems in the specimens with different textures. The reflections in the X-ray diffraction patterns were separated into two groups. One group corresponds to the major and the other group to the random texture component, respectively. The dislocation densities, the subgrain size and the prevailing active slip-systems were evaluated by using the CMWP procedure. These microstructure parameters were evaluated separately in the two groups of reflections corresponding to the two different texture components. The differences between the RD and TD stress-strain curves are discussed in terms of the differences of the microstructure evolution.

In Chapter 5, the microstructure and the strength of high pressure torsion processed V-5Cr-5Ti alloy were investigated by X-ray line profile analysis and microhardness testing. High pressure torsion has been applied at 4 and 8 GPa with 0.25, 0.5, 1, 2, 4 and 8 rotations. The X-ray beam of the high angular resolution diffractometer, dedicated for line profile analysis, has a footprint of about 200 μm×1.5 mm on the specimen. The diffraction patterns have been measured in the center, at half radius and close to the

edge of the specimens. This technique has provided a large number of data of the microstructure and hardness as a function of strain up to about $\gamma \cong 300$. The dislocation density and the crystallite size determined by X-ray line broadening are correlated and discussed in terms of the strength of the alloy using the Taylor equation.

The conclusion drawn from the work are:

The mechanical response was obtained to be remarkably different in RD and TD samples of cold rolled Zr. It is observed that the hardening rate and plasticity are larger in the RD than in the TD samples. At the same time, the texture of the RD samples remained unchanged, while in the TD samples the prismatic poles were gradually aligning along the loading direction during tensile deformation.

The dislocation densities and slip-system types were determined in different texture components of cold rolled Zr. An algorithm was developed to identify and sort out the diffraction peaks in diffraction patterns corresponding to the same texture components. Diffraction peaks pertinent to the same texture component, sorted out from diffraction patterns measured by changing the specimen orientations relative to the incident beam, were merged into single whole texture-specific diffraction patterns. These patterns were evaluated using the CMWP procedure to obtain texture specific microstructure parameters for textured specimens.

The dislocation densities prevailing in the RD samples increased monotonously with strain, and the fractions of slip-systems in the major and random texture components developed in a complementary manner. The well-balanced activity between the major and random texture components results in the good plasticity of the RD samples.

During the texture evolution of the TD samples, the <a>-type slip-system dominates the deformation in nearly plane strain. Once the new type of texture appeared significantly, the samples show necking and more <c+a>-type dislocations accumulate in the major texture component, apparently to accommodate the deformation.

The evolution of the dislocation density and grain size along with work hardening has been determined in the V-5Cr-5Ti alloy. High resolution X-ray diffraction and line profile analysis has been used to determine the dislocation density and subgrain size

during large deformations applied by the method of HPT and two different pressures. TEM micrographs have been used to determine the grain size and size distribution. Heating experiments were applied to determine the thermal stability of the microstructure of the alloy.

We found that work hardening proceeds up to about $\gamma \cong 50$ where it saturates at a level of about $\sigma \cong 1220$ (±40) MPa. The dislocation density was obtained to increase up to about $\gamma \cong 75$ where it saturated at a level of about $\rho \cong 82$ (±8)×10^{14} m^{-2}. The subgrain size decreases to about $d_x \cong 31$ (±2) nm at about $\gamma \cong 15$ and saturates at higher values.

The heating experiments have revealed that the dislocation density remains fairly stable up to about 800 °C. Diffraction peak shape and dislocation arrangement or dipole character analysis has shown that up to about 800 °C the dislocation line density stays constant while the dipole character becomes stronger revealing the onset of recovery process where the dislocation dipoles become narrower, however, are annealed either at a higher temperature or during longer holding times than 30 min. Our study has shown that large plastic deformation of the V-5Cr-5Ti alloy produces a strongly strained microstructure and substantial work hardening revealing a relatively good temperature stability up to about 800 °C.

Own Publications

Zhang, C., Xie, L., Fan, Z., Wang, H., Chen, X., Li, J. and Sun, G., Straightforward understanding of the structures of metastable α″ and possible ordered phases in uranium-niobium alloys from crystallographic simulation, *J. Alloys Compd.*, **648**, 389-396 (2015)

Li, H., Cai, W., Fan, Z., Huang, X., Wang, Y., Gong, J., Chen, B., Sun, G., Wang, H., Li, J. and Peng, S., Compression deformation behavior of zircaloy-4 alloy changing with activated twinning type at ambient temperature: experiment and modeling. *J. Appl. Cryst.*, **49**, 987–996 (2016).

Yan, G., Tian, Q., Liu, J., Fan, Z., Sun, G., Zhang, C., Wang, Y., Chen, B., Gong, J., Zhou, X., Yang, Z., Nie, F., Li, J. and Li, X., The microstructural evolution in HMX based plastic-bonded explosive during heating and cooling process: an in situ small-angle scattering study, *Cent. Eur. J. Energ. Mater.*, **13(4)**, 916-926 (2016)

Yan, G., Fan, Z., Huang, S., Liu, J., Wang, Y., Tian, Q., Bai, L., Gong, J., Sun, G. and Wang, X., Phase re-transformation and void evolution of previously heated HMX-based plastic-bonded explosive in wet air, *J. Phys. Chem. C*, **121(37)**, 20426–20432 (2017)

Peng, L., Li, X., Fan, Z., Jiang, C., Zhou, P. and Lai, X., A quasi-in-situ EBSD observation of the transformation from rolling texture to recrystallization texture in V-4Cr-4Ti alloy, *Mater. Charact.*, **126**, 35-41 (2017)

Sun, C, Hai, X., Xi, S., Fan, Z., Li, P. and Wang, W., New insights of solid-state alloying and amorphous-nanocrystalline cyclic phase transitions during Cr-40wt.%Mo powder milling, *J. Alloys Compd.*, **731**, 667-677 (2018)

Fan, Z., Jóni, B., Xie, L., Ribárik, G. and Ungár, T., Dislocation structure in textured zirconium tensile-deformed along rolling and transverse directions determined by X-ray diffraction line profile analysis, *J. Nucl. Mater.*, **502**, 301-310 (2018)

Fan, Z., Jóni, B., Ribárik, G., Ódor, É., Fogarassy, Zs. and Ungár, T., The microstructure and strength of a V-5Cr-5Ti alloy processed by high pressure torsion, *Mater. Sci. Eng. A*, **758**, 139-146 (2019)

Fan, Z., Song, Z., Jóni, B., Ribárik, G. and Ungár, T., Investigation of dislocation structure in Cu compressed at different strain rates by X-ray line profile analysis, *in preparation* (2019)

Bibliography

[1] Abdolvand, H., Majkut, M., Oddershede, J. and Wright, J. P., *Acta Mater.*, **93**, 246-255 (2015)

[2] Ahmmed, K. F., Balogh, L., Idrees, Y., Yu, H., Long, F. and Daymond, M. R., *J. Appl. Cryst.*, **49**, 1609-1623 (2016)

[3] Allen, T. R., Konings, R. J. M. and Motta, A. T., *Corrosion of Zirconium Alloys*, Comprehensive Nuclear Materials, edited by Konings, R. J. M., Allen, T. R., Stoller, R. E. and Yamanaka, S., Vol. 5, pp. 49-68, Elsevier, Amsterdam (2012)

[4] Alvarez, M. A. V., Santisteban, J. R., Domizzi, G. and Almer, J., *Acta Mater.*, **59**, 2210-2220 (2011)

[5] Alvarez, M. A. V., Santisteban, J. R., Vizcaino, P., Flores, A. V., Banchik, A. D. and Almer, J., *Acta Mater.*, **60**, 6892-6906 (2012)

[6] Balogh, L., Brown, D. W., Mosbrucker, P., Long, F. and Daymond, M. R., *Acta Mater.*, **60**, 5567-5577 (2012)

[7] Balogh, L., Ribárik, G. and Ungár, T., *J. Appl. Phys.*, **100**, 023512 (2006)

[8] Balogh, L., Tichy, G. and Ungár, T., *J. Appl. Cryst.*, **42**, 580-591 (2009)

[9] Becker, K., *Z. Phys.*, **42**, 226-245 (1927)

[10] Bertaut, F. C. R., *Acad. Sci. Paris*, **228**, 187-189 (1949)

[11] Beyerlein, I. J. and Tomé, C. N., *Int. J. Plast.*, **24**, 867-895 (2008)

[12] Bolef, D. I., Smith, R. E. and Miller, J. G., *Phy. Rev. B*, **15**, 4100-4108 (1971)

[13] Borbély, A., Dragomir, I. C., Ribárik, G. and Ungár, T., *J. Appl. Cryst.*, **36**, 160-162 (2003)

[14] Borbély, A. and Ungár, T., *C. R. Physique*, **13**, 293-306 (2012)

[15] Bourke, M. A. M., Dunand, D. C. and Ustündag, E., *Appl. Phys. A*, **74**, s1707-s1709 (2002)

[16] Cai, M., Zhang, J., Niu, L. and Shi, H., *Scripta Mater.*, **62**, 524-527 (2010)

[17] Castelnau, O., Francillette, H., Bacroix, B. and Lebensohn, R. A., *J. Nucl. Mater.*, **297**, 14-26 (2001)

[18] Chen, J., Muroga, T., Nagasaka, T., Qiu, S., Li, C., Chen, Y., Liang, B. and Xu, Z., *Fusion Eng. Des.*, **81**, 2899-2905 (2006)

[19] Chen, J., Nagasaka, T., Muroga, T., Qiu, S., Li, C. and Nita, N., *J. Nucl. Mater.*, **374**, 298-303 (2008)

[20] Chun, Y. B., Ahn, S. H., Shin, D. H. and Hwang, S. K., *Mater. Sci. Eng. A*, **508**, 253-258 (2009)

[21] Chun, Y. B., Ahn, S. H., Shin, D. H. and Hwang, S. K. *Mater. Sci. Forum*, **638-642**, 1934-1939 (2010)

[22] Csiszár, G., Pantleon, K., Alimadadi, H., Ribárik, G. and Ungár, T., *J. Appl. Cryst.*, **45**, 61-70 (2012)

[23] Collum, B., *Nuclear Facilities*, Woodhead Publishing, Cambridge (2017)

[24] Cordier, P., Ungár, T., Zsoldos, L. and Tichy, G., *Nature*, **428**, 837–840 (2004)

[25] De Sanctis, E., Monti, S. and Ripani, M., *Energy from Nuclear Fission*, Springer International Publishing, Switzerland (2016)

[26] Ding, J., Yang, S., Zhu, B., Li, Q., Long, Y. and Wan, F., *Fusion Eng. Des.*, **125**, 407-414 (2017)

[27] Ditenberg, I. A., Grinyaev, K. V., Tyumentsev, A. N., Chernov, V. M. and E. V. Chulkov, *Russ. Phys. J.*, **55**, 223-228 (2012)

[28] Ditenberg, I. A. and Tyumentsev, A. N., *AIP Conf. Proc.*, **1683**, 020043 (2015)

[29] Ditenberg, I. A. and Tyumentsev, A. N., *Russ. Phys. J.*, **60**, 1993-1999 (2018)

[30] Ditenberg, I. A., Tyumentsev, A. N., Grinyaev, K. V., Chernov, V. M., Potapenkoc, M. M. and Drobyshevc, V. A., *Inorg. Mater.: Appl. Res.*, **4**, 438-443 (2013)

[31] Ditenberg, I. A., Tyumentsev, A. N., Grinyaev, K. V., Chernov, V. M., Potapenkoc, M. M. and Korznikov, A. V., *Tech. Phys.*, **56**, 815-820, (2011)

[32] Ditenberg, I. A., Tyumentsev, A. N., Korznikov, A. V., Chernov, V. M. and Potapenkoc, M. M., *Phys. Met. Metallogr.*, **113**, 160-169 (2012)

[33] Dragomir, I. C. and Ungár, T., *J. Appl. Crystallogr.*, **35**, 556-564 (2002a)

[34] Dragomir, I. C. and Ungár, T., *Powder Diffr.*, **17**, 104-111 (2002b)

[35] Dunlop, J. W., Brechet, Y. J. M., Legras, L. and Estrin, Y., *Mater. Sci. Eng. A*, **443**, 77-86 (2007)

[36] Engler, O. and Randle, V., *Introduction to Texture Analysis: Macrotexture, Micro-texture & Orientation Mapping*, CRC Press, Boca Raton (2010)

[37] Farrell, K., Byun, T. S. and Hashimoto, N., *J. Nucl. Mater.*, **335**, 471-486 (2004)

[38] Fu, H., Chen, J., Zheng, P., Nagasaka, T., Muroga, T., Li, Z., Cui, S., and Xu, Z., *J. Nucl. Mater.*, **442**, S336-S340 (2013)

[39] Fukumoto, K., Kuroyanagi, Y., Kuroiwa, H., Narui, M. and Matsui, H., *J. Nucl. Mater.*, **417**, 295-298 (2011)

[40] Fukumoto, K., Narui, M., Matsui, H., Nagasaka, T., Muroga, T., Li, M., Hoelzer, D. T. and Zinkle, S. J., *J. Nucl. Mater.*, **386**, 575-578 (2009)

[41] Furuno, T., Kurishita, H., Nagasaka, T., Nishimura, A., Muroga, T., Sakamoto, T., Kobayashi, S., Nakai, K., Matsuo, S. and Arakawa, H., *J. Nucl. Mater.*, **417**, 299-302 (2011)

[42] Gao, J., Du, Y., Ohnuki, S. and Wan, F., *J. Nucl. Mater.*, **481**, 81-87 (2016)

[43] Gelles, D. S., Rice, P. M., Zinkle, S. J. and Chung, H. M, *J. Nucl. Mater.*, **258-263**, 1380-1385 (1998)

[44] Gloaguen, D., Fajoui, J. and Girault, B., *Acta Mater.*, **71**, 136-144 (2014)

[45] Grinyaev, K. V., Smirnov, I. V., Ditenberg, I. A., Tyumentsev, A. N., Radishevsky, V. L., Gavrilin, A. N., Korznikov, A. V. and Chernov, V. M., *Russ. Phys. J.*, **59**, 2094-2100 (2017)

[46] Grinyaev, K. V., Smirnov, I. V., Radishevsky, V. L., Ditenberg, I. A., Tyumentsev, A. N., Chernov, V. M. and Korznikov, A. V., *AIP Conf. Proc.*, **1783**, 020066 (2016)

[47] Groma, I., *Phys. Rev. B*, **57**, 7535–7542 (1998)

[48] Groma, I., Ungár, T. and Wilkens, M. *J. Appl. Crystallogr.*, **21**, 47-54 (1988)

[49] Grossbeck, M. L., *Effect of Radiation on Strength and Ductility of Metals and Alloys*, Comprehensive Nuclear Materials, edited by Konings, R. J. M., Allen, T. R., Stoller, R. E. and Yamanaka, S., Vol. 1, pp. 99-122, Elsevier, Amsterdam (2012)

[50] Gubicza, J., Kassemc, M., Ribárik, G. and Ungár, T., *Mater. Sci. Eng. A*, **372**, 115-122 (2004)

[51] Guinier, A., *X-ray diffraction*, Freeman and Co., San Francisco, CA (1963)

[52] Gui, L., and Liu, Y., *Comp. Cond. Matter*, **7**, 7-13 (2016)

[53] Gurao, N. P., Akhiani, H. and Szpunar, J. A., *J. Nucl. Mater.*, **453**, 158-168 (2014)

[54] Hahn, O. and Strassmann, F., *Naturwissenschaften*, **27**, 11-15 (1939)

[55] Hielscher, R. and Schaeben, H., *J. Appl. Crystallogr.*, **41**, 1024-1037 (2008)

[56] Himbeault, D. D., Chow, C. K. and Puls, M. P., *Metall. Mater. Trans. A*, **25**, 135-145 (1994)

[57] Hinds, W. C., *Aerosol Technology: Properties, Behavior and Measurement of*

Airbone Particles, Wiley, New York (1982)

[58] Hoffelner, W., *Materials for Nuclear Plants*, Springer, London (2013)

[59] Hohenwarter, A. and Wurster, S., *Mater. Sci. Eng. A*, **650**, 492-496 (2016)

[60] Holden, T. M., Root, J. H., Holt, R. A. and Turner, P. A., *J. Nucl. Mater.*, **304**, 73-82 (2002)

[61] Holden, T. M., Suzuki, H., Carr, D. G., Ripley, M. I. and Clausen, B., *Mater. Sci. Eng. A*, **437**, 33-37 (2006)

[62] Huang, Y., Lemang, M., Zhang, X., Pereira, P. H. R. and Langdon, T. G., *Mater. Sci. Eng. A*, **655**, 60–69 (2016)

[63] Jiang, Z. Z., Yu, S. H., Chun, Y. B., Shin, D. H. and Hwang, S. K. *Mater. Sci. Eng. A*, **479**, 285-292 (2008)

[64] Jóni, B., Schafler, E., Zehetbauer, M., Tichy, G. and Ungár, T., *Acta Mater.*, **61**, 632-642 (2013)

[65] Kikuchi, M., Lackner, K. and Tran, M. Q., *Fusion Physics*, International Atomic Energy Agency, Vienna (2012)

[66] Krill, C. E. and Birringer, R., *Philos. Mag. A*, **77**, 621-640 (1998)

[67] Krivoglaz, M. A., *Theory of X-ray and Thermal Neutron Scattering by Real Crystals*, Springer-Verlag, Berlin (1996)

[68] Krivoglaz, M. A. and Ryaboshapka, K. P., *Fizika Metall.*, **15**, 18-31 (1963)

[69] Kurishita, H., Kuwabara, T. and Hasegawa, M., *Mater. Sci. Eng. A*, **432**, 245-252 (2006a)

[70] Kurishita, H., Kuwabara, T. and Hasegawa, M., *Mater. Sci. Eng. A*, **433**, 32-38 (2006b)

[71] Kurishita, H., Oda, S., Kobayashi, S., Nakai, K., Kuwabara, T., Hasegawa, M. and Matsui., H., *J. Nucl. Mater.*, **367**, 848-852 (2007)

[72] Kuwabara, T., Kurishita, H. and Hasegawa, M. *Mater. Sci. Eng. A*, **417**, 16-23 (2006)

[73] Langford, J. I., Louër, D. and Scardi, P., *J. Appl. Cryst.*, **33**, 964–974 (2000)

[74] Langford, J. I. and Wilson, A. J. C., *J. Appl. Cryst.*, **11**, 102–113 (1978)

[75] Lee, S., Edalati, K. and Horita, Z., *Mater. Trans.*, **51**, 1072-1079 (2010)

[76] Lemaignan, C., *Zirconium Alloys: Properties and Characteristics*, Comprehensive Nuclear Materials, edited by Konings, R. J. M., Allen, T. R., Stoller, R. E. and Yamanaka, S., Vol. 2, pp. 217-232, Elsevier, Amsterdam (2012)

[77] Lemaignan, C. and Motta, A. T., *Zirconium alloys in nuclear applications*,

Materials Science and Technology, edited by Cahn, R.W., Haasen, P., Kramer, E. J. and Forst, B. R. T., 10B, pp. 1-51, VCH, Weinheim (1994)

[78] Li, H., Cai, W., Fan, Z., Huang, X., Wang, Y., Gong, J., Chen, B., Sun, G., Wang, H., Li, J. and Peng, S., *J. Appl. Crystallogr.*, **49**, 987-996 (2016)

[79] Li, Y., Dong, P., Li, R., Yang, J. and Xie, J., *J. Nucl. Mater.*, **421**, 9-14 (2012)

[80] Li, Y., Wang, Z., Zhang, L., Luo, C. and Lai, X., *T. Nonferr. Metal. Soc.*, **25**, 1889-1900 (2015)

[81] Li, Z., Li, Q., Li, Y., Lin, C., Cui, S. and Ma, T., *Fusion Eng. Des.*, **114**, 76-83 (2017)

[82] Long, F., Balogh, L., Brown, D. W., Mosbrucker, P., Skippon, T., Judge, C. D. and Daymond, M. R., *Acta Mater.*, **102**, 352-363 (2016)

[83] Lowe, T. C. and Valiev, R. Z., JOM, **56**, 64-68 (2004)

[84] Luton, M. J. and Jonas, J. J., *Can. Metall. Ouart.*, **11**, 79-90 (1972)

[85] Mac Ewen, S. R., Ells, C. E. and Woo, O. T., *J. Nucl. Mater.*, **101**, 336-349 (1981)

[86] Máthis, K., Nyilas, K., Axt, A., Dragomir-Cernatescu, I., Ungár, T. and Lukáč, P., *Acta Mater.*, **52**, 2889-2894 (2004)

[87] Matsui, H., Fukumoto, K., Smith, D. L., Chung, H. M., Witzenburg, W. V. and Votinov, S. N., *J. Nucl. Mater.*, **233-237**, 92-99 (1996)

[88] McCabe, R. J., Cerreta, E. K., Misra, A., Kaschner, G. C. and Tome, C. N., *Philos. Mag. A*, **86**, 3595-3611 (2006)

[89] Meitner, L. and Frisch, O. R., *Nature*, **143,** 239-240 (1939)

[90] Mughrabi, H., *Curr. Opin. Solid State Mater. Sci.*, **20**, 411-420 (2016)

[91] Mughrabi, H., *Mater. Sci. Eng.*, **85**, 15-31 (1987)

[92] Muroga, T., *Vanadium for nuclear systems*, Comprehensive Nuclear Materials, edited by Konings, R. J. M., Allen, T. R., Stoller, R. E. and Yamanaka, S., Vol. 4, pp. 391-406, Elsevier, Amsterdam (2012)

[93] Muroga, T., Chen, J., Chernov, V. M., Kurtz, R. J. and Le Flem, M., *J. Nucl. Mater.*, **455**, 263-268 (2014)

[94] Muroga, T., Nagasaka, T., Abe, K., Chernov, V. M., Matsui, H., Smith, D. L., Xu, Z. and Zinkle, S. J., *J. Nucl. Mater.*, **307**, 547-554 (2002)

[95] Najmabadi, F. and The ARIES Team, *Fusion Eng. Des.*, **80**, 3-23 (2006)

[96] Onimus, F. and Béchade, J. L., *Radiation effects in zirconium alloys*, Comprehensive Nuclear Materials, edited by Konings, R. J. M., Allen, T. R., Stoller, R. E. and Yamanaka, S., Vol. 4, pp. 1-31, Elsevier, Amsterdam (2012)

[97] Onimus, F., Monnet, I., Béchade, J. L., Prioul, C. and Pilvin, P., *J. Nucl. Mater.*, **328**, 165-179 (2004)

[98] Partridge, P. G., *Metall. Rev.*, **12**, 169-194 (1967)

[99] Pippan, R., *High-pressure torsion – features and applications*, Bulk Nano-structured Materials, edited by Zehetbauer, M. J. and Zhu Y., pp. 217-233, WILEY-VCH, Weinheim (2009)

[100] Prakash, D. G. L., Preuss, M., Dahlbäck, M. and Quinta da Fonseca, J., *Acta Mater.*, **88** 389-401 (2015)

[101] Qu, F., Dong, X., Liu, J., Chen, D., Wang, Z. and Zhou, J., *Int. J. Refract. Met. H.*, **72**, 349-366 (2018)

[102] Qu, F., Reng, Z., Ma, R., Wang, Z. and Chen, D., *J. Alloy. Compd.*, **663**, 552-559 (2016)

[103] Ribárik, G., *Ph. D. thesis*, Eötvos Loránd University, Budapest, Hungary (2008)

[104] Ribárik, G., Gubicza, J. and Ungár, T., *Mater. Sci. Eng. A*, **387-389**, 343-347 (2004)

[105] Ribárik, G., Jóni, B. and Ungár, T., *J. Mater. Sci. Technol.*, **35**, 1508-1514 (2019)

[106] Ribárik, G. and Ungár, T., *Mater. Sci. Eng. A*, **528**, 112-121 (2010)

[107] Ribárik, G., Ungár, T. and Gubicza, J., *J. Appl. Cryst.*, **34**, 669–676 (2001)

[108] Rice, P. M. and Zinkle, S. J., *J. Nucl. Mater.*, **258-263**, 1414-1419 (1998)

[109] Richert, J. and Richert, M., *Aluminium*, **62**, 604-607 (1986)

[110] Saito, Y., Tsuji, N., Utsunomiya, H., Sakai, T. and Hong, R. G., *Scripta Mater.*, **39**, 1221-1227 1998

[111] Sakamoto, T., Kurishita, H., Furuno, T., Nagasaka, T., Kobayashi, S., Nakai, K., Matsuo, S., Arakawa, H., Nishimura, A. and Muroga, T., *Mater. Sci. Eng. A*, **528**, 7843-7850 (2011)

[112] Salishchev, G. A., Valiahmetov, O. R. and Galeev, R. M., *J. Mater. Sci.*, **28**, 2898-2902 1993

[113] Santisteban, J. R., Vicente-Alvarez, M. A., Vizcaíno, P., Banchik, A. D. and Almer, J. D., *Acta Mater.*, **58**, 6609-6618 (2010)

[114] Satou, M., Chuto, T. and Abe, K., *J. Nucl. Mater.*, **283-287**, 367-371 (2000)

[115] Scardi, P. and Leoni, M., *Acta Cryst. A*, **58**, 190–200 (2002)

[116] Schafler, E., *Scripta Mater.*, **62**, 423-426 (2010)

[117] Scherrer, P., *Nachr. Ges. Wiss. Göettingen*, **26**, 98-100 (1918)

[118] Seymour, T., Frankel, P., Balogh, L., Ungár, T., Thompson, S. P., Jädernäs, D., Romero, J., Hallstadius, L., Daymond, M. R., Ribárik, G. and Preuss, M., *Acta*

Mater., **126**, 102-113 (2017)

[119] Shultis, J. K. and Faw, R. E., *Fundamentals of nuclear science and engineering*, CRC Press, Boca Raton (2002)

[120] Singh, J., Mahesh, S., Kumar, G., Pant, P., Srivastava, D., Dey, G. K., Saibaba, N. and Samajdar, I., *Metall. Mater. Trans. A*, **46**, 1927-1947 (2015)

[121] Skrotzki, W., Eschke, A., Jóni, B., Ungár, T., Toth, L. S., Ivanisenko, Yu. and Kurmanaeva, L., *Acta Mater.*, **61**, 7271-7284 (2013)

[122] Smirnov, I. V., Grinyaev, K. V., Ditenberg, I. A., Tyumentsev, A. N., Chernov, V. M. and Korznikov, A. V., *AIP Conf. Proc.*, **1783**, 020211 (2016)

[123] Stolyarov, V. V., Zhu, Y., Alexandrov, I. V., Lowe, T. C. and Valiev, R. Z., *Mater. Sci. Eng. A*, **343**, 43-50 (2003)

[124] Taylor, G. I., *Proc. Roy. Soc. A*, **145**, 362-404 (1934)

[125] Tenckhoff, E., *Deformation mechanisms, texture, and anisotropy in zirconium and Zircaloy*, Special Technical Publication, Philadelphia, PA (1988)

[126] Tenckhoff, E. and Rittenhouse, P. L., *J. Nucl. Mater.*, **35**, 14-23 (1970)

[127] Tsisar, V., Nagasaka, T., Flem, M. L., Yeliseyeva, O., Konys, J. and Muroga, T., *Fusion Eng. Des.*, **89**, 1633-1636 (2014)

[128] Tsisar, V., Nagasaka, T., Flem, M. L., Yeliseyeva, O., Konys, J. and Muroga, T., *Nucl. Mater. Eng.*, **9**, 436-440 (2016)

[129] Tomé, C. N., Christodoulou, N., Turner, P. A., Miller, M. A., Woo, C. H., Root, J. and Holden, T. M., *J. Nucl. Mater.*, **227**, 237-250 (1996)

[130] Topping, M., Ungár, T., Race, C. P., Harte, A., Garner, A., Baxter, F., Dumbill, S., Frankel, P. and Preuss, M., *Acta Mater.*, **145**, 255-263 (2018)

[131] Toth, L. S. and Gu, C., *Mater. Charact.*, **92**, 1-14 (2014)

[132] Trojanova, Z., Lukac, P., Dlouhy, A. and Heinitz, H. J., *Czech. J. Phys.*, **35**, 298-301 (1985)

[133] Turner, P. A., Christodoulou, N. and Tomé, C. N., *Int. J. Plast.*, **11**, 251-265 (1995)

[134] Tyumentsev, A. N., Ditenberg, I. A., Grinyaev, K. V., Chernov, V. M. and Potapenko, M. M. *J. Nucl. Mater.*, **413**, 103-106 (2011)

[135] Tyumentsev, A. N., Ditenberg, I. A., Grinyaev, K. V., Smirnov, I. V., Pinzhin, Yu. P., Chernov, V. M., Potapenko, M. M., Drobyshev, V. A. and Kravtsova, M. V., *Phys. Atom. Nucl.*, **78**, 1092-1099 (2015)

[136] Tyumentsev, A. N., Korotaev, A. D., Pinzhin, Y. P., Ditenberg, I. A., Litovchenko, S. V., Shuba, Y. V., Shevchenko, N. V., Drobishev, V. A., Potapenko and M. M.,

Chernov, V. M., *J. Nucl. Mater.*, **329**, 429-433 (2004)

[137] Ungár, T. and Borbély, A., *Appl. Phys. Lett.*, **69**, 3173-3175 (1996)

[138] Ungár, T., Castelnau, O., Ribárik, G., Drakopoulos, M., Béchade, J. L., Chauveau, T., Snigirev, A., Snigireva, I., Schroer, C. and Bacroix, B., *Acta Mater.*, **55**, 1117-1127, (2007)

[139] Ungár, T., Dragomir, I. C., Révész, Á. and Borbély, A., *J. Appl. Cryst.*, **32**, 992-1002 (1999)

[140] Ungár, T., Gubicza, J., Ribárik, G. and Borbély, A., *J. Appl. Cryst.*, **34**, 298-310 (2001)

[141] Ungár, T., Holden, T. M., Jóni, B., Clausen, B., Balogh, L., Csiszár, G. and Brown, D. W., *J. Appl. Crystallogr.*, **48**, 409-417 (2015)

[142] Ungár, T., Ott, S., Sanders, P. G., Borbély, A. and Weertman, J. R., *Acta Mater.*, **46**, 3693-3699 (1998)

[143] Ungár, T., Ribárik, G. and Balogh, L., *Met. Mater. Transact. A*, **41**, 1202-1209 (2010)

[144] Ungár, T. and Tichy, G., *Phys. Status Solidi A*, **171**, 425–434 (1999)

[145] Ungár, T., Tichy, G., Gubicza, J. and Hellmig, R. J., *Powder Diffr.*, **20**, 366-375 (2005)

[146] Valiev, R. Z., Estrin, Y., Horita, Z., Langdon, T. G., Zehetbauer, M. J. and Zhu, Y., *JOM*, **58**, 33-39 (2006)

[147] Valiev, R. Z., Islamgaliev, R. K. and Alexandrov, I. V., *Prog. Mater. Sci.*, **45**, 103-189, (2000)

[148] Valiev, R. Z. and Langdon, T. G., *Prog. Mater. Sci.*, **51**, 881-981 (2006)

[149] Wang, Z., Zhao, Q., Wei, Y., Liu, P., Yang, S., Wan, F. and Zhan, Q., *J. Alloy. Compd.*, **732**, 406-413 (2018)

[150] Warner E. S. and Heath G. A., *J. Ind. Ecol.*, **16**, S73–S92 (2012)

[151] Warren, B. E., *Progr. Metal Phys.*, **8**, 147–202 (1959)

[152] Warren, B. E., *X-ray Diffraction*, Reading, Addison-Wesley, MA (1969)

[153] Warren, B. E. and Averbach, B. L., *J. Appl. Phys.*, **21**, 595–598 (1950)

[154] Whittle, K., *Nuclear Materials Science*, IOP Publishing, Bristol (2016)

[155] Wilkens, M., *Acta Metall.*, **17**, 1155-1159 (1969)

[156] Wilkens, M., *Phys. Status Solidi A*, **2**, 359-370 (1970b)

[157] Wilkens, M., *Theoretical aspects of kinematical X-ray diffraction profiles from crystals containing dislocation distributions*, Fundamental Aspects of Dislocation

Theory, edited by J. A. Simmons, R. de Wit and R. Bullough., Vol. II, pp. 1195-1221, Nat. Bur. Stand. (US) Spec. Publ. No. 317., Washington, DC, USA (1970a)

[158] Wilkens, M., Herz, K. and Mughrabi, H., *Z. Metallkde.*, **71**, 376-384 (1980)

[159] Williamson, G. K. and Hall, W. H., *Acta Metall.*, **1**, 22-31 (1953)

[160] Wurster, S. and Pippan, R., *Scripta Mater.*, **60**, 1083-1087 (2009)

[161] Xu, F., Holt, R. A., Daymond, M. R., Rogge, R. B. and Oliver, E. C., *Mater. Sci. Eng. A*, **488**, 172-185 (2008)

[162] Zheng, P., Chen, J., Nagasaka, T., Muroga, T., Zhao, J., Xu, Z., Li, C., Fu, H., Chen, H. and Duan, X., *J. Nucl. Mater.*, **455**, 669-675 (2014a)

[163] Zheng, P., Nagasaka, T., Muroga, T. and Chen, J., *Fusion Eng. Des.*, **89**, 1648-1652 (2014b)

[164] Zheng, P., Nagasaka, T., Muroga, T. and Chen, J., *J. Nucl. Mater.*, **442**, S330-S335 (2013)

[165] Zheng, P., Nagasaka, T., Muroga, T., Chen, J. and Li, Y., *Fusion Eng. Des.*, **86**, 2561-2564 (2011)

[166] Zhilyaev, A. P. and Langdon, T. G., *Prog. Mater. Sci.*, **53**, 893-979 (2008)

[167] Zhilyaev, A. P., Lee, S., Nurislamova, G. V., Valiev, R. Z. and Langdon, T. G., *Scripta Mater.*, **44**, 2753-2758 (2001)

[168] Zhilyaev, A. P., Nurislamova, G. V., Kim, B. K., Baró, M. D., Szpunar, J. A. and Langdon, T. G., *Acta Mater.*, **51**, 753-765 (2003)

[169] Zhu, B., Yang, S., Ding, J., Zhang, W., Long, Y., and Wan, F., *Fusion Eng. Des.*, **100**, 171-176 (2015)

[170] Zinkle, S. J., Matsui, H., Smith, D. L., Rowcliffe, A. F., Osch, E. V., Abe, K. and Kazakov, V. A., *J. Nucl. Mater.*, **258-263**, 205–214 (1998)

Appendix

A.1 Microstructure of a neutron irradiated Zr-4 alloy

The specimens were machined from a commercial cold-rolled Zr-4 plate. The nominal composition of Zr-4 alloy is 1.45 Sn, 0.21 Fe, 0.1 Cr, 0.125 O and balance Zr in wt %. The macrotexture of the specimens was measured using a Bruker D8 Discover X-ray diffractometer. The procedure of the measurement is described in Section 4.1.2. The texture of the Zr-4 specimens is of typical rolling texture, which is similar to the case of the initial pure Zr specimen in Chapter 4. The {0002} planes are inclined about ±35^{o} from ND toward TD, and the [01$\bar{1}$0] direction is parallel to RD.

Zr-4 alloy is widely used as cladding materials in pressurized water reactors. In order to investigate irradiation damages in Zr-4 alloy, one square plate of neutron irradiated specimen was prepared. The fluence of the specimen is 3×10^{23} n/m^2 (E > 0.1 MeV). The length and the thickness of the specimen are about 10 and 0.4 mm, respectively. Since neutron activated Zr-4 alloy can emit γ rays, it will increase the background level in X-ray diffraction measurement. The specimen was later cut into a smaller rectangular plate with 4 mm length and 3 mm width. Fig. A.1 shows the diffraction patterns of the irradiated specimens of two different dimensions. The X-ray incident angle is 25^{o} on the sample surfaces parallel to the RD-TD plane. According to the comparison, it can be found that reducing the sample size is helpful to improve the signal-to-noise ratio of diffraction pattern. Therefore, the diffraction pattern of the smaller dimension specimen will be used for the evaluation.

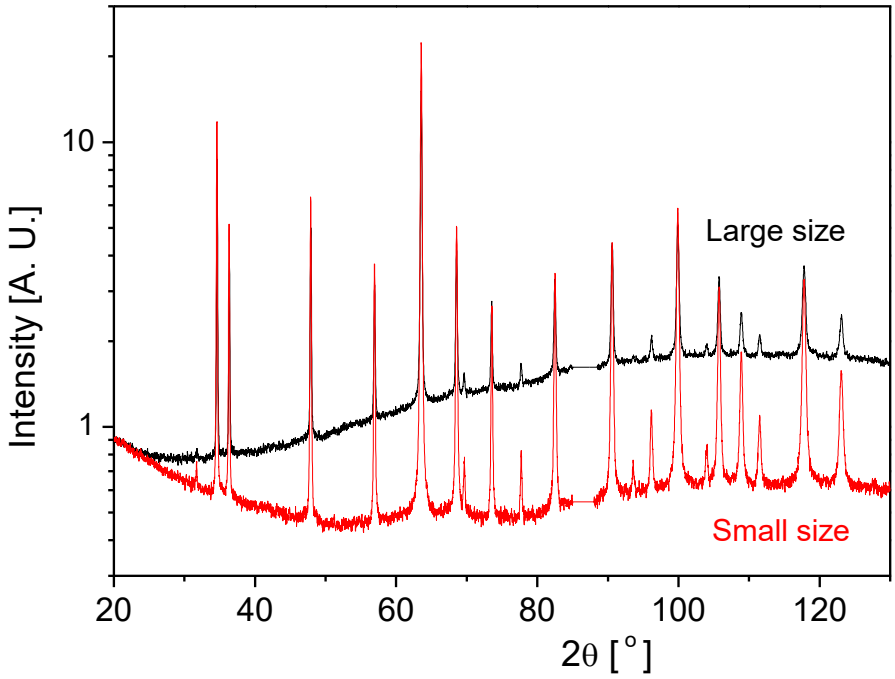

Fig. A.1: Diffraction patterns of the Zr-4 specimens with two different sizes measured on the sample surface parallel to the RD-TD plane at the incident angle 25°.

In order to select suitable rotation angles of the specimen, the calculation in Section 4.1.4 was carried out. The incident angle 25° was adopted to measure high-resolution diffraction patterns on the ND-TD and the RD-TD sample surfaces, respectively. The reflections belonging to the major texture component were selected to construct a whole diffraction pattern. The whole diffraction pattern was then evaluated using the CMWP procedure to obtain microstructure parameters in the specimen. The measured and calculated patterns of the irradiated Zr-4 specimen are shown in Fig. A.2. As a benchmark, the diffraction pattern of the unirradiated Zr-4 specimen was also measured and evaluated. Table A.1 lists the area average crystallite size, d_{area}, the dislocation densities, ρ, the fractions of slip-system types, $h_{<a>}$ and $h_{<c+a>}$ and the dislocation arrangement parameter M for the unirradiated and irradiated Zr-4 specimens. The CMWP results show the dislocation density of the irradiated Zr-4 specimen is unchanged compared to that of the irradiated Zr-4 specimen. This can also be confirmed from the mWH plots of the Zr-4 specimens (see Fig. A.3). The slopes of the FWHM values are nearly the same for the unirradiated and irradiated samples. It indicates qualitatively neutron irradiation at such a fluence hardly affect the dislocation density in the sample.

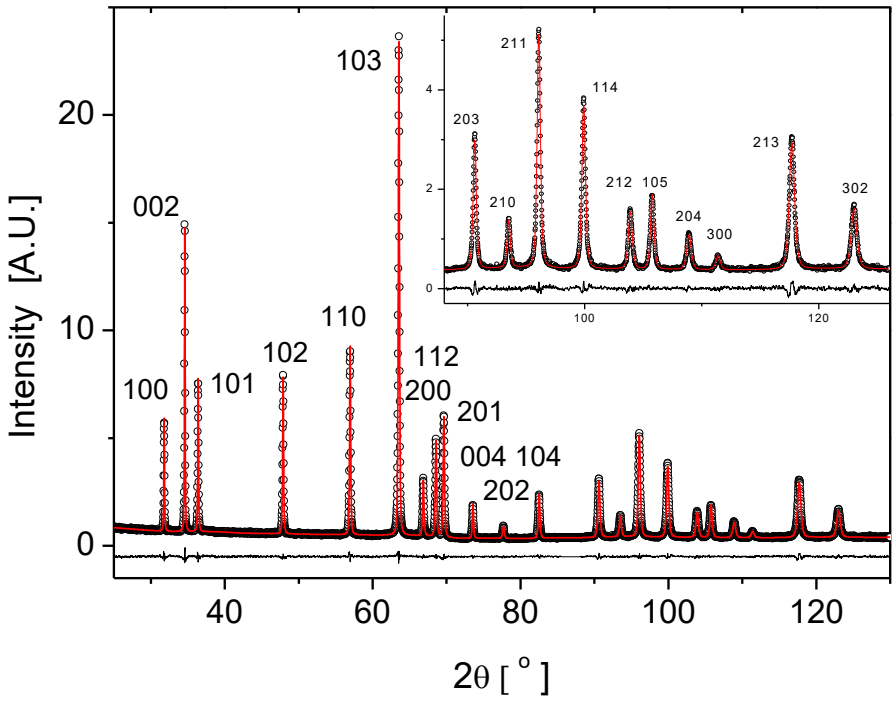

Fig. A.2: The measured (black open circles) and the calculated (red solid lines) diffraction patterns of the irradiated Zr-4 specimen. The difference between the measured and calculated patterns is shown at the bottom of the figure.

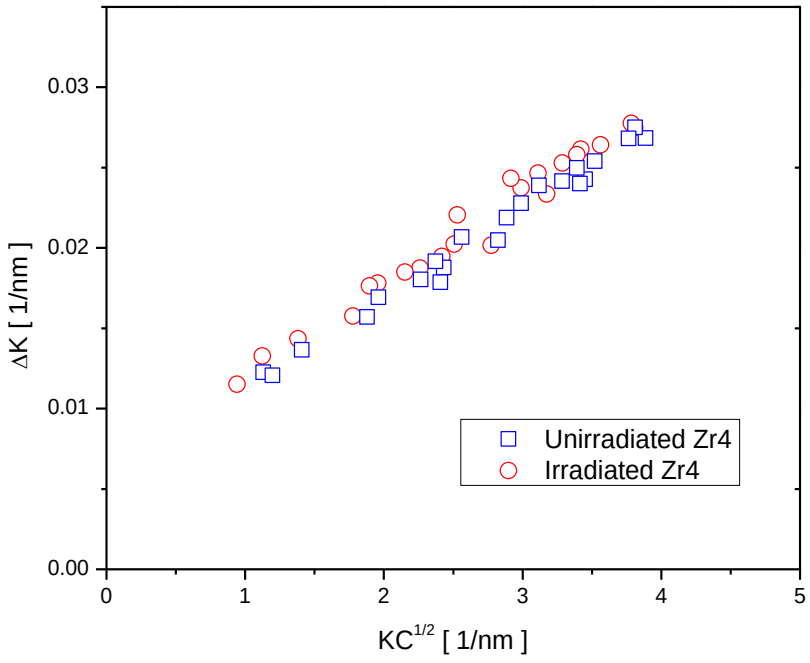

Fig. A.3: The mWH plots of the FWHM for the unirradiated (blue squares) and irradiated (red circles) Zr-4 specimens.

Table A.1: The area average mean crystallite size, d_{area}, the dislocation densities, ρ, the fractions of slip-system types, $h_{<a>}$ and $h_{<c+a>}$ and the dislocation arrangement parameter M for the Zr-4 samples.

Zr-4	d_{area} [nm]	ρ [10^{14} m^{-2}]	$h_{<a>}$	$h_{<c+a>}$	M
Unirradiated	99	2.0	58	42	5
Irradiated	90	2.0	62	38	5

The microhardness of unirradiated and irradiated Zr-4 specimens were measured using a Zwick/Roell-ZHμ-Indentec microhardness tester. The measurements were carried out on the RD-TD and ND-TD surfaces of the samples. The hardness values of the unirradiated specimen are 236 (±6) and 202 (±10) for the RD-TD and ND-TD surfaces, respectively. After irradiation, the corresponding hardness values increase to 251 (±8) and 215 (±7). The results show the hardening effect can be observed at such a low neutron fluence, although dislocation density hardly increases in the irradiated sample. The hardening is probably attributed to irradiation-formed point defects or small-size dislocation loops.

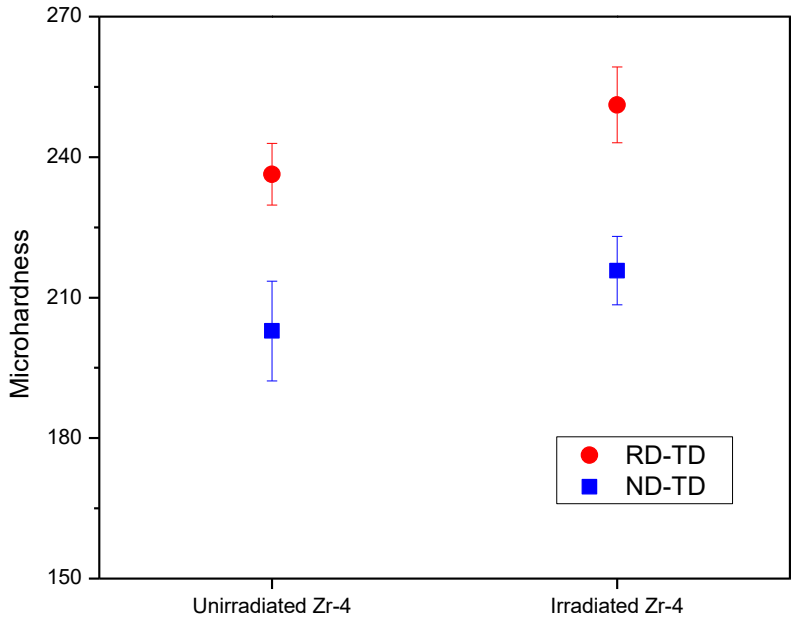

Fig. A.4: Microhardness of the unirradiated and irradiated Zr-4 specimens measured on the RD-TD and ND-TD surfaces.

A.2 Microstructure parameters of HPT deformed V-5Cr-5Ti alloy

Table A.2: Flow stress σ, q and M parameters, dislocation densities ρ, median and logarithmic variance of the size distribution function m and κ, area average mean crystallite size, d_{area} for the samples deformed at 4 GPa.

Sample	σ [MPa]	q	M	ρ [10^{14} m^{-2}]	m [nm]	κ	d_{area} [nm]
4G-0.25rot-0*R*	770	-1.2	13.5	11	50.2	0.31	63
4G-0.5rot-0*R*	855	-1.4	5.3	28	33.8	0.36	46
4G-1rot-0*R*	863	-0.9	5.4	38	19.2	0.54	40
4G-2rot-0*R*	1012	-0.5	5.5	65	13.7	0.60	34
4G-4rot-0*R*	1022	-1.2	5.2	62	10.4	0.65	30
4G-8rot-0*R*	1131	-1.2	5.4	79	13.3	0.61	34
4G-0.25rot-0.5*R*	970	-0.4	7.0	36	34.1	0.39	50
4G-0.5rot-0.5*R*	1027	-0.5	5.7	38	33.1	0.35	45
4G-1rot-0.5*R*	1179	-0.6	7.0	64	11.1	0.63	30
4G-2rot-0.5*R*	1246	-0.8	5.9	86	11.0	0.65	31
4G-4rot-0.5*R*	1231	-0.5	5.8	87	12.4	0.61	31
4G-8rot-0.5*R*	1216	-0.5	6.0	86	13.8	0.58	32
4G-0.25rot-1*R*	1036	-0.5	5.0	58	33.6	0.33	44
4G-0.5rot-1*R*	1160	-0.5	5.0	57	15.3	0.54	31
4G-1rot-1*R*	1231	-0.8	5.1	70	15.2	0.49	28
4G-2rot-1*R*	1196	-0.7	6.2	80	12.7	0.60	31
4G-4rot-1*R*	1186	-1.1	5.5	74	13.2	0.59	31
4G-8rot-1*R*	1215	-0.9	5.5	77	13.0	0.59	31
4G-4rot-0.25*R*	1184	-0.5	5.9	82	12.3	0.61	31
4G-8rot-0.25*R*	1184	-0.5	6.4	87	11.2	0.66	33
4G-4rot-0.75*R*	1222	-0.8	6.3	76	11.3	0.63	31
4G-8rot-0.75*R*	1157	-0.4	6.0	84	13.2	0.58	31

Table A.3: Flow stress σ, q and M parameters, dislocation densities ρ, median and logarithmic variance of the size distribution function m and κ, area average mean crystallite size, d_{area} for the samples deformed at 8 GPa.

Sample	σ [MPa]	q	M	ρ [10^{14} m^{-2}]	m [nm]	κ	d_{area} [nm]
8G-0.25rot-0*R*	768	-1.1	10.5	15	61.7	0.19	67
8G-0.5rot-0*R*	835	-1.2	5.4	23	35.0	0.40	52
8G-1rot-0*R*	987	-0.9	5.5	49	24.0	0.48	43
8G-2rot-0*R*	1011	-0.4	5.5	63	13.7	0.60	34
8G-4rot-0*R*	1119	-0.3	5.8	74	13.3	0.59	31
8G-8rot-0*R*	1123	-0.2	5.7	79	12.7	0.61	32
8G-0.25rot-0.5*R*	927	-0.4	7.0	36	34.1	0.39	50
8G-0.5rot-0.5*R*	1096	-0.6	5.0	56	24.1	0.44	39
8G-1rot-0.5*R*	1136	-0.8	5.8	70	11.5	0.64	32
8G-2rot-0.5*R*	1249	-1.0	5.1	91	14.8	0.57	33
8G-4rot-0.5*R*	1258	-0.5	6.1	87	13.0	0.61	33
8G-8rot-0.5*R*	1243	-0.1	6.8	85	12.9	0.57	29
8G-0.25rot-1*R*	1050	-0.5	5.8	57	23.5	0.41	36
8G-0.5rot-1*R*	1132	-0.8	5.3	65	15.1	0.54	32
8G-1rot-1*R*	1198	-0.6	5.0	78	16.7	0.49	31
8G-2rot-1*R*	1252	-0.5	6.0	76	12.6	0.57	28
8G-4rot-1*R*	1216	-0.9	6.0	71	11.0	0.63	30
8G-8rot-1*R*	1257	-0.4	6.5	75	11.6	0.60	28
8G-4rot-0.25*R*	1208	-0.4	6.5	84	11.9	0.65	34
8G-8rot-0.25*R*	1253	-0.9	6.2	83	12.1	0.64	34
8G-4rot-0.75*R*	1204	-0.7	5.8	82	11.8	0.64	33
8G-8rot-0.75*R*	1236	-0.2	7.2	76	12.6	0.59	30

Acknowledgements

I would like to express my deepest appreciation to my supervisors, Prof. Tamás Ungár and Dr. Gábor Ribárik for their instructions, encouragement and steady support. What I learned from them is not only the knowledge of X-ray diffraction and materials physics, but also the spirit of their persistent efforts in the field of line profile analysis. I'm especially grateful to Prof. Tamás Ungár for his careful and patient revision of this manuscript.

I would like to thank Mr. Bertalan Jóni for his guidance in the operation of high-resolution X-ray diffractometer and other instruments, and the processing techniques of X-ray diffraction data. I also thank Mr. Bertalan Jóni and Mr. Gyula Zilahi for a lot of help during the period of my staying at Budapest.

I would like to acknowledge Profs István Groma, János Lendvai, Géza Tichy, Károly Havancsák, Jenő Gubicza and other colleagues for their providing excellent education at Department of Materials Physics, ELTE.

I'm grateful to my colleagues at Institute of Nuclear Physics and Chemistry, CAEP, especially to Profs Shuming Peng, Tongzai Yang and Bo Chen for their support of my studying at ELTE.

Thanks for everyone of the co-authors of our common papers. Without your contributions, it would be impossible for me to go through the difficulties and eventually finish the work.

Finally, I thank my wife, Lihua Feng, and my son, Zeyu Fan, for their independence when I was writing this dissertation.

Short summary

Both nuclear fission and fusion power become increasingly important for the current and future world energy. The service conditions in nuclear reactor are extremely rigorous. In order to maintain normal operation of reactor, structural materials should possess excellent comprehensive performance. In this dissertation, two typical structural materials, Zr and V-5Cr-5Ti, are studied. The high-resolution X-ray diffraction and the CMWP procedure are applied to obtain the microstructural information of deformed Zr and V-5Cr-5Ti. And the correlation between the microstructure and mechanical properties of the structural materials are investigated. The main scientific results of the work are presented as follows.

The cold-rolled zirconium specimens were tensile-deformed along the rolling and the transverse directions. It is observed that the hardening rate and plasticity are larger in the RD than in the TD samples. At the same time, the texture of the RD samples remained unchanged, while in the TD samples the prismatic poles were gradually aligning along the loading direction during tensile deformation. For determining microstructure parameters of textured specimens, an algorithm was developed to identify and sort out the diffraction peaks in diffraction patterns corresponding to the same texture components. The dislocation densities prevailing in the RD samples increased monotonously with strain, and the fractions of slip-systems in the major and random texture components developed in a complementary manner. The well-balanced activity between the major and random texture components results in the good plasticity of the RD samples. During the texture evolution of the TD samples, the <a>-type slip-system dominates the deformation in nearly plane strain. Once the new type of texture appeared significantly, the samples show necking and more <c+a>-type dislocations accumulate in the major texture component, apparently to accommodate the deformation.

The specimens of V-5Cr-5Ti alloy were processed by HPT at 4 and 8 GPa with 0.25, 0.5, 1, 2, 4 and 8 rotations. X-ray diffraction patterns and microhardness were measured at different positions along the radius of the HPT disks. It was found the strength, dislocation densities and subgrain size are almost the same in the samples deformed at 4 and 8 GPa. Work hardening proceeds up to about $\gamma \cong 50$ where it saturates at a level of about $\sigma \cong 1220$ (±40) MPa. The dislocation density was obtained to increase up to about $\gamma \cong 75$ where it saturated at a level of about $\rho \cong 82\ (\pm 8) \times 10^{14}\ m^{-2}$. The majority of dislocations are of edge character, which indicates solute atoms such as Cr and Ti play an important role in pinning of edge dislocations. The subgrain size decreases to about $d_x \cong 31$ (±2) nm at about $\gamma \cong 15$ and saturates at higher values. The heating experiments have revealed that the dislocation density remains constant up to about 800 °C. However, the change of peak tails at 800 ºC shows the dipole character becomes stronger indicating the onset of recovery process. The study has shown that large plastic deformation of the V-5Cr-5Ti alloy produces a strongly strained and fairly stable microstructure.

EÖTVÖS LORÁND UNIVERSITY
DECLARATION FORM
for disclosure of a doctoral dissertation

I. The data of the doctoral dissertation:

Name of the author: Zhijian Fan
MTMT-identifier: 10068259
Title and subtitle of the doctoral dissertation: Microstructure of nuclear structural materials, Zr and V-5Cr-5Ti, determined by X-ray line profile analysis
DOI-identifier: 10.15476/ELTE.2019.129
Name of the doctoral school: Doctoral School of Physics
Name of the doctoral programme: Materials science and solid state physics
Name and scientific degree of the supervisor: Tamás Ungár, DSc; Gábor Ribárik,Dr.
Workplace of the supervisor: ELTE, Department of Materials Physics

II. Declarations

1. As the author of the doctoral dissertation, I agree to public disclosure of my doctoral dissertation after obtaining a doctoral degree in the storage of ELTE Digital Institutional Repository. I authorize the administrator of the Department of Doctoral, Habilitational and International Affairs of the Dean's Office of the faculty of Science to upload the dissertation and the abstract to ELTE Digital Institutional Repository, and I authorize the administrator to fill all the declarations that are required in this procedure.

2. As the author of the doctoral dissertation, I declare that
a) the doctoral dissertation and abstract uploaded to the ELTE Digital Institutional Repository are entirely the result of my own intellectual work and as far as I know, I did not infringe anyone's intellectual property rights.;
b) the printed version of the doctoral dissertation and the abstract are identical with the doctoral dissertation files (texts and diagrams) submitted on electronic device.

3. As the author of the doctoral dissertation, I agree to the inspection of the dissertation and the abstract by uploading them to a plagiarism checker software.

Budapest, Jun. 9, 2019

Zhijian Fan

Signature of dissertation author